

GRAIN BOUNDARY MOBILITY TENSOR AND TOPOLOGICAL PHASE
TRANSITIONS

Kongtao Chen

A DISSERTATION

in

Materials Science and Engineering

Presented to the Faculties of the University of Pennsylvania

in

Partial Fulfillment of the Requirements for the

Degree of Doctor of Philosophy

2020

Supervisor of Dissertation

David J. Srolovitz, Joseph Bordogna Professor of Engineering and Applied Science

Graduate Group Chairperson

I-Wei Chen, Skirkanich Professor of Materials Innovation

Dissertation Committee

Andrea J. Liu, Hepburn Professor of Physics

Prashant K. Purohit, Professor of Mechanical Engineering and Applied Mechanics

Vivek Shenoy, Eduardo D. Glandt President's Distinguished Professor

GRAIN BOUNDARY MOBILITY TENSOR AND TOPOLOGICAL PHASE
TRANSITIONS

© COPYRIGHT

2020

Kongtao Chen

This work is licensed under the
Creative Commons Attribution
NonCommercial-ShareAlike 3.0
License

To view a copy of this license, visit

<http://creativecommons.org/licenses/by-nc-sa/3.0/>

ACKNOWLEDGMENT

I owe my greatest appreciation to my advisor, Dr. Srolovitz, for leading me to computational materials science and grain boundary kinetics and training me to be an independent researcher. I want to thank my dissertation committee members, Drs. Purohit, Liu, and Shenoy, for insightful comments and suggestions on this dissertation. I extend my sincere gratitude to all the members of David Srolovitz's group, especially Jian Han and Spencer L. Thomas, with whom I have collaborated on research. I am thankful for all the faculty and staff at the University of Pennsylvania who contributed greatly to my experience over the course of earning my Ph.D. I have had the pleasure of collaborating with many researchers to whom I am very thankful, including Dr. Purohit at the University of Pennsylvania and Dr. Pan at the University of California, Irvine. I would also like to acknowledge Dr. Khanttha at the University of Pennsylvania for her insightful discussions. Finally, I am forever indebted to my family for their love.

ABSTRACT

GRAIN BOUNDARY MOBILITY TENSOR AND TOPOLOGICAL PHASE TRANSITIONS

Kongtao Chen

David J. Srolovitz

The grain boundary (GB) mobility relates the GB velocity to the driving force. While the GB velocity is normally associated with motion of the GB normal to the GB plane, there is often a tangential motion of one grain with respect to the other across a GB; i.e., the GB velocity is a vector. Grain boundary motion can be driven by a chemical potential that jumps across a GB or by shear applied parallel to the GB plane; the driving force has three components. Hence, the GB mobility must be a tensor (the off-diagonal components indicate shear coupling). Recent molecular dynamics (MD) and experimental studies show that the GB mobility may abruptly jump, smoothly increase, decrease, remain constant or show multiple peaks with increasing temperature. Performing MD simulations on symmetric tilt GBs in copper, we demonstrate that all six components of the GB mobility tensor are non-zero (the mobility tensor is symmetric, as required by Onsager). We demonstrate that some of these mobility components increase with temperature while, surprisingly, others decrease. We develop a disconnection dynamics-based statistical model that suggests that GB mobilities follow an Arrhenius relation with respect to temperature T below a critical temperature T_c and decrease as $1/T$ above it. T_c is related to the operative disconnection modes and their energetics. We implement this model in a kinetic Monte Carlo (kMC); the results capture all of these observed temperature dependencies and are shown to be in quantitative agreement with each other and direct MD simulations of GB migration for a set of specific GBs. We demonstrate that the abrupt change in GB mobility results from a Kosterlitz-Thouless (KT) topological phase transition. This phase transition corresponds to the screening of the long-range interactions between (and unbinding of) disconnections.

This phase transition also leads to abrupt change in GB sliding and roughening. We analyze this KT transition through mean-field theory, renormalization group methods, and kMC simulation. Finally, we examine the impact of the generalization of the mobility and KT transition for grain growth and superplasticity.

TABLE OF CONTENTS

ACKNOWLEDGMENT	iii
ABSTRACT	iv
LIST OF TABLES	viii
LIST OF ILLUSTRATIONS	x
CHAPTER 1 : Introduction	1
1.1 Grain Boundary Kinetics	1
1.2 Thesis Overview	6
CHAPTER 2 : Grain Boundary Shear Coupling	9
2.1 Simulation Method	10
2.2 Mechanically-Driven Shear Coupling	12
2.3 Chemical Potential Jump-Driven Shear Coupling	15
2.4 Statistical Disconnection Model	17
2.5 Conclusions	25
CHAPTER 3 : Grain Boundary Mobility Tensor	27
3.1 Generalized GB Kinetics	28
3.2 Simulation Methods	30
3.3 Simulation Results	31
3.4 Statistical Disconnection Model	32
3.5 Discussion	37
3.6 Conclusion	38
CHAPTER 4 : Temperature Dependence of Grain Boundary Mobility	40

4.1	Kinetic Monte Carlo Simulations	42
4.2	Statistical Disconnection Model	49
4.3	Parameters for Specific Grain Boundaries and Comparison with MD	56
4.4	Discussion and Conclusions	60
CHAPTER 5 : Grain Boundary Topological Phase Transitions		68
5.1	Disconnection Topological Transitions	70
5.2	Kinetic Monte Carlo Simulations	78
5.3	Grain Growth Stagnation	83
5.4	Discussion	85
CHAPTER 6 : Final Remarks		88
APPENDIX		90
A.1	The Parameters C^x and β_0^x	90
A.2	Limiting Behavior for Shear Coupling Factor	91
A.3	Enumeration of Modes	91
A.4	Coupling Factor in the Framework of Mobility Tensor	93
A.5	Grain Growth in 3- and d -dimensions	93
A.6	The Elastic Energy and Stress in the Kinetic Monte Carlo Simulations	95
A.7	Configurational Entropy and Equilibrium Disconnection Concentration	98
A.8	Consistency between Lattice Model and Continuum Theory	100
A.9	Grain Boundary Roughness	102
BIBLIOGRAPHY		104

LIST OF TABLES

TABLE 1 : Fitting parameters A and B in Eq. (2.3) for the data in Figs. 2 and 5. γ is the GB energy for this potential at 0 K (Mishin et al., 2001). b_i , h_i , and β_i are the Burgers vector, step height, and coupling factor of disconnection mode with the i^{th} lowest barrier (see Eq. (2.3) and the analytical expressions for the parameters). B and γ are in J/m^2 and A is in GPa. b_1 , b_2 , h_1 , and h_2 are in cubic lattice constant units ($a_0 = 0.36 \text{ nm}$). F identifies the driving force type. 21

TABLE 2 : Activation energy $Q^{(m)}$ and pre-exponential $c_{ij}^{(m)} \equiv f_0 L^2 H_i^{(m)} H_j^{(m)} / k_B$ for the m^{th} mode for the mobility component M_{ij} , obtained by fitting Eq. (3.5) to the data in Fig. 9. The fit was performed assuming a single-mode expression for M_{i3} ($i = 1, 2, 3$) and a two-mode expression for M_{ij} ($i, j = 1, 2$). The pre-exponential normalization is $c_0 = 1 \text{ K m s}^{-1} \text{ MPa}^{-1}$. The symbols “-” in the last two rows indicate that a single-mode model was sufficient (no two-mode fitting was performed). 35

TABLE 3 : Parameters for two symmetric tilt GBs in EAM (Mishin et al., 1999) Al. $a_0 = 0.405$ nm is the lattice constant, a_{dsc} is the size of a DSC lattice cell, m is the index of disconnection mode, b_m , h_m and E_m^* are the corresponding Burgers vector, step height, and glide barrier, A_m and B_m are fitting parameters (see Eq. (4.19)), $K \equiv \mu/[4\pi(1 - \nu)]$ (μ and ν are the shear modulus and Poisson’s ratio), γ is the step energy, δ_0 is the effective core size (r_0 is the core size), δ is the spacing between lattice point in the quasi-1D lattice model, and ζ scales the contribution of the core energy (Eq. (4.7)). The range of $K = \mu/[4\pi(1 - \nu)]$ corresponds to different crystal orientations and the anisotropic elastic constants are from Mishin et al. (1999). The $\Sigma 17$ [100] step energy is estimated from $\sqrt{2}\gamma_s - \gamma_0$ (Han et al., 2018), where $\gamma_s = 0.4861$ J/m² for the (014) and $\gamma_0 = 0.4657$ J/m² for the (035) STGB in EAM Al. The $\Sigma 25$ [100] step energy estimates employ $\gamma_s = 0.4707$ J/m² for the (017) and $\gamma_0 = 0.3872$ J/m² for the (034) STGB. γ_0 and γ_s are from Han et al. (2017). 57

TABLE 4 : Transition temperatures for thermodynamic GB roughening and sliding and where abrupt changes in GB mobilities are expected for pure step ($\mathbf{b} = \mathbf{0}$), pure dislocation ($h = 0$), a single disconnection mode (\mathbf{b}, h), and multiple disconnection modes (\mathbf{b}_m, h_m). A “-” and “0” indicate no transition and a transition temperature at 0 K. The subscripts and superscripts indicate dimensionality (2d/3d) and pure step (S), pure dislocation (D), single disconnection (1), and multiple disconnection (M) modes. M_{11} , M_{12} and M_{22} represent mobilities associated with pure GB migration, shear coupling, and sliding, respectively (Chen et al., 2020a). For multiple disconnection modes, entries only represent the lowest temperature of abrupt mobility changes. 85

LIST OF ILLUSTRATIONS

<p>FIGURE 1 : The periodic simulation cell containing two equivalent symmetric tilt GBs shown in red (periodicity only shown in the x- and z-directions). The tilt axis is parallel to z and the GB plane is nominally x-z.</p>	11
<p>FIGURE 2 : Temperature dependence of the inverse shear coupling factor β^{-1} for shear stress-driven migration of three [001] symmetric tilt grain boundaries, $\Sigma 5(310)$, $\Sigma 13(510)$, and $\Sigma 37(750)$. The circles indicate the mean value of β^{-1} for two GBs (the individual values of β^{-1} are the top and bottom of the error bars which are not visible when their difference is smaller than the size of the circle). The continuous curves are from the fits to Eq. (2.2) and (2.3) for each GB.</p>	13
<p>FIGURE 3 : The temperature dependence of the inverse coupling factor β^{-1} is different under constant stress and strain rate. Constant stress MD data and diamond symbol constant strain rate data are averaged over 2 GBs. The open circles correspond to the constant strain rate (fixed end boundary condition) MD data from (Cahn et al., 2006). The open diamond symbols show constant strain rate simulation results under periodic boundary conditions. The horizontal black dashed lines indicate the values of β^{-1} for $T \rightarrow 0$.</p>	14
<p>FIGURE 4 : Coupling factor versus shear stress for the $\Sigma 7[111](12\bar{3})$ symmetric tilt GB. The data points are represent the mean for 2 GBs. The continuous curve is the best fit parabola to these data, as suggested by Eq. (2.4).</p>	14

FIGURE 5 :	Temperature dependence of the coupling factor β for three GBs driven by a constant chemical potential jump under zero net shear stress conditions. The continuous curves are fits of the data to Eqs. (2.2) and (2.3) for each GB.	16
FIGURE 6 :	Coupling factor versus chemical potential jump for the $\Sigma 7[111](12\bar{3})$ symmetric tilt GB. The data points represent the mean for 2 GBs. The continuous curve is the best fit parabola to these data, as suggested per Eq. (2.5).	17
FIGURE 7 :	Temperature dependence of the coupling factor β for constant stress and chemical potential jump driving forces. The data are plotted on a logarithmic scale to fit the data meaningfully on one plot. The continuous curves are fits to the constant stress and chemical potential jump data as per Eqs. (2.2) and (2.3) for each GB. Curves are from fitting A and B from Eqs. (2.2) and (2.3) for each GB.	18
FIGURE 8 :	Bicrystal simulation cell with a symmetric tilt GB (shaded yellow). The tilt axis is parallel to x_3 and the GB plane is nominally x_2 - x_3 . The cell is periodic in the x_2 - and x_3 -directions and a thin, rigid perfect crystal layer is added to the top and bottom surfaces which may displace freely.	29
FIGURE 9 :	Temperature dependences of the GB mobility components (a) M_{11} , (b) M_{22} , (c) M_{33} , (d) M_{12} , (e) M_{13} , and (f) M_{23} (error bars indicate the range of the simulation results). The data points represent the MD results and the dashed lines are fits of these data to Eq. (3.5) for a single disconnection mode. For the off-diagonal components of M_{ij} ($i \neq j$), two sets of data points (blue circles and red squares) are shown corresponding to M_{ij} and M_{ji} ; the Onsager relation suggests that these two sets of data are equivalent.	31

FIGURE 10 : Numerical results for (a) square of the mean grain size R^2 vs. time t and (b) the shear stress τ vs. time t at 1000 K (blue), 1100 K (green) and 1200 K (red). The solid and dotted lines are for the case of $n = 12$ and 4, respectively (n is the number of edges of a grain in a 2D microstructure). The insets show the time evolutions for much longer times.	36
FIGURE 11 : (a) Quasi-1D lattice model description of a tilt GB. The state of lattice site i is (u_i, z_i) . (b) The GB state after nucleation of a pair of disconnections of mode m (i.e., (b_m, h_m) and $(-b_m, -h_m)$) at site i	43
FIGURE 12 : Schematic of the energy barrier associated with a single transition associated with the formation of a pair of disconnections of mode m at site i	47

FIGURE 13 : kMC simulation results for the (reduced) temperature dependence of the (reduced) GB mobility. The label above each figure indicates the operative disconnection modes: $(\tilde{b}_1, \tilde{h}_1)$ and, if there is another mode, $(\tilde{b}_2, \tilde{h}_2)$ (recall that $\tilde{h} = h/\delta$ and $\tilde{b} = b/\delta$). The kMC simulation correspond to: (a) a single pure-step disconnection mode – $(\tilde{b}_1, \tilde{h}_1) = (0, 1)$; (b) a single mode – $(\tilde{b}_1, \tilde{h}_1) = (1, 1)$; (c) two modes – $(\tilde{b}_1, \tilde{h}_1) = (0, 1)$ and $(\tilde{b}_2, \tilde{h}_2) = (1, 1)$; (d) two modes – $(\tilde{b}_1, \tilde{h}_1) = (0, 1)$ and $(\tilde{b}_2, \tilde{h}_2) = (2, 2)$; and (e) two modes – $(\tilde{b}_1, \tilde{h}_1) = (0, 1)$ and $(\tilde{b}_2, \tilde{h}_2) = (3, 3)$. In each figure, the kMC results are represented by solid black squares; the solid black lines connecting the kMC data points are drawn as guides to the eye. The blue dashed lines are obtained from the analytical model, i.e., Eq. (4.16). (c) also shows a comparison between the two-mode model (solid black squares) and the sum of the reduced mobilities for the two 1-mode simulations corresponding to the same two modes, individually, as shown in (a) and (b) (hollow red circles). This comparison demonstrates that the mobility in the 2-mode case can be approximated as the sum of those for the two 1-mode cases. The green dotted line in (a) indicates the relationships $\ln \tilde{M} = -1/\tilde{T}$ and the red dotted line indicates $\tilde{M} = 1/\tilde{T}$ 63

FIGURE 14 : Schematics of the energy vs. separation of a disconnection pair for the cases of (a) $\psi = 0$ and (b) $\psi \neq 0$. The red curves represent $E^S(R) = E^c + W^I(R) + W^E(R)$, the blue curves represent $E(R) = E^S(R) + E^G(R)$, and the green solid line represents $W^E(R) = -\psi hR$. R^\ddagger is the “critical” separation corresponding to the total energy barrier. In (b), the order of the approximation to each part of the energy associated with the external driving force is of order $\mathcal{O}(\psi^2)$ 64

FIGURE 15 : Temperature dependence of GB mobility described by Eq. (4.18) for a single mode (black dotted curve), two modes with $h_2/h_1 = 2 < e$ (blue dashed curve), and two modes with $h_2/h_1 = 3 > e$ (red solid curve) cases. In the two-mode simulations $Q_2 = 10Q_1$ 65

FIGURE 16 : (a1) and (b1) are the energy E^S vs. separation R of a pair of disconnections, scaled by the supercell period L for the $\Sigma 17$ [100] (035) and $\Sigma 25$ [100] (034) STGBs in EAM Al, respectively. The data point colors indicate disconnection modes ($b_m/a_{\text{dsc}}, h_m/a_{\text{dsc}}$), as indicated in the legend. (a2) and (b2) are the energy landscape between two neighboring metastable configurations with the highest energy (at the maxima of each curve in (a1) and (b1)) obtained from the NEB calculations. E^* is the energy difference between the maximum and zero. 66

FIGURE 17 : Temperature dependence of GB mobility obtained by MD simulations (blue hollow squares), kMC simulations (black solid circles) and disconnection theory (red dashed lines) for (a) $\Sigma 17$ [100] (035) and (b) $\Sigma 25$ [100] (034) STGBs in EAM Al. The error bars in the MD data represent the mobilities obtained in two MD simulations and the hollow, blue squares represent their mean. 67

FIGURE 18 : (a) Disconnection dipoles on a 1d GB in 2d. δ , r , L and S denote the disconnection core size, the separation of the disconnections in a disconnection dipole, the average distance between the disconnection dipoles and the system size in the x -direction, respectively. (b) The states of the system at i before and after disconnection dipole nucleation are (u_i, y_i) and $(u_i + b_m, y_i + h_m)$, respectively, for a pair of disconnections of mode m at location i 73

FIGURE 19 : Renormalization flows obtained by numerical solution of Eq. (5.5) with $\psi = \tau = 0$ and different initial conditions $(g(0), f(0))$. The arrows denote directions of increasing length scale l (coarse-graining). The red curve is the critical manifold. The flows in the shaded region converge to $(g > 1.5, f = 0)$ as $l \rightarrow \infty$, while the flows in the unshaded region converge to $(g = 0, f \rightarrow \infty)$. The blue curve corresponds to $(g(0, T), f(0, T))$ where the temperature T increases from bottom right to top left; the material and GB parameters are those used for the one-mode kMC simulation. The Kosterlitz-Thouless transition temperature corresponds to the point where the red and blue curves cross. 76

FIGURE 20 : (a)-(b) show the GB roughness σ_y vs. T for the (a) pure step and (b) single mode with $b \neq 0$; the insets in (b) is the standard deviations of shear σ_u vs. temperature T . (c)-(d) show the average of the (square of the) magnitude of the Fourier transform (k is a wave vector) of the equilibrium GB profile $y(x)$, $\langle |y(k)|^2 \rangle$, for several temperatures (see the legend) for the (c) pure step and (d) single mode with $b \neq 0$. (e) shows the correlation length $\xi(T)$ (obtained from fitting $\xi = AT/(k^d + \xi^{-d})$) for each temperature to the kMC data in (c)-(d); the horizontal dashed line (at $\xi = 150$) is the kMC simulation cell period (in x). (f)-(g) show $\ln(MT)$ vs. $1/T$ (Chen et al., 2020a), where M is the GB mobility for the (f) pure step and (g) single mode cases. The vertical gray lines label $T = 0.1$ in (b), and (g), and $T = 0.14$ in (e). 80

FIGURE 21 : Temperature dependence of stagnated grain size D_s from mesoscale MC simulations (data points) from Holm and Foiles (2010) and a linear fit from Eq. (5.13). D_0 and T_m are the initial grain size and melting point, respectively. 84

FIGURE 22 : The temperature (T) dependence of the coupling factor (β) for the $\Sigma 7$ $[111]$ $(12\bar{3})$ GB in copper obtained from the MD simulation data reported in Fig. 9 of the main text.	94
FIGURE 23 : Lattice-model description of the formation of a disconnection pair (dipole), $(b, -h)$ and $(-b, h)$, on site i	102

CHAPTER 1 : Introduction

1.1. Grain Boundary Kinetics

Our current understanding of microstructural evolution in polycrystalline materials is based primarily on our understanding of how grain boundaries (GBs) move. Grain boundary motion is central to a wide range of microstructure evolution processes, including normal grain growth, abnormal grain growth, grain growth stagnation, primary recrystallization, superplasticity, and sintering. These processes may be driven by different factors, e.g., stress, injection of defects from within the grains, capillarity (surface tension), and differences in defect densities or elastic energy (across the GB).

The most important dynamical property for the evolution of polycrystalline microstructures (e.g., grain growth, recrystallization) is the GB mobility. Normally, we describe GB dynamics as overdamped, where the GB mobility is defined (Turnbull, 1951) as the ratio of the GB velocity v to the thermodynamic driving force (per area) F in the limit of infinitesimal driving force, $M = \lim_{F \rightarrow 0} v/F$. Grain boundary mobility has been measured in many different metals (e.g., Zn (Li et al., 1953), Pb (Rutter and Aust, 1965), Al (Hu and Rath, 1972), Au (Grünwald and Haessner, 1970; Molodov et al., 1995), Cu (Viswanathan and Bauer, 1973), Fe-Si (Lejček et al., 1994; Furtkamp et al., 1998), Bi (Molodov et al., 1998)) and ceramics (e.g., alumina (Powers and Glaeser, 1998)) and as a function of several variables (e.g., temperature, bicrystallography, solute concentration) in bicrystal experiments with different types of driving forces (e.g., stress (Li et al., 1953), curvature (Hu and Rath, 1972; Grünwald and Haessner, 1970; Molodov et al., 1995; Viswanathan and Bauer, 1973; Lejček et al., 1994; Furtkamp et al., 1998), magnetic field (Molodov et al., 1998)), as summarized in (Gottstein and Shvindlerman, 2009). More recently, molecular dynamics (MD) simulations have been employed to study GB mobilities in bicrystals as a function of many of the same variables (Upmanyu et al., 1999; Zhang et al., 2004, 2005; Janssens et al., 2006; Olmsted et al., 2009; Zhou and Mohles, 2011; Song and Hoyt, 2012; Homer et al., 2014; Rahman et al., 2014; Priedeman et al., 2017) and driving forces (Upmanyu et al., 1999; Zhang et al.,

2005) (as well as driving forces only accessible in simulations (Janssens et al., 2006)). Olmsted and colleagues (Olmsted et al., 2009; Homer et al., 2014) systematically studied the mobility of 388 GBs (different macroscopic, bicrystallographic degrees of freedom) in Ni as a function of temperature.

Grain boundary migration may also be driven by the application of a shear across the GB plane. Shear coupling refers to the motion of GBs driven by shear across the GB plane or, equivalently, the displacement of one grain relative to the other during GB migration. While shear coupling was first observed more than 60 years ago (Li et al., 1953; Bainbridge et al., 1954; Biscondi and Goux, 1968), interest in this topic has grown considerably in the past decade. Shear coupling has been reported in both metals (e.g., Al (Biscondi and Goux, 1968; Fukutomi et al., 1991; Wanning et al., 2001, 2002; Wanning and Rollett, 2005), Zn (Li et al., 1953; Bainbridge et al., 1954)) and ceramics (e.g., cubic zirconia (Yoshida et al., 2004)). Grain boundary sliding is, in some sense, the absence of shear coupling (shear across the GB produces no migration). Grain boundary sliding has been observed in a wide range of polycrystalline systems (e.g., see Sheikh-Ali et al. (2003)). These experimental observations of shear coupling and GB sliding have been reproduced in a wide-range of atomic-scale simulations (e.g., see Molteni et al. (1996, 1997); Hamilton and Foiles (2002); Chen and Kalonji (1992); Shiga and Shinoda (2004); Chandra and Dang (1999); Haslam et al. (2003); Sansoz and Molinari (2005); Cahn et al. (2006); Thomas et al. (2017); Chen et al. (2019)). The importance of shear coupling in microstructure evolution is illustrated in experimental observations of stress-assisted grain growth in nanocrystalline metals (Gianola et al., 2006; Rupert et al., 2009).

Recent studies (Cahn et al., 2006; Thomas et al., 2017; Han et al., 2018; Chen et al., 2019) suggest that, because of shear coupling, GB mobility depends on the origin of the driving force for GB migration (stress versus jumps in chemical potential across a GB). This dependence contradicts the widely accepted notion that GB mobility is an intrinsic GB property (independent of the source of the driving force). However, if GB mobility depends

on the nature of the driving force, the notion of GB mobility should be expanded. The shear-coupling factor (ratio of GB sliding and migration rates) also depends on the nature of the driving force (Chen et al., 2019). Hence, GB motion is associated with three orthogonal displacements (and velocities): GB migration (perpendicular to the GB plane) and translations of one grain with respect to the other (in two directions tangent to the GB plane). Accordingly, there are three generalized forces (per unit area) associated with these motions (variations of the free energy with respect to three displacements). Assuming that the displacements associated with the GB motion are overdamped (an excellent approximation since GB velocities are small compared with all speeds of sound), the proportionality constant between the velocity and force vectors should therefore be a 3×3 mobility tensor, \mathbf{M} . If we establish a coordinate system such that the GB normal is parallel to the \mathbf{e}_1 -axis, then M_{11} is the traditional GB (migration) mobility, M_{1j} ($j \neq 1$) components describe shear coupling, and M_{ij} ($i, j \neq 1$) describe GB sliding. Since M_{ij}/M_{11} is often not small, ignoring these non-traditional mobility tensor components (i.e., replacing \mathbf{M} with the scalar $M_{\text{GB}} = M_{11}$) can be inappropriate. Also note that the individual components of \mathbf{M} may have different temperature dependences.

Since the most widely employed approach for controlling the rate (and often the nature) of microstructure evolution is through variation of temperature T (i.e., annealing), the temperature dependence of GB mobility is important for many applications. The temperature dependence of GB mobility has been measured for a wide range of materials both experimentally (Aust and Rutter, 1959a,b; Rutter and Aust, 1965; Gottstein and Shvindlerman, 2009) and via atomistic simulations (Homer et al., 2014; Rahman et al., 2014; Janssens et al., 2006; Zhang et al., 2004; Priedeman et al., 2017; Zhang et al., 2005; Olmsted et al., 2009; Zhou and Mohles, 2011; Song and Hoyt, 2012; Upmanyu et al., 1999; Schönfelder et al., 2005). The quoted references focused on the measurement of the mobility of nominally flat GBs in bicrystals of elemental metals rather than GBs in microstructures (i.e., averaging over many GBs or influenced by GB junctions). The temperature dependence of GB mobility is commonly fit to an Arrhenius relation $M_{11} = M_0 e^{-Q/k_{\text{B}}T}$, where Q is an

activation energy, the prefactor M_0 is a constant, and k_B is the Boltzmann constant. This Arrhenius relation provides a good fit to many of the M vs. T experimental data. However, GB mobilities extracted from atomistic simulations in pure systems show a wide variety of T -dependences (Homer et al., 2014; Olmsted et al., 2009; Schönfelder et al., 2005). Homer et al. (Homer et al., 2014) performed a series of MD simulations of GB migration in Ni for a large number of bicrystallographically different GBs. While nearly half of these GBs showed mobilities that they characterized as Arrhenius over some range of temperature, they also observed several cases for which the GB mobility (i) decreased with increasing T (so called anti-thermal behavior), (ii) was nearly T independent, (iii) exhibited maxima and/or minima with respect to T , and (iv) was nearly zero at low T and then increased rapidly over a small T -range. The existence of such diversity in GB mobility $M(T)$ within a single material challenges our current understanding of and ability to predict GB mobility.

Grain boundary migration occurs through the motion of line defects (i.e., disconnections), that are constrained to lie within the GB and are characterized by both a Burgers vector \mathbf{b} and a step height h that are determined by the underlying GB bicrystallography (Hirth and Balluffi, 1973; Pond and Bollmann, 1979; King and Smith, 1980; Balluffi et al., 1982; Hirth et al., 2006, 2007; Cahn et al., 2006; Thomas et al., 2017; Han et al., 2018; Hadian et al., 2018; Chen et al., 2019, 2020a,b,c). Therefore, GB migration (resulting from step motion along the GB) and lateral grain translation (motion of one grain relative to the other across the GB, resulting from dislocation migration along the GB) are coupled (e.g., see Cahn et al. (2006); Han et al. (2018); Chen et al. (2019)). Both atomistic simulation (Rajabzadeh et al., 2013b; Khater et al., 2012; Combe et al., 2016; Hadian et al., 2018) and electron microscopy (Legros et al., 2008; Momprou et al., 2009; Rajabzadeh et al., 2013a) studies have directly observed GB migration through the formation and migration of disconnections along GBs. The motion of disconnections of different modes, characterized by different (\mathbf{b}_m, h_m) (m is the index for mode) allowed by the bicrystallography, can conspire to affect GB motion. This suggests a possible source for some of the complexity in the observed GB kinetics (e.g., temperature and driving force dependence of GB mobility and coupling

factor) (Thomas et al., 2017; Han et al., 2018; Chen et al., 2019).

Disconnections may be introduced into GBs via homogeneous or heterogeneous nucleation and/or by the decomposition of lattice dislocations. In this discussion, we focus on homogeneous nucleation since, as in phase transformations, heterogeneities often simply rescale the homogeneous nucleation energies. Disconnection nucleation and migration may be driven either through a jump in chemical potential across the GB or by a mechanical stress. Shear stresses drive disconnection migration in much the same way that they drive the motion of lattice dislocations (as described by the Peach-Koehler equation). Chemical potential jumps drive disconnection motion through the motion of atoms across the GB (at steps) from the low to high chemical potential grains. Since shear stress τ couples (is conjugate) to \mathbf{b} and chemical potential jump ψ couples (is conjugate) to h , the nucleation barrier for a pair of disconnections of mode (\mathbf{b}, h) depends on both.

Like most material properties, GB properties are functions of temperature and may change abruptly at temperatures corresponding to phase transitions. Such GB phase transitions may explain the existence of critical temperatures at which abrupt changes in the nature of several physical phenomena occur, including grain growth stagnation (Holm and Foiles, 2010) and superplasticity (Edington et al., 1976).

Several types of GB phase transitions are discussed in the literature. These include thermodynamic phase transitions such as GB structural transitions or faceting/defaceting transitions (which are first-order) (Cantwell et al., 2014; Frolov et al., 2013; Meiners et al., 2020), roughening transitions (divergence in the height-height correlation function) which may be continuous (Rottman, 1986), and improper transitions where the GB transforms from solid-like to glass-like (Zhang et al., 2009). In this dissertation, we discuss a new class of fundamentally different GB phase transitions. We identify a GB topological phase transition of a type of the class originally discussed by Kosterlitz and Thouless (Kosterlitz and Thouless, 1973). Such topological transitions may be thought of as defect binding/unbinding transitions. Disconnections (like dislocations) are topological defects, as seen through a Burgers

circuit analysis (Han et al., 2018).

Below the topological or Kosterlitz-Thouless (KT) transition temperature T_{KT} , the interaction between disconnections is long-range, decaying as the inverse of their separation. The formation and migration of disconnections are severely restricted and GB mobility tends to be small (with important exceptions). On the other hand, above T_{KT} , the long-range elastic field of disconnections is effectively screened. Hence, the KT transition may be viewed as a screening (or sliding) transition, where the screening parameter (dialelastic constant) diverges at T_{KT} . The KT transition leads to abrupt changes in GB migration mobility, roughness, sliding coefficient, etc.

1.2. Thesis Overview

The work described in this thesis investigates GB mobility, shear coupling, topological phase transition, and their implications on grain growth. Parts of this thesis were adapted from Chen et al. (2019, 2020a,b,c), where K. Chen, J. Han, X. Pan, and D.J. Srolovitz designed research, performed research, and wrote the paper; K. Chen performed simulations and analyzed data.

Chapter 2 studies the temperature and driving force dependence of GB shear coupling factor. Shear coupling implies that all GB migration necessarily creates mechanical stresses/strains and is a key component to the evolution of all polycrystalline microstructures. We present MD simulation data and theoretical analyses that demonstrate that GB shear coupling is not an intrinsic GB property, but rather strongly depends on the type and magnitude of the driving force for migration and temperature. We resolve this apparent paradox by proposing a microscopic theory for GB migration that is based upon a statistical ensemble of line defects (disconnections) that are constrained to lie in the GB. Comparison with the MD results for several GBs provides quantitative validation of the theory of shear coupling factor as a function of stress, chemical potential jump and temperature. This chapter was adapted from Chen et al. (2019), where K. Chen, J. Han, S.L. Thomas, and D.J. Srolovitz designed research, performed research, and wrote the paper; K. Chen performed simulations

and analyzed data.

Chapter 3 proposes the concept of GB mobility tensor. GB mobility relates GB velocity to the driving force. While the GB velocity is normally associated with the motion of the GB normal to the GB plane, there is often a tangential motion of one grain with respect to the other across a GB; i.e., GB velocity is a vector. Grain boundary motion can be driven by a jump in chemical potential across a GB or by shear applied parallel to the GB plane; the driving force has three components. Hence, GB mobility must be a tensor (the off-diagonal components indicate shear coupling). Performing MD simulations on a symmetric tilt GB in copper, we demonstrate that all six components of the GB mobility tensor are non-zero (the mobility tensor is symmetric, as required by Onsager). We demonstrate that some of these mobility components increase with temperature while, surprisingly, others decrease. We develop a disconnection dynamics-based statistical model that suggests that GB mobilities follow an Arrhenius relation with respect to temperature T below a critical temperature T_c and decrease as $1/T$ above it. T_c is related to the operative disconnection mode(s) and its (their) energetics. For any GB, which disconnection modes dominate depends on the nature of the driving force and the mobility component of interest. Finally, we examine the impact of the generalization of the mobility for applications in classical capillarity driven grain growth. We demonstrate that stress generation during GB migration (shear coupling) necessarily slows grain growth and reduces GB mobility in polycrystals. This chapter was adapted from Chen et al. (2020a), where K. Chen, J. Han, X. Pan, and D.J. Srolovitz designed research, performed research, and wrote the paper; K. Chen contributed new analytic tools; K. Chen and J. Han analyzed data.

Chapter 4 studies the temperature dependence of GB mobility. The GB mobility relates GB velocity to the thermodynamic driving forces and is central to our understanding of microstructure evolution in polycrystals. Recent MD and experimental studies have shown that the temperature dependence of GB mobility is much more varied than is commonly thought. Grain boundary mobility may increase, decrease, remain constant or show multiple

peaks with increasing temperature. We propose a mechanistic model for GB migration, based on the formation and migration of line defects (disconnection) within the GB. We implement this model in a kinetic Monte Carlo and statistical mechanics framework; the results capture all of these observed temperature dependencies and are shown to be in quantitative agreement with each other and direct MD simulations of GB migration for a set of specific GBs. Examination of the dependence of GB mobility on disconnection mode and temperature provides new insight into how GBs migrate in polycrystalline materials. This chapter was adapted from Chen et al. (2020b), where K. Chen, J. Han, and D.J. Srolovitz designed research, performed research, and wrote the paper; K. Chen performed simulations and analyzed data.

Chapter 5 proposes a topological phase transition of disconnections in GB. The formation and migration of disconnections (line defects constrained to the GB plane with both dislocation and step character) control many of the kinetic and dynamical properties of GBs and the polycrystalline materials of which they are central constituents. We demonstrate that GBs undergo a finite-temperature, dynamical, topological phase transition of the KT type. The phase transition corresponds to the screening of the long-range interactions between (and unbinding of) disconnections. This phase transition leads to abrupt change in GB mobility, GB sliding, and roughening. We analyze this KT transition through mean-field theory, renormalization group methods, and kinetic Monte Carlo simulation and examine how this transition affects microstructure-scale phenomena such as grain growth stagnation, abnormal grain growth and superplasticity. This chapter was adapted from Chen et al. (2020c), where K. Chen, J. Han, and D.J. Srolovitz designed research, performed research, and wrote the paper; K. Chen performed simulations and analyzed data.

CHAPTER 2 : Grain Boundary Shear Coupling

This chapter was adapted from Chen et al. (2019), where K. Chen, J. Han, S.L. Thomas, and D.J. Srolovitz designed research, performed research, and wrote the paper; K. Chen performed simulations and analyzed data.

Grain boundary (GB) motion is central to a wide range of microstructure evolution processes, including normal grain growth, abnormal grain growth, primary recrystallization, and sintering. These processes may be driven by different factors; e.g., stress, injection of defects from within the grains, capillarity (surface tension), and differences in defect densities or elastic energy (across the GB). Shear coupling refers to the motion of GBs driven by shear across the GB plane or, equivalently, the displacement of one grain relative to the other during GB migration. While shear coupling was first observed over 60 years ago (Li et al., 1953; Bainbridge et al., 1954; Biscondi and Goux, 1968), interest in this topic has grown considerably in the past decade. Shear coupling has been reported in both metals (e.g., Al (Biscondi and Goux, 1968; Fukutomi et al., 1991; Winning et al., 2001, 2002; Winning and Rollett, 2005), Zn (Li et al., 1953; Bainbridge et al., 1954)) and ceramics (e.g., cubic zirconia (Yoshida et al., 2004)). Grain boundary sliding is, in some sense, the absence of shear coupling (shear across the grain boundary produces no migration). Grain boundary sliding has been observed in a wide range of polycrystalline systems (e.g., see Sheikh-Ali et al. (2003)). These experimental observations of shear coupling and grain boundary sliding have been reproduced in a wide-range of atomic-scale simulations (e.g., see Molteni et al. (1996, 1997); Hamilton and Foiles (2002); Chen and Kalonji (1992); Shiga and Shinoda (2004); Chandra and Dang (1999); Haslam et al. (2003); Sansoz and Molinari (2005); Cahn et al. (2006); Thomas et al. (2017)).

The shear coupling factor $\beta = v_{\parallel}/v_{\perp}$ is the ratio of the shear rate across the GB (v_{\parallel}) to the normal (migration) velocity of the GB (v_{\perp}). Interestingly, there are many examples in which molecular dynamics (MD) simulations of shear coupling under a fixed shear strain

rate (Cahn et al., 2006) and those performed based on a synthetic driving force (Homer et al., 2013) show very different values of β for the same grain boundary. (A synthetic driving force is a simulation method for producing a jump in chemical potential across a GB; physically, such jumps may result from the capillarity/Gibbs-Thompson effect, differences in defect densities, and differences in elastic strain energy differences associated with elastic anisotropy.) Additionally, both simulations (Cahn et al., 2006) and experiments (Gorkaya et al., 2010) demonstrate that β is often temperature dependent; i.e., in some cases, $\beta \rightarrow \infty$ at high temperature - GB sliding. In this paper, we examine how β varies with the type of driving force, the magnitude of the driving force, and temperature. In particular, we perform MD simulation of GB motion driven by an applied shear stress, an applied shear strain rate (the more widely used), and a jump in chemical potential across the GB for different driving force magnitudes and temperature for several crystallographically distinct GBs. In short, we find that β varies with all three of these factors (type and magnitude of the driving force and temperature). We propose an approach to understand these observations based upon the microscopic mechanism of GB migration, i.e., disconnection motion (Han et al., 2018), as well as the competition between different disconnection modes (Thomas et al., 2017). Based on this approach, we make quantitative predictions of how shear coupling varies with both the type and magnitude of the driving force and with temperature and validate these predictions against our MD results.

2.1. Simulation Method

The mechanical deformation of a polycrystal, whether under stress or strain-control, results in non-uniform stresses and strains within the sample. Strain-controlled and stress-controlled loading can lead to very different deformation behavior. In computer modeling and theoretical treatments of the reaction of grain boundaries to mechanical deformation, the loading is most commonly applied under fixed strain-rate conditions (Cahn et al., 2006). Bicrystal shear coupling experiments are most commonly performed under fixed stress (Rupert et al., 2009). In the present study, we investigate the difference in shear coupling associated with fixed stress and fixed strain rate loading. Constant stress simulations are

more easily analyzed in a statistical mechanics framework (see below) than their constant strain rate counterparts.

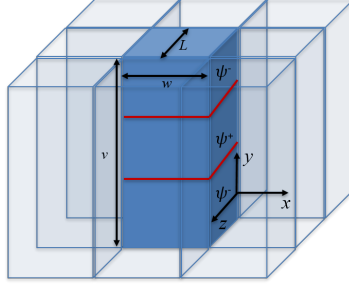


Figure 1: The periodic simulation cell containing two equivalent symmetric tilt GBs shown in red (periodicity only shown in the x - and z -directions). The tilt axis is parallel to z and the GB plane is nominally x - z .

We perform MD simulations of several symmetric tilt GBs in copper within the Large-scale Atomic/Molecular Massively Parallel Simulator (LAMMPS) (Plimpton, 1995) using periodic boundary conditions and a copper EAM interatomic potential (Mishin et al., 2001). In particular, we examine symmetric tilt GBs with tilt axis $[hkl]$, and GB plane (mno) ; i.e., $\Sigma 5[001](310)$, $\Sigma 13[001](510)$, $\Sigma 37[001](750)$ and the $\Sigma 7[111](12\bar{3})$. The simulation cell, shown in Fig. 1, is periodic in all directions, where a pair of nominally flat, parallel GBs have normal y and the tilt axis is parallel to z . For a $[hkl](mno)$ GB, our periodic unit cells has dimensions $w = an_w\sqrt{m^2 + n^2 + o^2}$ (x -direction), $v = an_v\sqrt{(ko - ln)^2 + (lm - ho)^2 + (hn - km)^2}$ (y -direction) and $L = an_L\sqrt{h^2 + k^2 + l^2}$ (z -direction), where a is the cubic cell lattice parameter, $n_L = 3$, and n_w and n_x are integers chosen to make $w \sim 25$ nm and $v \sim 100$, respectively.

We construct GBs by fixing the misorientation of the two crystals and the GB plane and minimize the energy with respect to atomic coordinates and the relative translations of the upper grain relative to the lower grain parallel to the GB plane. We then rescale all atomic coordinates in accordance with temperature-dependent lattice constant prior to simulations at any temperature. Before applying a driving force, we equilibrate the bicrystal system at the temperature of interest for 0.2 ns.

A constant shear stress σ_{xy} is applied, while the other elastic fields satisfy: $\sigma_{yz} = \sigma_{yy} = 0$ and $\epsilon_{xx} = \epsilon_{zz} = \epsilon_{xz} = 0$. We also perform MD simulation in exactly the same simulation cells at fixed shear strain rate $\dot{\epsilon}_{xy}$ together with $\sigma_{yz} = \sigma_{yy} = 0$ and $\epsilon_{xx} = \epsilon_{zz} = \epsilon_{xz} = 0$. Additional MD simulations are performed in which GB migration is driven by a jump in chemical potential ψ ($= \psi^+ - \psi^-$, where ψ^\pm indicate the chemical potential above/below the GB) across the GB while keeping $\sigma_{yz} = \sigma_{yy} = 0$ and $\epsilon_{xx} = \epsilon_{zz} = \epsilon_{xz} = 0$ (i.e., a synthetic driving force (Janssens et al., 2006)). All simulations are 7 ns in duration at temperatures in the 600 – 1300 K range. (Note: we employ larger driving forces for the $\Sigma 13(510)$ GB than the others because the mobility of this boundary is considerably lower than the others.) The GB position is determined as the maximum in the x – y layer-averaged centro-symmetry parameter (Kelchner et al., 1998) in the direction normal to the GB plane using the visualization package OVITO (Stukowski, 2010). The shear coupling factor β for the two GBs in the simulation cell are measured separately from the ratio of the translation rate of the grains parallel to the GB to that of the normal velocity of the mean GB plane. The top and bottom of the error bars in all of the β plots below indicate the values for each of the two GBs in the MD simulations. (The standard deviation of β is half the difference of these two measurements.)

2.2. Mechanically-Driven Shear Coupling

Figure 2 shows the inverse shear coupling factor β^{-1} versus temperature for shear stress ($\sigma_{xy} = \tau$) driven migration of three symmetric tilt grain boundaries. In all cases, $|\beta^{-1}|$ decreases with increasing temperature. While this decrease is particular evident for the $\Sigma 5(310)$ and $\Sigma 13(510)$ GBs, the $\Sigma 37(750)$ is nearly temperature independent until very near the melting point ($T_m = 1327$ K for this interatomic potential (Mishin et al., 2001)). This tendency is consistent with earlier simulations in fixed strain rate-driven shear coupling (e.g., see Cahn et al. (2006)). The decrease in $|\beta^{-1}|$ with increasing temperature is consistent with the widely known increase in the grain boundary sliding rate with increasing temperature (Cahn et al., 2006).

Figure 3 shows the inverse shear coupling factor β^{-1} versus temperature for fixed shear

strain rate $\dot{\epsilon}_{xy}$ driven migration of the same three symmetric tilt grain boundaries, where the open circles are from (Cahn et al., 2006) and the diamonds are from the present work. Since the simulation cell size was not given explicitly in (Cahn et al., 2006), we estimate the shear rate employed based on the bicrystal size (7 nm - in the direction normal to the GB plane) from the figures (Cahn et al., 2006) and the given shear velocity; i.e., $\dot{\epsilon}_{xy} \sim 10^8/s$. Our simulation cell was approximately ten times larger and the shear strain rate is \sim an order of magnitude smaller (our simulation cell also was periodic in the direction normal to the GB plane and contained two GBs. When applying constant strain rate $\dot{\epsilon}_{xy}$, we shear the simulation cell at a constant rate while (Cahn et al., 2006) apply constant velocities to atoms in the top and bottom regime of the simulation cell. The two data sets for the same (510) GB show similar tendencies although the lower strain rate data exhibits smaller

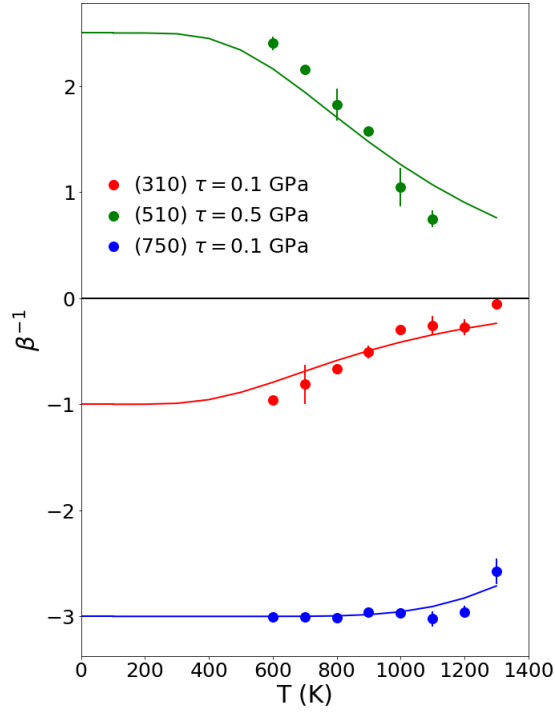


Figure 2: Temperature dependence of the inverse shear coupling factor β^{-1} for shear stress-driven migration of three [001] symmetric tilt grain boundaries, $\Sigma 5(310)$, $\Sigma 13(510)$, and $\Sigma 37(750)$. The circles indicate the mean value of β^{-1} for two GBs (the individual values of β^{-1} are the top and bottom of the error bars which are not visible when their difference is smaller than the size of the circle). The continuous curves are from the fits to Eq. (2.2) and (2.3) for each GB.

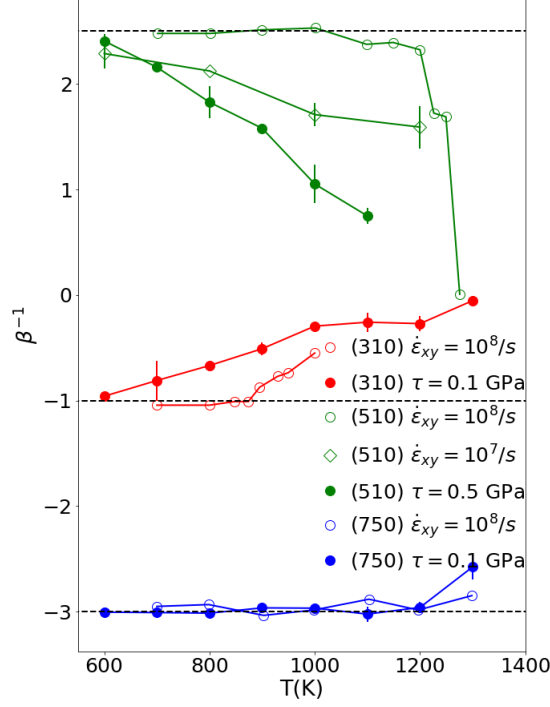


Figure 3: The temperature dependence of the inverse coupling factor β^{-1} is different under constant stress and strain rate. Constant stress MD data and diamond symbol constant strain rate data are averaged over 2 GBs. The open circles correspond to the constant strain rate (fixed end boundary condition) MD data from (Cahn et al., 2006). The open diamond symbols show constant strain rate simulation results under periodic boundary conditions. The horizontal black dashed lines indicate the values of β^{-1} for $T \rightarrow 0$.

values of β^{-1} than those at larger strain rate.

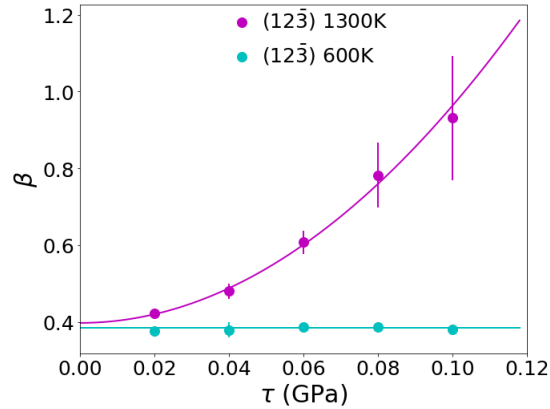


Figure 4: Coupling factor versus shear stress for the $\Sigma 7[111](12\bar{3})$ symmetric tilt GB. The data points are represent the mean for 2 GBs. The continuous curve is the best fit parabola to these data, as suggested by Eq. (2.4).

Figure 3 also shows a comparison between the shear coupling factors obtained under constant stress and constant strain rate conditions. The stress-driven migration simulations were performed using the same simulation cell size and periodic boundary conditions as in our fixed strain rate simulations. These data show that the absolute value of the inverse coupling factor $|\beta^{-1}|$ is larger for the fixed strain rate simulations than for the fixed stress simulations for the (310) and (510) GBs (since β^{-1} for the (750) GB is nearly temperature-independent, no conclusions can be drawn from this GB). In addition, in almost every case, the variation of the slope of the absolute value of the inverse coupling factor with temperature ($\partial|\beta^{-1}|/\partial T$) is larger for the fixed stress simulations than for the fixed strain rate simulations. The fact that β varies with temperature implies that the amount of GB sliding associated with GB migration varies with temperature. This implies that in a constant applied strain rate case, the steady-state shear stress is temperature dependent. And, correspondingly, in a constant applied shear stress case, the strain rate is a function of temperature. The fact that constant stress and constant strain rate loading give different results is not surprising in light of the differences in stress-strain response under different loading conditions during plastic deformation. A quantitative model describing the dependence of the shear coupling factor on both temperature and the magnitude of the mechanical loading is presented below.

Figure 4 shows that at low temperature, the coupling factor β for the $\Sigma 7[111](12\bar{3})$ symmetric tilt GB is controlled by GB geometry and is independent of mechanical load; but the coupling factor β is a function of the magnitude of shear stress at high temperature.

2.3. Chemical Potential Jump-Driven Shear Coupling

Shear coupling may also occur during GB migration when it is induced by non-mechanical driving forces. Following Janssens et al. (Janssens et al., 2006), we simulate GB migration driven by a jump in chemical potential across the GB, ψ , under periodic boundary conditions where the entire simulation cell may shear to maintain zero-net shear stress. Figure 5 shows the temperature dependence of the shear coupling factor for this driving force for the same three GBs discussed above. For the $\Sigma 13(510)$ GB, β decreases with increasing

temperature, while for the $\Sigma 5(310)$ and $\Sigma 37(750)$ GBs, the coupling factor is nearly temperature independent. This is in stark contrast with $\beta(T)$ for the mechanically-driven GB migration results in Fig. 2, especially for the $\Sigma 5(310)$ and $\Sigma 13(510)$ GB cases (we provide a direct comparison in Fig. 7).

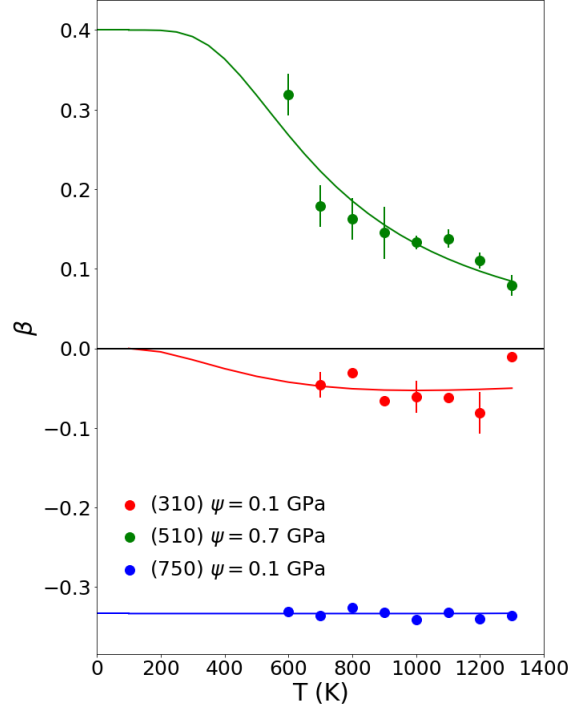


Figure 5: Temperature dependence of the coupling factor β for three GBs driven by a constant chemical potential jump under zero net shear stress conditions. The continuous curves are fits of the data to Eqs. (2.2) and (2.3) for each GB.

Figure 6 shows that at low temperature, the coupling factor β for the $\Sigma 7[111](12\bar{3})$ symmetric tilt GB is controlled by GB geometry and is independent of chemical potential jump; but the coupling factor β is a function of the magnitude of the chemical potential jump at high temperature (this effect is particularly striking for this GB). While larger driving force leads to larger magnitude coupling factors $|\beta|$ under mechanical driving forces (see Fig. 4), larger chemical potential jump-driving forces lead to smaller magnitude coupling factors $|\beta|$. A quantitative model describing the dependence of the shear coupling factor on both temperature and the magnitude of the chemical potential jump is presented below.

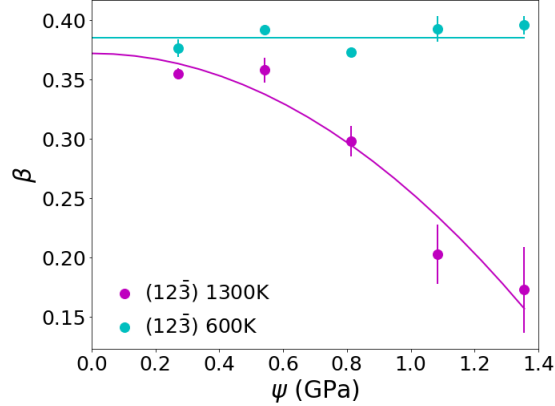


Figure 6: Coupling factor versus chemical potential jump for the $\Sigma 7[111](12\bar{3})$ symmetric tilt GB. The data points represent the mean for 2 GBs. The continuous curve is the best fit parabola to these data, as suggested per Eq. (2.5).

Figure 7 shows a direct comparison of the shear coupling factors for different types of driving forces; i.e., shear stress and chemical potential jump. (We plot this on a logarithmic-scale, $\ln(1 + |\beta|)$ vs. T , to fit all of these data on one plot.) For the $\Sigma 5(310)$ GB, the stress and chemical potential jump coupling factor data are very different at both low and high temperature; this difference grows with increasing temperature. For the $\Sigma 13(510)$ GB, the values of β for the two types of driving forces are the same at low temperature but diverge at higher temperature. On the other hand, for the $\Sigma 37(750)$ GB, the values of β for the two types of driving forces are nearly the same and temperature independent. We present a microscopic mechanism-based analysis for the mode selection below.

2.4. Statistical Disconnection Model

Disconnections are line defects within an interface that are both dislocations and steps, characterized by a Burgers vector \mathbf{b} and step height h , respectively. For a given GB, permissible combinations (modes) of (\mathbf{b}, h) are completely determined by the bicystallography (Han et al., 2018). While pure step modes ($\mathbf{b} = \mathbf{0}, h \neq 0$) and pure dislocation modes ($\mathbf{b} \neq \mathbf{0}, h = 0$) may exist, these never correspond to both small $b = |\mathbf{b}|$ and $|h|$. GBs migrate through the formation and migration of disconnections. Therefore, grain boundary migration (resulting from step motion along the GB) and lateral grain translation (motion of one grain relative to the other across the GB, resulting from dislocation migration along

the GB) are coupled (e.g., see Cahn et al. (2006); Han et al. (2018)). Disconnection migration may be driven either through a jump in chemical potential across the GB or by a mechanical stress. Shear stresses drive disconnection migration in much the same way that they drive the motion of lattice dislocations (as described by the Peach-Koehler equation). Chemical potential jumps drive disconnection motion through the motion of atoms across the GB (at steps) from the low to high chemical potential grains.

Since shear stress τ couples (is conjugate) to \mathbf{b} and chemical potential jump ψ couples (is conjugate) to h , the nucleation barrier for a pair of disconnections of mode (\mathbf{b}, h) depends on both. Following the detailed discussion of disconnection nucleation in (Han et al., 2018) (for the case of a straight dislocation dipole in an isotropic and periodic system), we write

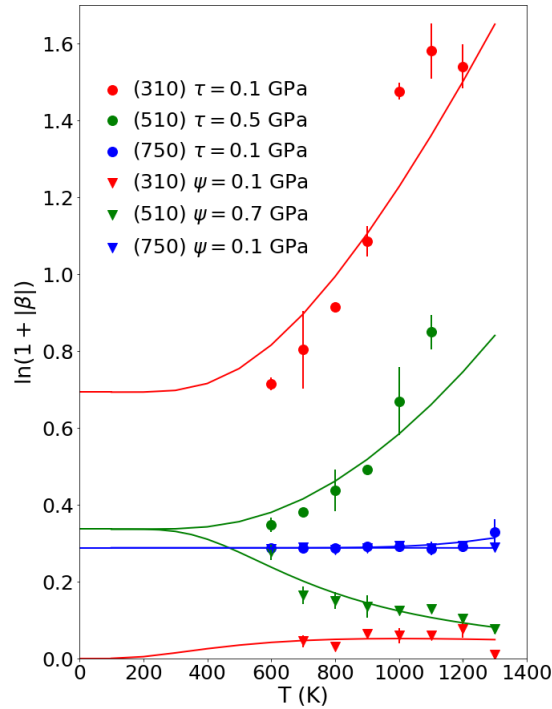


Figure 7: Temperature dependence of the coupling factor β for constant stress and chemical potential jump driving forces. The data are plotted on a logarithmic scale to fit the data meaningfully on one plot. The continuous curves are fits to the constant stress and chemical potential jump data as per Eqs. (2.2) and (2.3) for each GB. Curves are from fitting A and B from Eqs. (2.2) and (2.3) for each GB.

the disconnection nucleation barrier as

$$q = (Ab^2 + B|h|)L - bS\tau + hS\psi, \quad (2.1)$$

where $A = -2G [(1 - \nu \cos^2 \alpha)/4\pi(1 - \nu)] \ln [\sin(\pi r/w)]$ and $B = 2\gamma$. b is the magnitude of the Burgers vector that is conjugate to shear stress τ , γ is the GB energy (per unit area), G and ν are the shear modulus and Poisson's ratio, α is the angle between the Burgers vector and the disconnection line direction, and r is the disconnection core size. In the periodic unit cell employed in the MD simulations, L is the cell dimension parallel to the nominally straight disconnection lines, w is the cell dimension in the direction orthogonal to the disconnection line, and $S = Lw$ is the nominal GB area. A describes the energy required to form a pair of dislocations and separate them to a distance of half the periodic unit cell ($w/2$) (Hirth and Lothe, 1982) and B describes the energy required to form a pair of steps (Han et al., 2018).

Equation (2.1) suggests that mode selection depends on both the magnitude AND type of driving force (stress or chemical potential jump). Large stresses favor modes of large $|\mathbf{b}|$ and small $|h|$, while large chemical potential jumps favor modes of small $|\mathbf{b}|$ and large h (especially the pure step mode with $\mathbf{b} = 0$), resulting in different coupling factors β in these cases; the larger the driving force, the stronger this effect.

Since the disconnection nucleation barrier in Eq. (2.1) depends on \mathbf{b} and h , we should expect that different disconnection modes will have different nucleation rates. This effect may be captured via Boltzmann statistics (Thomas et al., 2017). In this way, we describe the effective shear coupling factor by weighting the coupling factors associated with disconnection

modes i ($\beta_i = b_i/h_i$) by their Boltzmann factors

$$\begin{aligned}\beta &= \frac{\sum_i b_i e^{-\frac{Q_i}{k_B T}} \sinh \frac{(b_i \tau - h_i \psi) S}{k_B T}}{\sum_i h_i e^{-\frac{Q_i}{k_B T}} \sinh \frac{(b_i \tau - h_i \psi) S}{k_B T}} \\ &= \frac{\sum_i b_i e^{-\frac{Q_i}{k_B T}} (b_i \tau - h_i \psi)}{\sum_i h_i e^{-\frac{Q_i}{k_B T}} (b_i \tau - h_i \psi)} + \mathcal{O}\left(\frac{(b \tau - h \psi) S}{k_B T}\right)^2,\end{aligned}\tag{2.2}$$

where the summation is over all crystallographically possible disconnection modes, $k_B T$ is the thermal energy and Q_i is intrinsic disconnection nucleation barrier for the i^{th} disconnection mode (i.e., $Q_i = q$ in the absence of a driving force)

$$\frac{Q_i}{L} = Ab_i^2 + B|h_i|.\tag{2.3}$$

At low temperature, only the disconnection mode with the lowest barrier is activated, while at high temperature, many modes are activated, resulting in β being a function of temperature.

2.4.1. Temperature and Driving Force Type

Before comparing the disconnection model prediction of β with the MD simulation results, we note that the expressions for A and B following Eq. (2.1) represent continuum model descriptions of fundamentally atomic-level and bonding-dependent quantities (related to disconnection core structures). As such, we treat A and B as parameters to be determined by fitting to the simulation data and defer the assessment of how well the analytical expressions for A and B work. We perform nonlinear fits of Eqs. (2.2) and (2.3) to the β data in Figs. 2 (stress driving force) and 5 (chemical potential driving force). To do this, we consider all of the disconnection modes (although we include $\sim 10,000$ different modes for each GB, in practice only the lowest few modes are important) for the $\Sigma 5[001](310)$, $\Sigma 13[001](510)$, and $\Sigma 37[001](750)$ symmetric tilt GBs (see Han et al. (2018) for a description of how to enumerate all possible disconnection modes). The results of this fitting procedure are shown as the continuous curves in Figs. 2 and 5 and in Table 1. Overall, we see that

Eqs. (2.2) and (2.3) are in good agreement with the MD results for both driving forces as a function of temperature. The predicted temperature dependence is especially remarkable giving the simplicity of the Boltzmann weighting of the different disconnection modes; even better agreement should be possible with inclusion of correlation effects, e.g., through the use of kinetic Monte Carlo approaches.

Table 1: Fitting parameters A and B in Eq. (2.3) for the data in Figs. 2 and 5. γ is the GB energy for this potential at 0 K (Mishin et al., 2001). b_i , h_i , and β_i are the Burgers vector, step height, and coupling factor of disconnection mode with the i^{th} lowest barrier (see Eq. (2.3) and the analytical expressions for the parameters). B and γ are in J/m^2 and A is in GPa. b_1 , b_2 , h_1 , and h_2 are in cubic lattice constant units ($a_0 = 0.36 \text{ nm}$). F identifies the driving force type.

GB	F	A	B	2γ	b_1	h_1	β_1	b_2	h_2	β_2
(310)	τ	13	0.39	1.9	$\frac{1}{\sqrt{10}}$	$-\frac{1}{\sqrt{10}}$	-1	$\frac{1}{\sqrt{10}}$	$\frac{3}{\sqrt{40}}$	$\frac{2}{3}$
	ψ	58	0.39		0	$\frac{5}{\sqrt{40}}$	0	$-\frac{1}{\sqrt{10}}$	$\frac{1}{\sqrt{10}}$	-1
(510)	τ	50	0.38	1.9	$\frac{1}{\sqrt{26}}$	$\frac{5}{\sqrt{104}}$	$\frac{2}{5}$	$\frac{1}{\sqrt{26}}$	$-\frac{4}{\sqrt{26}}$	$-\frac{1}{4}$
	ψ	94	0.25		$\frac{1}{\sqrt{26}}$	$\frac{5}{\sqrt{104}}$	$\frac{2}{5}$	0	$\frac{13}{\sqrt{104}}$	0
(750)	τ	36	0.53	1.5	$\frac{1}{\sqrt{74}}$	$-\frac{3}{\sqrt{74}}$	$-\frac{1}{3}$	$\frac{2}{\sqrt{74}}$	$-\frac{6}{\sqrt{74}}$	$-\frac{1}{3}$
	ψ	36	0.53		$-\frac{1}{\sqrt{74}}$	$\frac{3}{\sqrt{74}}$	$-\frac{1}{3}$	$-\frac{2}{\sqrt{74}}$	$\frac{6}{\sqrt{74}}$	$-\frac{1}{3}$

The values of the parameters A and B are of similar magnitude for all three GBs and for both driving forces. In fact, the non-linear fitting procedure employed showed many shallow minima, many of which give fits to the temperature-dependence of β of similar quality. This suggests that the predictions for β based on Eqs. (2.2) and (2.3) are robust (insensitive to which GB in a material, how the GB is driven, ...).

Further examination of Table 1 shows while the values of B obtained by fitting the constant stress and constant chemical potential jump data show little variation (the average difference is less than 15% of the mean value), the value of A is more sensitive to the type of driving force (average error 65%). The value of A depends on dislocation core size r and r roughly scales with Burgers vector b (Hirth and Lothe, 1982). Stress-driven GB dynamics favors

disconnections of large Burgers vector $|\mathbf{b}|$ while GB migration driven by a chemical potential jump favors disconnections of small $|\mathbf{b}|$. In fact, Table 1 shows that the value of A obtained with stress-driven GBs is less than or equal to that obtained when migration is driven by a chemical potential jump - as expected based on this argument. Since the two disconnections with the lowest nucleation barriers for the (750) GB have the same value of β , the effective coupling factor is insensitive to both temperature and driving force (see Table 1 and Figs. 2 and 5).

The analytical expression for A (following Eq. (2.1)) depends on the core size r . Inserting elastic constant data for Cu and using our fitted values of A (Table 1) suggest that $10^{-4} < r < 1$ nm. This result shows that the expression for A is not unreasonable (and that this is not a good way to determine core size). On the other hand, the analytical expression for B (following Eq. (2.1)) is simple and does not depend on disconnection mode: $B = 2\gamma$ (Hirth and Lothe, 1982; Han et al., 2018). Comparison of the values of B from the fitting and 2γ from our atomistic (energy minimization) simulations shows that while the two are within an order of magnitude of one another, the agreement is not outstanding. Hence, the analytical expressions for A and B should be viewed as order of magnitude estimates only. Moreover, if the driving force is too large to linearize Eq.(2.2), fitting A and B using the linearized expression will not be accurate.

Table 1 also gives the disconnection modes corresponding to the two lowest intrinsic nucleation barriers (see Eq. (2.3)) under the two types of driving forces. Note that since the fitted values of A and B may depend on the type of driving force, so may the lowest intrinsic nucleation barrier modes. The disconnections with the lowest intrinsic barriers (b_1, h_1) are the same for both types of driving forces for the (510) and (750) GBs, but for the (310) GB the lowest intrinsic barrier mode is different for the stress and chemical potential jump driving forces. For the second lowest intrinsic barrier mode (b_2, h_2) , only the (750) GB chooses the same mode for both types of driving force. In general, GB migration under a stress driving force favors disconnection modes with larger $|\mathbf{b}|$ and smaller $|h|$ than those

under a chemical potential jump driving force and *vice-versa*.

The temperature dependent coupling factors for the (310), (510) and (750) GBs for stress and chemical potential jump-driven migration (Figs. 2 and 5) may be directly compared in Fig. 7. β for the (750) boundary is remarkably temperature independent (compared with the other GBs) and insensitive to the nature of the driving force. The origin of both effects may be understood by reference to Table 1. For this GB, the coupling factors for the two lowest disconnection nucleation barrier modes are identical ($\beta_1 = \beta_2 = -1/3$). The fact that the lowest barrier mode β_1 is the same for both driving force types implies that the coupling factor for both types of driving force will be identical at low temperature. The fact that the second lowest barrier mode β_2 is the same as β_1 implies that raising the temperature has little effect on β . In fact, the temperature at which we expect to see significant deviations of β from its low temperature value is determined by the difference in barriers between the lowest barrier mode and the next mode with a different value of β . For this GB, the next lowest barrier mode with a different value of β is the fourth lowest (β_4). Since this barrier is much larger than that of β_1 , the effective β deviates from its low temperature value only near the melting point. Finally, since the two lowest disconnection barriers are the same for both types of driving forces, β is independent of driving force type till very close to the melting point.

For the (510) GB, the coupling factors for the lowest disconnection nucleation barrier mode β_1 are identical for both types of driving force. Like for the (750) GB, this implies that as $T \rightarrow 0$, the effective coupling factor for both driving force types are the same. However, as the temperature increases, Fig. 7 shows that the coupling factors for the different driving force types diverge. Table 1 shows that the second lowest barrier modes differ from the lowest barrier modes - this explains why β is temperature-dependent. Table 1 also shows that the second lowest barrier modes are different for different types of driving force - this explains why the $\beta(T)$ curves diverge at intermediate and high temperature.

$\beta(T)$ for the (310) GB exhibits remarkable differences compared with the (750) and (510)

GBs (see Fig. 7). For this GB, in the low temperature limit ($T \rightarrow 0$) β depends on the type of driving force. The behavior as $T \rightarrow 0$ is even more clear based on the continuous curves in Fig. 7 which are from Eq. (2.2). This may be explained by the fact the coupling factor corresponding to the lowest barrier mode β_1 is different for the two types of driving forces (see Table 1); for $T \rightarrow 0$, Eq. (2.2) shows that $\beta \rightarrow \beta_1$. Examination of the second lowest barrier modes (Table 1) shows that the difference between the first and second lowest barrier modes for the chemical potential jump-driving force is smaller (1) than that for the stress driving force (2.5). This explains why the temperature dependence of β for stress-driven migration is stronger than that for chemical potential-driven migration.

2.4.2. Driving Force Magnitude

Although in most studies of the coupling factor it is implicitly assumed that β is insensitive to the magnitude of the driving force, the results in Figs. 4 and 6 indicate that this is not true. Equation (2.2) shows that β depends on driving force. Therefore, expanding β to third order for small driving forces (i.e., $bS\tau/k_B T \ll 1$ or $hS\psi/k_B T \ll 1$), we find that

$$\beta = C^\tau \tau^2 + \beta_0^\tau \quad (2.4)$$

$$\beta = C^\psi \psi^2 + \beta_0^\psi, \quad (2.5)$$

where β_0^x is the zero driving force limit of β for driving force of type x (the justification for Eqs. (2.4) and (2.5) and the analytical expression of constants C^x and β_0^x are given explicitly in the Appendix). This suggests that the assumption that β is independent of the magnitude of the driving force is valid to first order in the driving force. Examination of the MD simulation results shown in Figs. 4 and 6 demonstrate that Eqs. (2.4) and (2.5) provide an excellent fit to the data. At low temperature $T \ll T_c$, $C^x \rightarrow 0$, where $T_c = (Q_2 - Q_1)/k_B$ and Q_i is the i^{th} lowest disconnection nucleation barrier.

As discussed above, stress-driven shear coupling and chemical potential jump-driven shear coupling may have different coupling factors β at small driving forces. While this conclusion is general, it fails (i.e., $\beta_0^\tau = \beta_0^\psi$) when (1) the temperature is low and (2) $\beta_0^\psi \neq 0$ (i.e., the

lowest barrier mode does not correspond to a pure step). This is consistent with all of the MD results in Fig. 7 given the lowest barrier modes shown in Table 1.

The fact that β depends on the magnitude of the driving force explains why β is different under constant stress and constant strain rate loading (see Fig. 3). In the spirit of the derivation of the thermodynamic Maxwell relations (Blundell and Blundell, 2010), we can write

$$\left. \frac{\partial \beta}{\partial T} \right|_{\dot{D}} = \left. \frac{\partial \beta}{\partial T} \right|_{\tau} + \left. \frac{\partial \beta}{\partial \tau} \right|_T \left. \frac{\partial \tau}{\partial T} \right|_{\dot{D}}, \quad (2.6)$$

where \dot{D} is the relative displacement rate of the two grains meeting at the GB (the shear strain rate is \dot{D}/v). We note that $(\partial\tau/\partial T)|_{\dot{D}}$ is non-zero since the shear stress depends on β at fixed displacement rate (and, τ decreases with increasing T). Hence, $(\partial\beta/\partial T)|_{\dot{D}} \neq (\partial\beta/\partial T)|_{\tau}$ simply because $(\partial\beta/\partial\tau)|_T$ is non-zero.

2.5. Conclusions

While grain boundary migration often appears complex, we demonstrated that much of this complexity may be resolved by consideration of the underlying mechanisms by which GBs migrate. The difference between experimentally measured shear coupling factors β (the quantity that relates GB migration to the relative translation of the grains) and geometric predictions (Momprou et al., 2009) can be explained within this framework. We present molecular dynamics results that demonstrate that the temperature-dependence of the grain boundary shear coupling factor β depends on whether the grain boundary is driven by differences (jumps) in chemical potential across the GB, stress, or strain rate. β is also observed to be a function of the magnitude of the driving force. These variations in β can be very large (orders of magnitude) and even lead to changes in sign.

We propose a simple model that quantitatively predicts these variations. Our model is based on the statistical mechanics of disconnection (line defects in the GBs characterized by a Burgers vector and step height) nucleation. After all crystallographically-permissible disconnection modes are predicted for any specific GB, our disconnection nucleation model determines the relative nucleation barriers for each and statistical mechanics determines

the relative rates of formation of each. We apply this theoretical construct to the four GBs examined in our MD simulations and predict which disconnections are most important for each GB and type of driving force (as well as their relative importance). With this information, we directly predict the shear coupling factor as a function of temperature, driving force (type and magnitude), and bicrystallography. These predictions are in excellent quantitative agreement with all of the MD simulation results.

Although it is difficult to identify individual disconnections at high temperature in the MD simulations (and experiments), the disconnection model should be applicable over a wide range of temperature because it rests on bicrystallography rather than any thermodynamic property of the GB structure or the details of the disconnection structure. Since disconnections are topological defects, they are present whether the GB is sharp or rough. While GB sliding may be viewed on a macroscopic level as a failure of ideal shear coupling, it does not imply a failure of the disconnection model. Rather, GB sliding is a direct consequence of the the presence and motion of disconnections with multiple modes.

Although the present work explicitly focused on GB dynamics in bicrystals, shear coupling constrained by multiple grains (and triple junctions) is a key feature of microstructure evolution in polycrystals (including grain size coarsening, grain rotation, stress generation, etc (Thomas et al., 2017)). Disconnections of one mode, moving along GBs in polycrystals, will pile-up at triple junctions, creating back stresses that will prevent macroscopic GB migration. Continued GB (and triple junction) migration requires the participation of disconnections of other modes to ensure that the total Burgers vector is zero at the triple junction (Han et al., 2018). The current work presents a statistical mechanics-based approach that provides the basis for explaining how multiple disconnection modes conspire to move GBs and triple junctions together.

CHAPTER 3 : Grain Boundary Mobility Tensor

This chapter was adapted from Chen et al. (2020a), where K. Chen, J. Han, X. Pan, and D.J. Srolovitz designed research, performed research, and wrote the paper; K. Chen contributed new analytic tools; K. Chen and J. Han analyzed data

Chapter 2 suggests that GB mobility depends on the origin of the driving force for GB migration (stress versus jumps in chemical potential across a GB) because of shear coupling. This dependence contradicts the widely accepted notion that GB mobility is an intrinsic GB property (independent of the source of the driving force). However, if the GB mobility does depend on the nature of the driving force, the notion of a GB mobility should be expanded. The shear-coupling factor (ratio of GB sliding and migration rates) also depends on the nature of the driving force (Chen et al., 2019). Hence, GB motion is associated with three orthogonal displacements (and velocities): GB migration (perpendicular to the GB plane) and translations of one grain with respect to the other (in two directions tangent to the GB plane). Accordingly, there are three generalized forces (per unit area) associated with these motions (variations of the free energy with respect to three displacements). Assuming that the displacements associated with the GB motion are overdamped (an excellent approximation since GB velocities are small compared with all speeds of sound), the proportionality constant between the velocity and force vectors should therefore be a 3×3 mobility tensor, \mathbf{M} . If we establish a coordinate system such that the GB normal is parallel to the \mathbf{e}_1 -axis, then M_{11} is the traditional GB (migration) mobility, M_{1j} ($j \neq 1$) components describe shear coupling, and M_{ij} ($i, j \neq 1$) describe GB sliding. Since M_{ij}/M_{11} is often not small, ignoring these non-traditional mobility tensor components (i.e., replacing \mathbf{M} with the scalar $M_{\text{GB}} = M_{11}$) can be inappropriate. Also note that the individual components of \mathbf{M} may have different temperature dependences.

Here, we employ molecular dynamics (MD) simulations to examine the individual components of the GB mobility tensor \mathbf{M} and their temperature dependences for a $\Sigma 7$ [111] (12 $\bar{3}$)

GB in face centered cubic (FCC) copper. We focus on this relatively simple low- Σ symmetric tilt GB as an example to demonstrate the main effects/principles (additional MD data, not reported here, suggests that the same conclusions apply broadly). We then develop a general statistical disconnection-based analytical model to understand the temperature dependence of the GB mobility tensor \mathbf{M} .

3.1. Generalized GB Kinetics

Consider the bicrystal schematic in Fig. 8, where the GB separates Grains A and B. The normal displacement of the GB (i.e., the GB migration distance) is u_1 in the x_1 -direction. The displacements of Grain A with respect to Grain B along two orthogonal directions in the GB plane (x_2 and x_3) are u_2 and u_3 , respectively. Thus, we define a generalized displacement $\mathbf{u} = (u_1, u_2, u_3)$ with a corresponding generalized velocity $\mathbf{v} = \dot{\mathbf{u}}$. The generalized driving force conjugate to the generalized velocity is $\mathbf{F} = -\partial G/\partial \mathbf{u}$, where G is the free energy per area of the GB. The first component of \mathbf{F} is $F_1 = -\partial G/\partial u_1 = \psi$, which is the jump of chemical potential (free energy density) across the GB. The second and third components of \mathbf{F} are $F_2 = \sigma_{12} \equiv \tau_2$ and $F_3 = \sigma_{13} \equiv \tau_3$, which are shear stresses along the x_2 - and x_3 -directions in the GB plane. The GB mobility tensor, relating \mathbf{v} and \mathbf{F} , i.e.,

$$\mathbf{v} = \mathbf{M}\mathbf{F} \tag{3.1}$$

is a second-rank tensor; more explicitly,

$$\begin{pmatrix} v_1 \\ v_2 \\ v_3 \end{pmatrix} = \begin{pmatrix} M_{11} & M_{12} & M_{13} \\ M_{21} & M_{22} & M_{23} \\ M_{31} & M_{32} & M_{33} \end{pmatrix} \begin{pmatrix} \psi \\ \tau_2 \\ \tau_3 \end{pmatrix}. \tag{3.2}$$

Since GB kinetics are overdamped, GB motion is consistent with the maximum energy dissipation rate and, as required by the Onsager relation (Onsager, 1931), the GB mobility tensor \mathbf{M} should be symmetric and positive definite (see below).

The shear-coupling factor (the ratio of the shear velocity to the GB migration velocity)

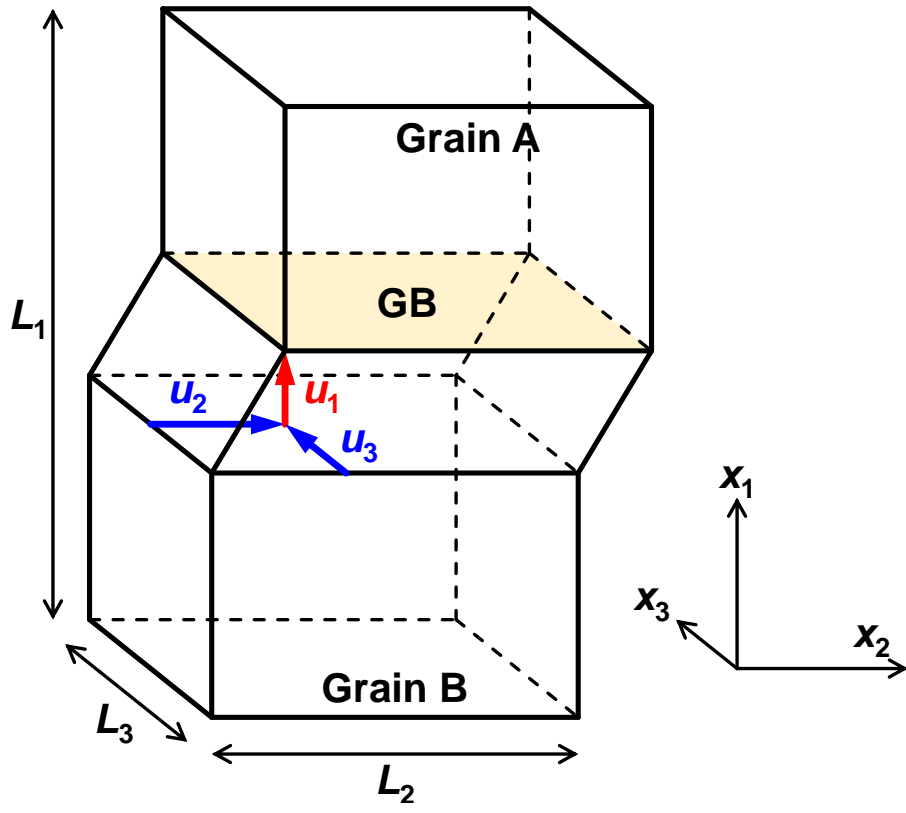


Figure 8: Bicrystal simulation cell with a symmetric tilt GB (shaded yellow). The tilt axis is parallel to x_3 and the GB plane is nominally x_2 - x_3 . The cell is periodic in the x_2 - and x_3 -directions and a thin, rigid perfect crystal layer is added to the top and bottom surfaces which may displace freely.

has two components $\beta_k = v_k/v_1$ corresponding to orthogonal shear directions. This factor can be obtained by measuring v_1 and v_k under an applied shear stress τ_k ; according to Eq. (3.2), such a factor is $\beta_k = M_{kk}/M_{1k}$. β_k can also be determined by measuring v_1 and v_k when GB migration is driven by a jump in the chemical potential across the GB ψ (e.g., a synthetic driving force such as often employed in MD simulations or associated with capillarity); the factor measured in this way is $\beta_k = M_{1k}/M_{11}$. Coupling factors β_k measured in these two manners are naturally different (Chen et al., 2019) (see Appendix).

3.2. Simulation Methods

We performed MD simulations using the Large-scale Atomic/Molecular Massively Parallel Simulator (LAMMPS) (Plimpton, 1995) and a copper embedded-atom-method potential (Mishin et al., 2001) for several different GBs (Chen et al., 2019). While these simulations (Chen et al., 2019) show qualitatively similar results, we focus on one particular GB in this paper; i.e., the $\Sigma 7$ [111] ($12\bar{3}$) symmetric tilt GB. In these simulations the tilt axis is parallel to the x_3 -direction and the cell dimensions are $L_1 \sim 100$ nm, L_2 and $L_3 \sim 5$ nm.

We construct GBs by fixing the misorientation of the two grains and minimizing the energy with respect to atomic coordinates and the relative translations of the upper grain relative to the lower grain. We then rescale all atomic coordinates in accordance with the temperature-appropriate lattice constant prior to beginning the MD simulations. Before applying a driving force, we equilibrate the bicrystal system at the temperature of interest for 0.2 ns. In the simulations of stress-driven GB migration, we apply a constant shear stress τ_2 or τ_3 by imposing forces on the top and bottom surfaces of F_2 or F_3 . Additional MD simulations are performed in which GB migration is driven by a jump in the chemical potential ψ ; i.e., an additional energy density $\pm\psi/2$ was added to the atoms in Grains A and B, respectively (i.e., a synthetic driving force (Janssens et al., 2006)). Much larger driving forces were employed to drive GB motion using applied shear stresses as compared with chemical potential jumps in order to obtain reliable mobility measurements (as seen below, the mobilities obtained for small and large driving forces are consistent). All simulations were run for 7 ns at temperatures in the 600-1300 K range at fixed number of atoms

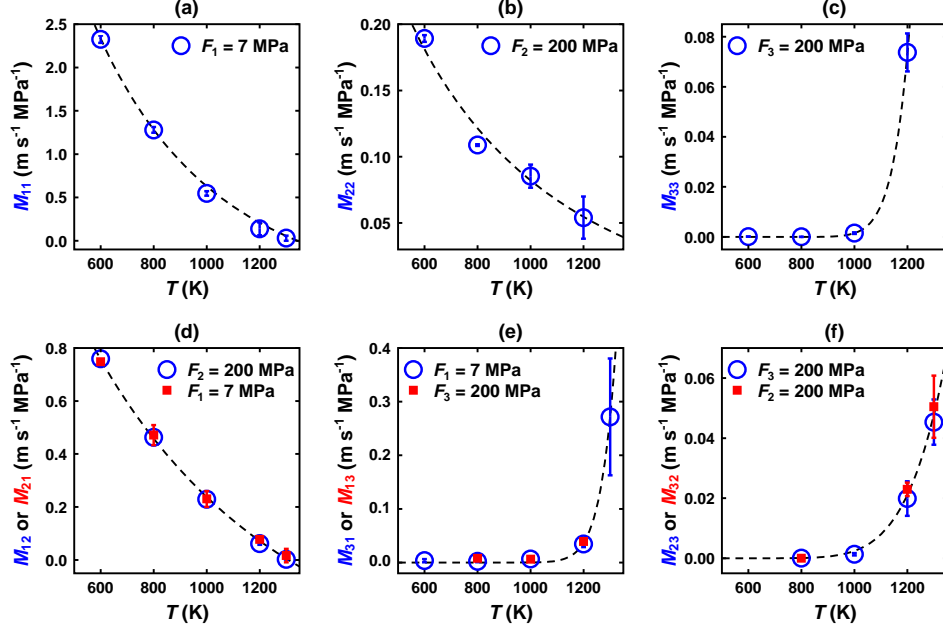


Figure 9: Temperature dependences of the GB mobility components (a) M_{11} , (b) M_{22} , (c) M_{33} , (d) M_{12} , (e) M_{13} , and (f) M_{23} (error bars indicate the range of the simulation results). The data points represent the MD results and the dashed lines are fits of these data to Eq. (3.5) for a single disconnection mode. For the off-diagonal components of M_{ij} ($i \neq j$), two sets of data points (blue circles and red squares) are shown corresponding to M_{ij} and M_{ji} ; the Onsager relation suggests that these two sets of data are equivalent.

and temperature (Nosé-Hoover thermostat on all but the fixed-atoms). The GB position is defined as the x_1 position where the layer-averaged centro-symmetry parameter (Stukowski, 2010) is maximum (Kelchner et al., 1998). The GB migration velocity is the normal velocity of the mean GB plane. The “error” bars in the GB mobility data depict the values obtained from two identical simulations.

3.3. Simulation Results

Figure 9 shows the temperature dependence of each of the GB mobility components M_{ij} . The magnitudes of these components can vary by several orders; $M_{11} > M_{1i} > M_{22} > M_{33}$. The temperature dependences of these GB mobility components also differ widely. The components which involve the displacement along the tilt axis (M_{31} , M_{32} and M_{33}) increase rapidly with increasing temperature (see Figs. 9c, e and f), while the other components (M_{11} , M_{12} and M_{22}) decrease with increasing temperature (see Figs. 9a, b and d).

The observation that the diagonal components M_{11} and M_{22} decrease with increasing temperature seems counterintuitive. But, such situations are, in fact, not unusual; in the MD data set of 388 distinct GBs, Olmsted et al. (2009); Homer et al. (2014) reported such behavior for many GBs (they call this anti-thermal behavior). The origin of this surprising temperature dependence of several GB mobility components is discussed below.

Examination of Figs. 9d, e and f clearly demonstrates that $M_{12} = M_{21}$, $M_{13} = M_{31}$ and $M_{23} = M_{32}$, as required by the Onsager reciprocal relation (Onsager, 1931). Coupling does not only exist between GB migration and shear but also between shears in different directions; i.e., a shear stress in one direction may produce shear displacement along the orthogonal direction, i.e., in general, $M_{23} \neq 0$. Note that in the symmetric tilt GB example which we focus on in this report, M_{23} is small compared with the other mobility components.

3.4. Statistical Disconnection Model

GB motion is accomplished through the glide of line defects (i.e., disconnections) along the GB (Han et al., 2018); such disconnection mechanism has been directly supported by the in-situ experimental observation of GB migration in polycrystals by Legros and colleagues (Legros et al., 2008; Momprou et al., 2009; Rajabzadeh et al., 2013a). Disconnections are constrained to lie within the GB and are characterized by a Burgers vector \mathbf{b} (dislocation character) and a step height h (step character); both of these are translation vectors of the displacement shift complete (DSC) lattice (Sutton and Balluffi, 1995; Han et al., 2018). For each GB with a particular bicystallography, there are multiple disconnection modes (\mathbf{b}_m, h_m) (Han et al., 2018) (the subscript denotes one of the disconnection modes allowed by the bicystallography).

Disconnections may be introduced into GBs via homogeneous or heterogeneous nucleation and/or by the decomposition of lattice dislocations. In this discussion, we focus on homogeneous nucleation since, as in phase transformations, heterogeneities often simply rescale the homogeneous nucleation energies. Since disconnection formation and migration may be driven by different types of driving force which couple to the disconnection (\mathbf{b}_m, h_m) ,

the disconnection dipole formation energy depends on the disconnection mode. Following earlier discussions of disconnection formation/nucleation (Han et al., 2018; Thomas et al., 2017; Chen et al., 2019), we can write the disconnection formation barrier as

$$E^* = Q - W \equiv (Ab^2 + B|h| + C)L - \mathbf{H} \cdot \mathbf{F}L^2/2, \quad (3.3)$$

where Q is the formation barrier without a driving force, W is the work done by the driving force, $\mathbf{H} \equiv (h, b_2, b_3)^T$, and $L = L_2 = L_3$. The constants may be estimated (Han et al., 2018) as $A = -2\mu [(1 - \nu \cos^2 \alpha)/4\pi(1 - \nu)] \ln \sin(\pi r_0/L)$ and $B = 2\gamma$, where γ is the step energy, μ is the shear modulus, ν is the Poisson's ratio, α is the angle between the Burgers vector and the disconnection line direction, and r_0 is the disconnection core size. A describes the energy required to form a dislocation pair and separate it to a distance of half the periodic unit cell $L/2$ (Han et al., 2018) and B describes the energy required to form a pair of steps (Thomas et al., 2017; Han et al., 2018; Chen et al., 2019). C represents the disconnection migration barrier which depends on the GB structure and bonding character; this is dominated by core-level phenomena and may be determined via calculations on the atomic scale (Combe et al., 2016). We emphasize that in our approach, we view a flat GB as reference configuration and curvature is directly represented by a distribution of step/disconnection (pairs) along the reference GB. While a macroscopically curved GB is appropriately viewed as flat on the scale of MD simulations (except for nano-grained microstructures), we still capture this macro-curvature driving force as a jump of chemical potential (i.e., ψ as a component of \mathbf{F}); this is consistent with the classical Gibbs-Thomson effect where GB curvature induces a pressure driving force on a GB - driving force and chemical potential jump are simply two equivalent approaches for describing the thermodynamics of GB curvature-induced GB migration.

Since the disconnection formation barrier (Eq. (3.3)) depends on both \mathbf{b} and h , disconnections of different modes have different formation rates. We implicitly assume that the GB velocity is disconnection formation-controlled (i.e., the disconnection formation barrier

is large compared with the migration barrier) and describe the temperature dependence of the disconnection formation rates based upon Boltzmann statistics (Thomas et al., 2017; Chen et al., 2019) (this is not always a good assumption (Combe et al., 2016)). Hence, the GB velocity is obtained by superimposing contributions from different disconnection modes, weighted by their Boltzmann factors:

$$\begin{aligned} \mathbf{v} &= 2f_0 \sum_m \mathbf{H}^{(m)} e^{-Q^{(m)}/k_{\text{B}}T} \sinh \left(\frac{\mathbf{H}^{(m)} \cdot \mathbf{F} L^2}{2k_{\text{B}}T} \right) \\ &\approx \left(\frac{f_0 L^2}{k_{\text{B}}T} \sum_m \mathbf{H}^{(m)} \otimes \mathbf{H}^{(m)} e^{-Q^{(m)}/k_{\text{B}}T} \right) \mathbf{F}, \end{aligned} \quad (3.4)$$

where f_0 is the attempt frequency, the superscript m denotes the m^{th} disconnection mode, and the expression in the second line of Eq. (3.4) is an expansion to leading order in $\mathbf{F} L^2/T$. Therefore, the GB mobility tensor is

$$\mathbf{M} = \frac{f_0 L^2}{k_{\text{B}}T} \sum_m \mathbf{H}^{(m)} \otimes \mathbf{H}^{(m)} e^{-Q^{(m)}/k_{\text{B}}T}. \quad (3.5)$$

Eq. (3.5) guarantees that $\mathbf{M} = \mathbf{M}^T$, the determinant $|\mathbf{M}| > 0$, the diagonal components M_{11} , M_{22} and M_{33} are each positive, and generally $M_{ij} \neq 0$. We also note that because of the temperature-dependent prefactor and the summation over modes, M_{ij} is, in general, non-Arrhenius. If only one mode is active, M_{ij} will reach maximum at $T = T_c \equiv Q^{(1)}/k_{\text{B}}$. For $T < T_c$, M_{ij} will be nearly Arrhenius, while for $T > T_c$, the temperature dependence of M_{ij} is dominated by the prefactor $1/T$. This suggests that M_{ij} may decrease with increasing temperature for $T > T_c$.

Since the [111] tilt axis is a close-packed direction in our material (FCC copper), the modes with Burgers vector \mathbf{b} parallel to the tilt axis (x_3) tend to have much larger values of $|\mathbf{b}|$ and, thus, larger Q (see Eq. (3.3)) than the modes with \mathbf{b} perpendicular to the tilt axis (x_2). The large difference in Q between the shears in the directions parallel and perpendicular to the tilt axis makes the investigated temperature range (600-1300 K) smaller than T_c for the former and larger than T_c for the latter. This results in qualitatively different temperature

dependences of the mobility components M_{3i} ($i = 1, 2, 3$) and M_{jk} ($j, k = 1, 2$). For M_{3i} (shearing in x_3), $T < T_c$ such that $M_{3i}(T)$ is nearly Arrhenius; in qualitative agreement with the MD results (Figs. 9c, e and f). For M_{jk} (shearing in x_1 or x_2), $T > T_c$ such that $M_{jk}(T)$ scales approximately as $1/T$; in qualitative agreement with the MD results (Figs. 9a, b and d).

The dashed lines in Fig. 9 show fits to the MD data using a single-mode expression (i.e., the first term in Eq. (3.5)) for M_{i3} ($i = 1, 2, 3$) and a two-mode expression (i.e., the first two terms in Eq. (3.5)) for M_{ij} ($i, j = 1, 2$). The parameters obtained by fitting are listed in Table 2. We find that the mobility components which involve sliding along the tilt axis, i.e., M_{i3} ($i = 1, 2, 3$), are associated with large activation energies (i.e., $Q^{(1)} \sim 2$ eV in Table 2) in comparison with the activation energies of the other mobility components. This implies that the temperature dependence of these components is dominated by the exponential factor in Eq. (3.5) (i.e., Arrhenius) and these are well-fitted by the single-mode expression (see Figs. 9c, e and f). However, for the other mobility components, i.e., M_{ij} ($i, j = 1, 2$), the activation energy of the first mode is negligible (i.e., $Q^{(1)} \sim 0$ eV in Table 2) such that the temperature dependence is dominated by the $1/T$ pre-factor in Eq. (3.5). For these components, a second mode is required to capture the high-temperature behavior. The activation energy for the second mode is, of course, larger than that of the first mode (i.e.,

Table 2: Activation energy $Q^{(m)}$ and pre-exponential $c_{ij}^{(m)} \equiv f_0 L^2 H_i^{(m)} H_j^{(m)} / k_B$ for the m^{th} mode for the mobility component M_{ij} , obtained by fitting Eq. (3.5) to the data in Fig. 9. The fit was performed assuming a single-mode expression for M_{i3} ($i = 1, 2, 3$) and a two-mode expression for M_{ij} ($i, j = 1, 2$). The pre-exponential normalization is $c_0 = 1 \text{ K m s}^{-1} \text{ MPa}^{-1}$. The symbols “_” in the last two rows indicate that a single-mode model was sufficient (no two-mode fitting was performed).

	M_{11}	M_{12}	M_{13}	M_{22}	M_{23}	M_{33}
$\ln(c_{ij}^{(1)}/c_0)$	7.5	6.2	31	4.7	15	25
$Q^{(1)}$ (eV)	~ 0	~ 0	2.8	~ 0	1.2	2.1
$\ln(c_{ij}^{(2)}/c_0)$	8.8	8.3	–	5.9	–	–
$Q^{(2)}$ (eV)	0.2	0.2	–	0.2	–	–

$Q^{(2)} > Q^{(1)}$ for M_{11} , M_{12} and M_{22} in Table 2).

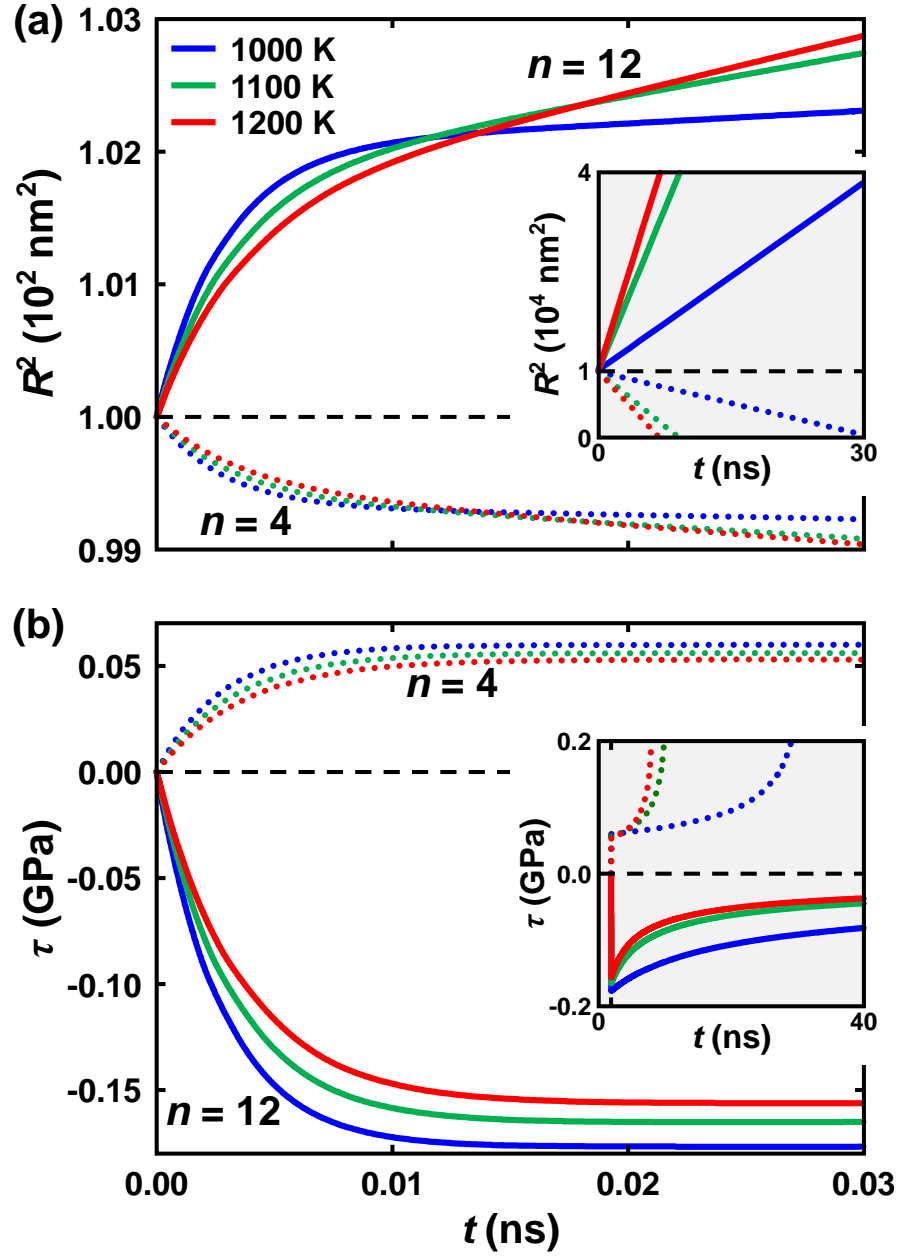


Figure 10: Numerical results for (a) square of the mean grain size R^2 vs. time t and (b) the shear stress τ vs. time t at 1000 K (blue), 1100 K (green) and 1200 K (red). The solid and dotted lines are for the case of $n = 12$ and 4, respectively (n is the number of edges of a grain in a 2D microstructure). The insets show the time evolutions for much longer times.

3.5. Discussion

The classical kinetic equation for describing capillarity-driven GB migration is $v_{\perp} = m\psi = m\gamma\kappa$, where γ is the GB energy and κ is the mean curvature of the GB plane. This description naturally led to a description of the growth of individual n -sided grains in a 2D polycrystal (i.e., the von Neumann-Mullins relation (Von Neumann, 1952; Mullins, 1956)): $\dot{R} = mg\gamma/R$, where R is the grain size, $g = n/6 - 1$ is a factor accounting for grain topology, and we approximated the rate of change of the area of a grain as $R\dot{R}$. Integration leads to one of the classic laws for grain growth: $R^2 - R_0^2 = 2mg\gamma t$, where R_0 is the initial grain size. If we incorporate the tensor character of the mobility, what are the consequences for grain growth?

For the case of the growth/shrinking of a grain in a 2D polycrystal, Eq. (3.1) can be simplified as

$$\begin{pmatrix} \dot{R} \\ -\dot{\tau}R/\mu \end{pmatrix} = \begin{pmatrix} M_{11} & M_{12} \\ M_{12} & M_{22} \end{pmatrix} \begin{pmatrix} g\gamma/R \\ \tau \end{pmatrix}. \quad (3.6)$$

$-\dot{\tau}R/\mu$ is the shear across the grain boundary assuming a linear elastic constitutive relation (Thomas et al., 2017). The numerical results are shown in Fig. 10. The numerical values of the terms in the mobility tensor are those extracted from the MD simulations. As expected, 12-sided grains grow while 4-sided grains shrink. At late times R^2 is a linear function of t and grain growth is parabolic. However, at early times R^2 is not a linear function and grain growth is not parabolic (see Fig. 10a). Figure 10b shows that the grain growth is accompanied by the development of internal stress; for growing grains this slowly decays with increasing grain size while for shrinking grains it diverges as the grain size tends to zero. If GB migration and shear are not coupled, i.e., $M_{12} = 0$, then $R^2 - R_0^2 = 2M_{11}g\gamma t$ and, obviously, no stress develops; this is classical grain growth.

Eq. (3.6) shows that as $R \rightarrow \infty$, $R^2 - R_0^2 = 2\tilde{m}g\gamma t$, where the effective mobility $\tilde{m} = |\mathbf{M}|/M_{22} = M_{11} - M_{12}^2/M_{22}$. Since \mathbf{M} is positive definite, \tilde{m} is necessarily positive. Also, since $\tilde{m} < M_{11}$, we see that the development of GB migration induced internal stresses

always inhibit grain growth/shrinkage; the apparent GB mobility measured in polycrystals will be smaller than that measured in bicrystals. We also note that \tilde{m} does not necessarily increase with increasing temperature (so-called “thermal” GB migration in Olmsted et al. (2009); Homer et al. (2014)). While in the large set of GBs examined by MD (Olmsted et al., 2009; Homer et al., 2014), thermal GB behavior was more common than anti-thermal behavior, we note that both possibilities exist here depending on the relative magnitudes of dM_{11}/dT and $d(M_{12}^2/M_{22})/dT$. While the relationship of \tilde{m} vs. T tends to be increasingly thermal with increasing T (shear coupling is less effective at higher T), there have been experimental observations of anti-thermal behavior in grain growth at low temperature (Rheinheimer and Hoffmann, 2015).

While this analysis focused on 2D grain growth (the topological nature of the von Neumann-Mullins result makes this case simple), extensions to higher dimension are straightforward (MacPherson and Srolovitz, 2007) (see Appendix).

3.6. Conclusion

Since GB migration and GB sliding are, in general, coupled, we have extended the notion of the GB velocity-driving force relation applied throughout the field to account for both this coupling and the inter-relation between the different types of GB motion (migration and sliding). The natural extension is from a scalar velocity-mobility-driving force relation to one in which the velocity and forces may be thought of as vectors and the mobility as a second rank tensor. The kinetic equation suggests the definition of a GB mobility tensor, \mathbf{M} . The diagonal components of \mathbf{M} correspond to the conventional GB mobility and GB sliding coefficient (or the inverse of a GB viscosity). The off-diagonal components of \mathbf{M} reflect coupling between GB migration and GB sliding. We determined the full GB mobility tensor and its temperature dependence for a $\Sigma 7$ [111] ($12\bar{3}$) symmetric tilt GB in copper via molecular dynamics simulations. Surprisingly, we found that some components of \mathbf{M} increase with temperature while others decrease. We were able to explain this temperature dependence as well as several general properties of the mobility tensor based upon analysis of a disconnection model. These results were then applied to analyze the effect of shear

coupling on grain growth. In particular, we showed that the effective GB migration mobility will be smaller than that expected based upon bicrystal experiments as a result of stress generation during grain growth in polycrystalline systems.

CHAPTER 4 : Temperature Dependence of Grain Boundary Mobility

This chapter was adapted from Chen et al. (2020b), where K. Chen, J. Han, and D.J. Srolovitz designed research, performed research, and wrote the paper; K. Chen performed simulations and analyzed data.

Chapter 3 proposes the concept of GB mobility tensor \mathbf{M} . In this chapter, we focus on $M \equiv M_{11}$, the component of the mobility tensor that couples the normal components of the GB velocity and driving force (i.e., here, M is a scalar). Since the most widely employed approach for controlling the rate (and often the nature) of microstructure evolution is through variation of temperature T (i.e., annealing), this study focuses on the temperature dependence of the GB mobility.

The temperature dependence of grain boundary mobility has been measured for a wide range of materials both experimentally (Aust and Rutter, 1959a,b; Rutter and Aust, 1965; Gottstein and Shvindlerman, 2009) and via atomistic simulations (Homer et al., 2014; Rahman et al., 2014; Janssens et al., 2006; Zhang et al., 2004; Priedeman et al., 2017; Zhang et al., 2005; Olmsted et al., 2009; Zhou and Mohles, 2011; Song and Hoyt, 2012; Upmanyu et al., 1999; Schönfelder et al., 2005). The quoted references focused on the measurement of the mobility of nominally flat GBs in bicrystals of elemental metals rather than GBs in microstructures (i.e., averaging over many GBs or influenced by GB junctions). The temperature-dependence of the GB mobility is commonly fit to an Arrhenius relation $M = M_0 e^{-Q/k_B T}$, where Q is an activation energy, the prefactor M_0 is a constant, and k_B is the Boltzmann constant. This Arrhenius relation provides a good fit to many of the M vs. T experimental data. However, GB mobilities extracted from atomistic simulations in pure systems show a wide variety of T -dependences (Homer et al., 2014; Olmsted et al., 2009; Schönfelder et al., 2005). Homer et al. (Homer et al., 2014) performed a series of MD simulations of GB migration in Ni for a large number of bicrystallographically different GBs. While nearly half of these GBs showed mobilities that they characterized as Arrhenius

over some range of temperature, they also observed several/many cases for which the GB mobility (i) decreased with increasing T (so called anti-thermal behavior), (ii) was nearly T independent, (iii) exhibit maxima and/or minima with respect to T , and (iv) is nearly zero at low T and then increases rapidly over a small T -range. The existence of such diversity in GB mobility $M(T)$ within a single material challenges our current understanding of and ability to predict GB mobility.

Recent studies suggest that GB migration occurs through the motion of line defects (i.e., disconnections), that are constrained to lie within the GB and are characterized by both a Burgers vector \mathbf{b} and a step height h that are determined by the underlying GB bicrystallography (Hirth and Balluffi, 1973; Pond and Bollmann, 1979; King and Smith, 1980; Balluffi et al., 1982; Hirth et al., 2006, 2007; Cahn et al., 2006; Thomas et al., 2017; Han et al., 2018; Hadian et al., 2018; Chen et al., 2019). Both atomistic simulation (Rajabzadeh et al., 2013b; Khater et al., 2012; Combe et al., 2016; Hadian et al., 2018) and electron microscopy (Legros et al., 2008; Momprou et al., 2009; Rajabzadeh et al., 2013a) studies have directly observed GB migration through the formation and migration of disconnections along GBs. The motion of disconnections of different modes, characterized by different (\mathbf{b}_m, h_m) (m is the index for mode) allowed by the bicrystallography, can conspire to affect GB motion. This suggests a possible source for some of the complexity in the observed temperature dependence of GB mobility (Thomas et al., 2017; Han et al., 2018; Chen et al., 2019).

In this paper, we explore the T -dependence of GB mobility based upon kinetic Monte Carlo (kMC) and molecular dynamics (MD) simulations of GB migration. We then propose an analytical model to describe many of the observed forms of the temperature dependences of GB mobility.

4.1. Kinetic Monte Carlo Simulations

4.1.1. Model

Here, we describe the motion of a GB in terms of the formation and migration of disconnections, as illustrated in Fig. 11. This model describes a quasi-2D bicrystal, containing a quasi-1D tilt GB. The tilt axis of the GB is along the \mathbf{e}_1 -axis and the GB normal is \mathbf{e}_3 (see Fig. 11a). By “quasi”, we imply that the bicrystal structure is uniform along the \mathbf{e}_1 -axis (i.e., the model is thin in the \mathbf{e}_1 -direction). Periodic boundary conditions are applied in both the \mathbf{e}_1 - and the \mathbf{e}_2 -axes. The GB is discretized into N lattice sites along the \mathbf{e}_2 -axis. The state of the i^{th} lattice site ($1 \leq i \leq N$) on the GB is denoted by (u_i, z_i) , where u_i is the relative (tangential) displacement of the upper grain with respect to the lower one (i.e., eigen-shear) in the \mathbf{e}_2 direction and z_i is the position of the GB plane in the \mathbf{e}_3 -direction at GB-site i . Formation of a \pm disconnection pair of mode m , (b_m, h_m) and $(-b_m, -h_m)$, at site i corresponds to the following change: $(u_i, z_i) \rightarrow (u_i + b_m, z_i + h_m)$, as illustrated in Fig. 11b. The evolution of the state of the GB is described by $\{(u_i(t), z_i(t))\}$ for all GB sites i . Disconnection motion is represented as transitions in the GB states on a series of sites. For example, referring to Fig. 11b, if the right disconnection “ \top ” glides to the right by one lattice site (a distance δ), the state of site $(i + 1)$ changes from (u_{i+1}, z_{i+1}) to $(u_{i+1} + b_m, z_{i+1} + h_m)$.

Under a driving force, the GB lattice site states shown in Fig. 11 will evolve. In the kMC simulations described here, we focus on a driving force associated with a difference (or jump) in the chemical potential across the GB, denoted by ψ . ψ can represent driving forces of different physical origins. For example, ψ can represent a capillary force (curvature), the difference in strain energy between two differently oriented grains in a bicrystal with anisotropic elastic constants subject to a non-shear stress (Washburn and Parker, 1952) or the effects of an applied magnetic field in a material with orientation-dependent magnetic susceptibility (Günster et al., 2013). In atomistic simulations, ψ is often modeled using the synthetic driving force method (Janssens et al., 2006). GB migration can be driven by

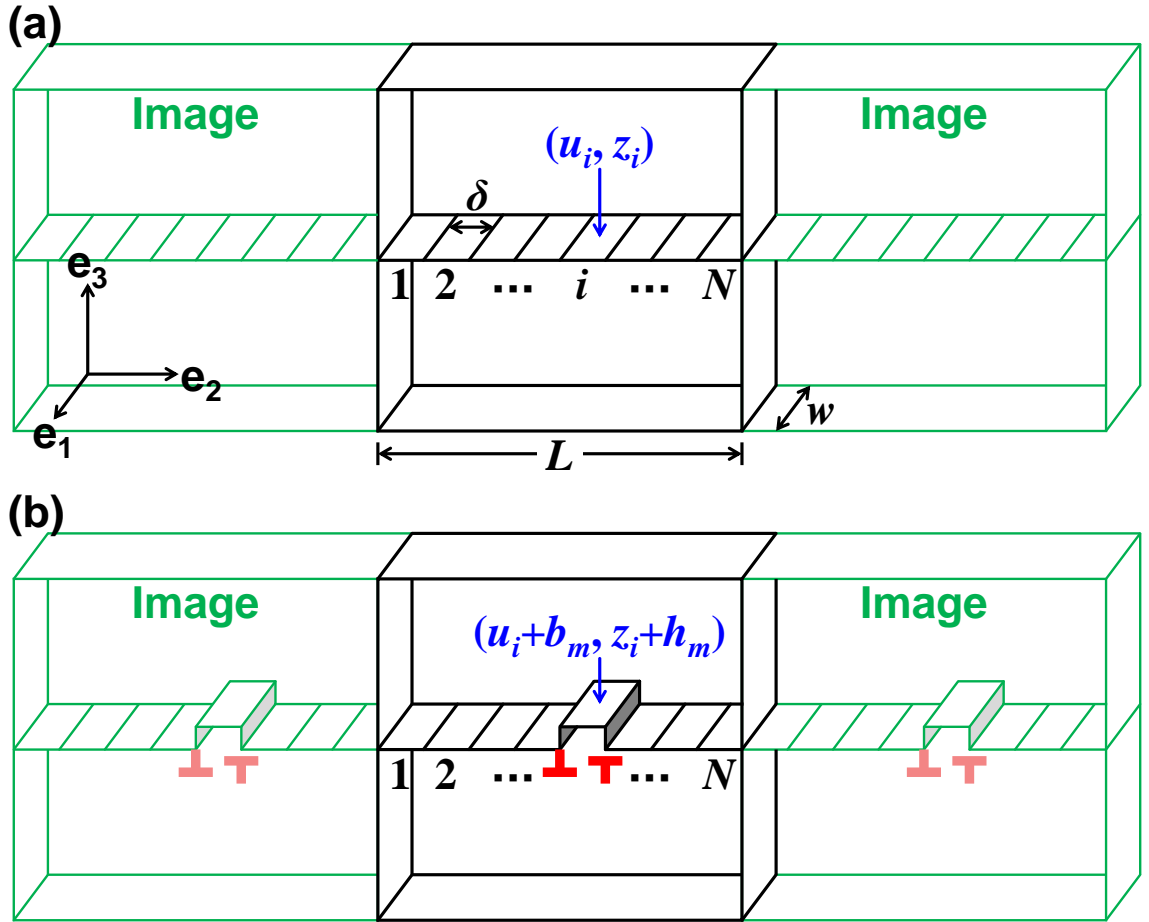


Figure 11: (a) Quasi-1D lattice model description of a tilt GB. The state of lattice site i is (u_i, z_i) . (b) The GB state after nucleation of a pair of disconnections of mode m (i.e., (b_m, h_m) and $(-b_m, -h_m)$) at site i .

other types of driving forces, such as a shear stress parallel to the GB plane τ . However, in most experiments (Hu and Rath, 1972; Grünwald and Haessner, 1970; Molodov et al., 1995; Viswanathan and Bauer, 1973; Lejček et al., 1994; Furtkamp et al., 1998; Molodov et al., 1998) and atomistic simulations (Olmsted et al., 2009; Homer et al., 2014), GB mobility is measured based upon chemical potential jump driving forces ψ (e.g., curvature-driven GB motion) (Gottstein and Shvindlerman, 2009).

4.1.2. Algorithm

In this section, we describe the kinetic Monte Carlo (kMC) algorithm we employ to simulate GB migration under a chemical potential jump driving force ψ .

The first step is to determine the Burgers vector and step height for each disconnection mode m (b_m, h_m), the energy landscape and the work done by the external driving force $W_m^E \equiv -\psi h_m \delta$, where δ is the periodicity of the local energy landscape along the GB which we associate with width of the GB site. We initialize the model by assuming that the GB is disconnection-free along $u_i = 0, z_i = 0$ (for $i = 1, \dots, N$) at time $t = 0$. Then, the kMC simulation proceeds as follows.

- (i) List the energy barriers for all possible transition events. The energy change associated with the formation of a disconnection pair of mode m at site i ΔE^S is (see Fig. 12):

$$\begin{aligned} \Delta E_{im} &= \frac{1}{2} \Delta E_{im}^S + E_m^* \\ &= \frac{1}{2} (\Delta E_{im}^c + W_{im}^I + W_m^E) + E_m^*, \end{aligned} \quad (4.1)$$

where ΔE_{im}^S is the total energy change associated with forming the disconnection dipole, E_m^* is the disconnection glide barrier and W_m^E is the work done by the driving force (chemical potential jump). ΔE^c is the formation energy of two disconnection

cores:

$$\begin{aligned}
\Delta E_{im}^c = & \gamma \left[|z_i^+ - z_{i-1}| + |z_{i+1} - z_i^+| \right. \\
& \left. - |z_i - z_{i-1}| - |z_{i+1} - z_i| \right] \\
& + \zeta K \left[(u_i^+ - u_{i-1})^2 + (u_{i+1} - u_i^+)^2 \right. \\
& \left. - (u_i - u_{i-1})^2 - (u_{i+1} - u_i)^2 \right], \tag{4.2}
\end{aligned}$$

where the first term is associated with the increased GB area (steps) and the second is an estimate of the core energy associated with the disconnection Burgers vectors (Thomas et al., 2017; Han et al., 2018; Chen et al., 2019, 2020a) δ . Here, γ is the GB energy associated with the step face, $K = \mu/4\pi(1 - \nu)$ (μ is the shear modulus and ν is the Poisson's ratio), and ζ is a constant. W^I is the contribution to the work done in forming a disconnection pair associated with the internal stress field τ_i at site i from all other disconnections in the systems (this is the Peach-Koehler (PK) force):

$$W_{im}^I = -\tau_i b_m \delta + \frac{2\pi K b_m^2}{N} \cot\left(\frac{\pi}{2N}\right). \tag{4.3}$$

The second term in this expression is associated with the expansion of the disconnection dipole from size 0 to $\delta = L/N$ (i.e., the elastic interaction between the two disconnections in the dipole. Equation (4.1) can best be understood by reference to Fig. 12.

- (ii) Compile a list of the rates of all possible transitions. The transition rate associated with the formation of a mode m disconnection dipole at site i is

$$\lambda_{im} = \omega \exp\left(-\frac{\Delta E_{im} w}{k_B T}\right), \tag{4.4}$$

where ω is an attempt frequency and w is the thickness of the bicrystal in direction \mathbf{e}_1 . Note, disconnection migration is simply the formation of a disconnection dipole

adjacent to an existing disconnection. The “activity” of the system is the rate at which any transition occurs, $\Lambda = \sum_m \sum_i \lambda_{im}$.

- (iii) Randomly choose an event in accordance with the probability $p_{im} = \lambda_{im}/\Lambda$. The detailed procedure is as follows. List all events in an array and index each event by j (i.e., a combination (i, m)): $\{p_1, \dots, p_j, \dots\}$. Generate a random number $\chi \in (0, 1]$. If j' is the minimum index such that $\chi \leq \sum_{j=1}^{j'} p_j$, then execute event j' (corresponding to (i', m')).
- (iv) Advance the clock $t := t + \Delta t$, where $\Delta t = \Lambda^{-1} \ln(\eta^{-1})$ and $\eta \in (0, 1]$ is a random number.
- (v) Update the state of site i' as $u_{i'} := u_{i'} + b_{m'}$, $z_{i'} := z_{i'} + h_{m'}$ and the stress at each site in the system ($i = 1, \dots, N$) as

$$\tau_i := \tau_i + \frac{2\pi K b_{m'}}{N\delta} \left\{ \cot \left[\frac{\pi}{N} \left(i' - i - \frac{1}{2} \right) \right] - \cot \left[\frac{\pi}{N} \left(i' - i + \frac{1}{2} \right) \right] \right\}. \quad (4.5)$$

- (vi) Return to Step (i).

(Derivations of Eqs. (4.3) and (4.5) are provided in Appendix)

To perform a simulation, we choose a GB (i.e., including specifying the bicystallography-allowed (b_m, h_m) and their associated energies), a temperature and a driving force ψ . Each kMC simulation is run for 10^6 (variable time) steps and measure a statistically-averaged, steady-state GB migration velocity v . The GB mobility at this temperature is determined from $M = v/\psi$ for ψ sufficiently small that $v \propto \psi$. Such simulations are repeated over a range of temperatures to determine $M(T)$ for the chosen GB.

Two sets of kMC simulations were performed using different disconnection parameter sets.

- (i) The first set of simulations were performed to investigate the contributions of different

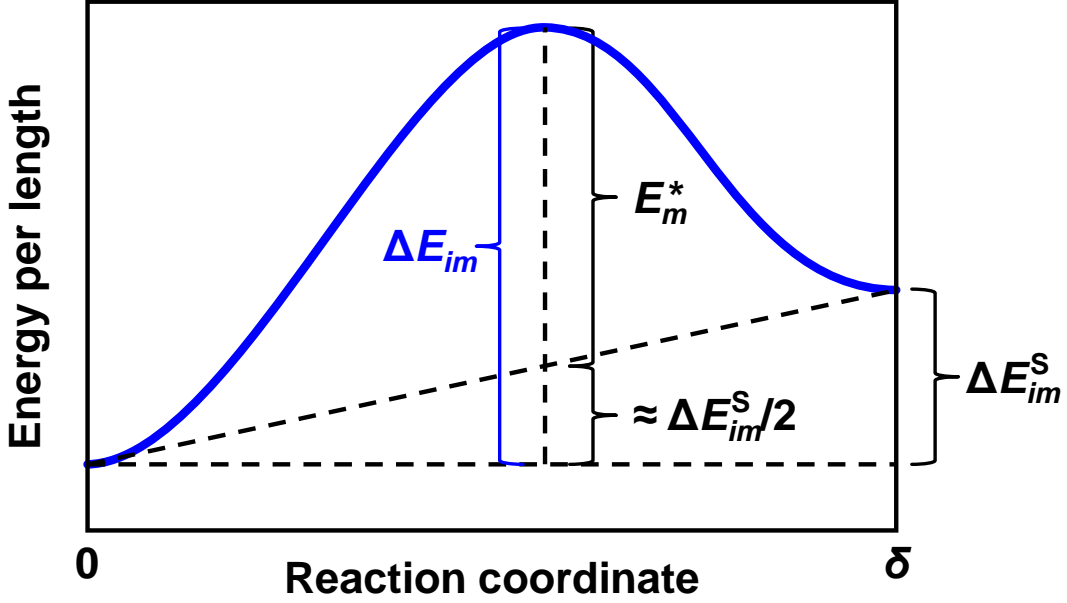


Figure 12: Schematic of the energy barrier associated with a single transition associated with the formation of a pair of disconnections of mode m at site i .

types of disconnections on $M(T)$. For these simulations, we employ reduced (dimensionless) quantities, labeled by “ $\tilde{\sim}$ ”: $\tilde{h} = h/\delta$, $\tilde{b} = b/\delta$, $\tilde{\gamma} = \gamma/(2\pi K\delta)$, $\tilde{\psi} = \psi/(2\pi K)$, $\tilde{\tau} = \tau/(2\pi K)$, $\tilde{T} = k_B T/(2\pi K\delta^2 w)$, $\tilde{E} = E/(2\pi K\delta^2)$, $\tilde{t} = t\omega$, and $\tilde{M} = 2\pi KM/(\delta\omega)$. This representation reduces the number of parameters in the simulations (e.g., by scaling out δ , ω and K). For these simulations, we choose $\tilde{\gamma} = 1$, $\tilde{\psi} = 1$, $\zeta = 2\pi$, and $\tilde{E}_m^* = 0.1\tilde{\gamma}(|\tilde{b}_m| + |\tilde{h}_m|)$.

- (ii) The second set of kMC simulations are performed using parameters determined from atomistic calculations for $\Sigma 17$ [100] (035) and $\Sigma 25$ [100] (034) symmetric tilt GBs in Al (using the embedded-atom-method potential from Mishin et al. (1999)), as described in Section 4.3. The admissible disconnection modes $\{(b_m, h_m)\}$ for these boundaries are as described in Han et al. (2018); Chen et al. (2019).

In all of the simulations reported here, we employed $N = 100$ and the site width δ equal to the coincidence-site-lattice (CSL) cell in the direction parallel to the GB.

4.1.3. Results

Figure 13 shows the temperature dependence of the reduced GB mobility $\tilde{M}(\tilde{T})$ obtained from the first set of kMC simulations. Several cases are investigated in order to understand the effects of the type of the operative disconnection(s) (b_m, h_m) and a single versus multiple operative disconnections.

In the first set of kMC simulations, we focus on a single operative disconnection type that corresponds to a pure-step $(\tilde{b}_1, \tilde{h}_1) = (0, 1)$. The results are shown in Fig. 13a. Starting from low T , the GB mobility increases quickly with temperature and then decays slowly at high T . At low T , GB mobility is well described by an Arrhenius relationship $\ln \tilde{M} \sim -1/\tilde{T}$, while at high T it decays as $\tilde{M} \sim 1/\tilde{T}$; both of these relations are indicated by the two dotted green curves in Fig. 13a).

In the second kMC simulation, we focus on a single operative disconnection that has both finite Burgers vector and step height, $(\tilde{b}_1, \tilde{h}_1) = (1, 1)$. These kMC results are shown in Fig. 13b. The presence of a finite Burgers vector lowers the GB mobility relative to the pure step case. Like in the first kMC simulation, the GB mobility $\tilde{M}(\tilde{T})$ increases at low T and then decays at high T . Two major differences are that the maximum mobility has decreased by more than a factor of two and that instead of rising rapidly from $\tilde{T} = 0$, the GB mobility remains nearly zero until a critical temperature before its initial rise (*cf.* (the $(\tilde{b}_1, \tilde{h}_1) = (0, 1)$ case in Fig. 13a).

Three additional kMC simulations shown are performed, corresponding to two operative disconnection modes. In all cases, the first mode is the pure step disconnection $(\tilde{b}_1, \tilde{h}_1) = (0, 1)$, while the second has both finite step height and Burgers vector; i.e., $(\tilde{b}_2, \tilde{h}_2) = (1, 1)$, $(2, 2)$, and $(3, 3)$ (see Figs. 13c,d,e, respectively). Comparison of these three, 2-mode cases show a much wider range of behavior than in the single mode cases.

While the 2-mode $(\tilde{b}_1, \tilde{h}_1) = (0, 1)$, $(\tilde{b}_2, \tilde{h}_2) = (1, 1)$ case (Fig. 13c) resembles that for the pure step mode case in Fig. 13a, the highest mobility in the 2-mode case exceeds that in the

pure step case by nearly 50% and that of the finite Burgers vector and step height case of Fig. 13b by nearly 300%. Figure 13c compares this 2-mode case ($(\tilde{b}_1, \tilde{h}_1) = (0, 1)$, $(\tilde{b}_2, \tilde{h}_2) = (1, 1)$) with the superposition of the mobilities of the two 1-modes cases ($(\tilde{b}_1, \tilde{h}_1) = (0, 1)$ in Fig. 13a and $(\tilde{b}_2, \tilde{h}_2) = (1, 1)$ in Fig. 13b). The mobility in the 2-mode case is approximated as the sum of those for the two 1-mode cases.

The 2-mode cases with $(\tilde{b}_2, \tilde{h}_2) = (2, 2)$ and $(\tilde{b}_2, \tilde{h}_2) = (3, 3)$ both decay at large temperature, like in the other cases, but also exhibit clear minima at intermediate temperatures and maxima at both high and low temperature. The minimum is deeper for the $(\tilde{b}_2, \tilde{h}_2) = (3, 3)$ mode than for the $(\tilde{b}_2, \tilde{h}_2) = (2, 2)$ mode.

4.2. Statistical Disconnection Model

4.2.1. Model

In this section, we develop an expression for the GB mobility

$$M = \left. \frac{dv}{d\psi} \right|_{\psi=0} \quad (4.6)$$

via a statistical analysis of the formation and migration (glide) of disconnections of one or more modes and compare with the kMC results. The first step is predicting the GB migration velocity v as a function of ψ . For consistency with the kMC simulations, we focus on the quasi-1D GB model of Fig. 11.

We begin by considering GB migration in terms of the formation and glide of a single disconnection mode (b, h) (we omit the subscript “ m ” for a one mode case) on an infinitely long, thermally equilibrated GB under the influence of a driving force ψ . Without a driving force, the GB is characterized by equal densities of positive and negative disconnection pairs. Since the numbers of positive and negative steps are equal, these disconnections do not contribute to net GB migration. When a driving force is applied, extra disconnection pairs of the appropriate sign (positive or negative) form along the GB, with an average spacing between disconnection pairs L (to be determined). For simplicity, focus on a periodic distribution of such pairs (as in Fig. 11b); unlike in the kMC model, here we consider a

continuous (rather than discrete) GB and L is a temperature-dependent correlation (rather than fixed) length. Under the influence of driving force ψ , the two disconnections in each pair glide apart. Once the separation between disconnection pairs reaches L , they annihilate with disconnections from neighboring pairs; at this point, the GB becomes flat again, but has migrated a distance h .

4.2.2. Energetics

The energy change as a function of the separation of the disconnections in a pair by a distance R is illustrated in Fig. 14. The red curve shows that the formation of a disconnection pair (separated by the disconnection core size r_0 in one period) requires energy E^c ; this is the disconnection core energy. Each disconnection interacts elastically with all other disconnections (including the other disconnection of the same pair and their periodic images). To separate a pair of disconnections by distance R against the elastic Peach-Koehler force requires work $W^I(R)$; this is represented by the curved portion of red line in Fig. 14. Expansion of the disconnection dipole against the external driving force ψ also requires work $W^E(R)$; this is denoted by the green line in Fig. 14b. In addition, there is a set of energy barriers E^* resulted from the atomic-scale (Peierls) potential that each disconnection must cross as it migrates. Hence, the total change in energy versus disconnection pair separation R is

$$\begin{aligned}
 E(R) &= E^S(R) + E^G(R) = E^c + W^I(R) + W^E(R) + E^G(R) \\
 &= \begin{cases} (2\gamma|h| + 2\zeta Kb^2) + 2Kb^2 \ln \left| \frac{\sin(\pi R/L)}{\sin(\pi r_0/L)} \right| - \psi h R + E^G(R), & r_0 \leq R \leq L - r_0 \\ 0, & \text{otherwise} \end{cases},
 \end{aligned} \tag{4.7}$$

where E^S is the energy of the stable/metastable states (corresponding to the red curves in Fig. 14), $E^c \equiv 2\gamma|h| + 2\zeta Kb^2$ is an estimate of the disconnection core energy and $E^G(R)$ describes the periodic glide barriers which we approximate as $E^*[1 - \cos(2\pi R/\delta)]/2$. Equation (4.7) describes the blue curve in Fig. 14.

The free energy associated with formation of the disconnection pair should also include the configurational entropy. In our model, L is the average spacing between disconnection pairs; hence, δ/L is the equilibrium concentration of disconnections:

$$\frac{\delta}{L} = \exp\left(-\frac{E^c}{k_B T/w}\right). \quad (4.8)$$

(See Appendix for more details.) The configurational entropy (per length) is then

$$\begin{aligned} S &= \frac{k_B}{\delta w} [L \ln L - \delta \ln \delta - (L - \delta) \ln(L - \delta)] \\ &\approx \frac{k_B}{w} \ln\left(\frac{eL}{\delta}\right) = \frac{k_B}{w} + E^c/T, \end{aligned} \quad (4.9)$$

where the last line applies for $(\delta/L) \rightarrow 0$ and we applied Eq. (4.8). Finally, the free energy (per length) as a function of disconnection separation R may be written as

$$\begin{aligned} F(R) &= E(R) - TS \\ &= W^I(R) + W^E(R) + E^G(R) - k_B T/w, \end{aligned} \quad (4.10)$$

where the individual terms are as per Eq. (4.7). Recall that the quantities F , E , S , W^I , W^E , E^* , E^c and L are dependent on disconnection mode such that in the multi-disconnection mode case, each should have a subscript m .

4.2.3. Kinetics

We estimate the GB velocity as the ratio of the step height to the sum of the disconnection (pair) nucleation time t_m^n and the time required for the disconnections to migrate t_m^g the distance required for annihilation L :

$$v = \sum_m \frac{h_m}{t_m^n + t_m^g}. \quad (4.11)$$

The most important assumption implied by Eq. (4.11) lies in the summation over all modes. We implicitly make the approximation that disconnection interactions only occur between

disconnections of the same mode (of course, this is not true). In order to assess this approximation we compare kMC results in Fig. 13c, where the red curve shows the GB mobility obtained by adding the velocities of two, single mode kMC simulations (i.e., $(\tilde{b}, \tilde{h}) = (0, 1)$ and $(1, 1)$) and the black curve shows the same two modes operating together in one kMC simulation. While the agreement is not perfect, it is very good indicating that this is a reasonable approximation.

We now derive expressions for t_m^n and t_m^g in Eq. (4.11). For each mode (temporarily dropping mode index m), the free energy barrier for disconnection pair nucleation is $\Delta F = F(R^\ddagger)$, where $R^\ddagger = R^\ddagger(\psi)$ is the driving force-dependent critical separation (i.e., where F is a maximum). From Eqs. (4.7) and (4.10),

$$\Delta F = 2Kb^2 \ln \left[\frac{\sin(\pi R^\ddagger/L)}{\sin(\pi r_0/L)} \right] - \psi h R^\ddagger + E^* - k_B T/w. \quad (4.12)$$

Expanding ΔF about $\psi = 0$ (recall that R^\ddagger is a function of ψ) and retaining the first order term, we find that $R^\ddagger = L/2 + \mathcal{O}(\psi)$ and

$$\Delta F = E^e + E^* - k_B T/w - \psi h L/2 + \mathcal{O}(\psi^2), \quad (4.13)$$

where $E^e \equiv W^1(R = L/2) = -2Kb^2 \ln[\sin(\pi\delta/2L)]$ represents the contribution of the long-range elastic interactions between disconnections (obviously, for a pure step mode $b = 0$, $E^e = 0$). The nucleation time is then

$$\begin{aligned} t^n &= \frac{1}{r^+ - r^-} \\ &= \left\{ \omega \exp \left[-\frac{\Delta F(h)}{k_B T/w} \right] - \omega \exp \left[-\frac{\Delta F(-h)}{k_B T/w} \right] \right\}^{-1} \\ &= \frac{1}{2e\omega} \exp \left(\frac{E^e + E^*}{k_B T/w} \right) \operatorname{csch} \left(\frac{\psi h L}{2k_B T/w} \right), \end{aligned} \quad (4.14)$$

where r^+ and r^- represent the rates for GB migration by h and $-h$, respectively, and $e = \exp(1)$ is Euler's number.

The energy barrier for disconnection glide over the atomic-scale barriers (i.e., the amplitude of the blue curve in Fig. 14) is $E^* - \psi h \delta / 2$. The rate of crossing one such barrier is $r^\pm = \omega \exp[-(E^* \mp \psi h \delta / 2)w / k_B T]$. Within a period L , the number of such glide barriers that must be overcome is $L / 2\delta$, such that the time required for disconnections to glide to annihilation is

$$t^g = \frac{L / 2\delta}{r^+ - r^-} = \frac{L}{4\delta\omega} \exp\left(\frac{E^* w}{k_B T}\right) \operatorname{csch}\left(\frac{\psi h \delta w}{2k_B T}\right). \quad (4.15)$$

Again, recall that t^n and t^g in Eqs. (4.14) and (4.15) depend on disconnection mode such that t^n , t^g , E^e , E^* , h , b and L should be assigned a disconnection mode index (subscript) m .

Substituting Eqs. (4.14) and (4.15) into Eq. (4.11), we obtain an expression for the GB velocity v . Then, based on the definition Eq. (4.6), the GB mobility is

$$M = \frac{2\omega\delta w}{k_B T} \sum_m \frac{h_m^2 \exp\left(-\frac{E_m^* + E_m^c}{k_B T / w}\right)}{1 + \frac{2}{e} \exp\left(\frac{E_m^e - 2E_m^c}{k_B T / w}\right)}. \quad (4.16)$$

Equation (4.16) is applied to predict the temperature dependence of the GB mobility for each of the kMC simulation cases in Section 4.1.3. Compare the theoretical prediction (blue dashed curves) and the kMC simulation results (solid black curves) in Fig. 13. Overall, the theoretical predictions from Eq. (4.16) capture the major trends in the kMC simulation data for all cases. These include

- (i) the increase in mobility with increasing temperature at low T (Arrhenius behavior),
- (ii) the decrease in mobility with increasing temperature at high T (anti-thermal behavior),
- (iii) the presence of a single mobility peak for the single disconnection mode cases,
- (iv) the presence of a single or a double peak (and a corresponding minimum) in the

mobility for the multi-mode cases, and

- (v) the trends in the magnitude of the mobility between different disconnection mode cases.

While the statistical disconnection theory reproduces the major trends in the temperature dependence of the mobility, this theory is only semi-quantitative. This may be attributed to several approximations in the theory. These are (1) not including interactions between disconnections of different modes, (2) assuming the same attempt frequency ω in the expressions for both of all modes t_m^n and t_m^g , and (3) the functional form of Eq. (4.11). Writing the denominator in Eq. (4.11) as the sum of t_m^n and t_m^g yields the correct solutions in the $t_m^n \gg t_m^g$ and $t_m^n \ll t_m^g$ limits, but is only approximate between these limits. This causes the deviation of the mobility peak in the pure step case (Fig. 13a), where $t_m^n \sim t_m^g$.

4.2.4. Trends in $M(T)$

We examine several of the main features of the temperature dependence of the mobility based on the statistical disconnection model.

In the high temperature limit, each term in the summation of Eq. (4.16) will have the form $h_m^2 \exp(-|h_m|)$, which converges rapidly to zero with increasing h_m (or m). This suggests that at high temperature the summation can be truncated; yielding a constant. This then implies that $M \sim 1/T$ in the high temperature limit.

In the low temperature limit ($T \rightarrow 0$), each term in the summation in Eq. (4.16) is $(eh_m^2/2) \exp[-(E_m^* + E_m^e - E_m^c)/(k_B T/w)]$ for $E_m^e > 2E_m^c$ and $h_m^2 \exp[-(E_m^* + E_m^c)/(k_B T/w)]$ for $E_m^e < 2E_m^c$. In other words, each term in the summation in Eq. (4.16) is of the form $(A_m h_m^2/k_B T) \exp(-Q_m/k_B T)$, where A_m and Q_m are positive constants (the detailed forms of which depend on the relative magnitudes of E_m^e , E_m^c and E_m^*). This implies that the GB

mobility has the form

$$\begin{aligned}
\ln M &= \ln \sum_m \frac{A_m h_m^2}{k_B T} \exp\left(-\frac{Q_m}{k_B T}\right) \\
&\approx \ln \left[\frac{A_1 h_1^2}{k_B T} \exp\left(-\frac{Q_1}{k_B T}\right) \right] \\
&\approx -\frac{Q_1}{k_B T} [1 + \mathcal{O}(T \ln T)] \quad \text{as } T \rightarrow 0.
\end{aligned} \tag{4.17}$$

If the $m = 1$ disconnection mode corresponds to the minimum Q_m amongst all the modes, we need only consider this mode in the summation (Eq. (4.17), second line). Equation (4.17) implies that, as $T \rightarrow 0$, the GB mobility is Arrhenius (Eq. (4.17), last line).

When $E^{e_m} \ll E^{c_m}$ (e.g., for a pure step),

$$M = \frac{2\omega\delta w}{k_B T} \sum_m h_m^2 \exp\left(-\frac{Q_m}{k_B T}\right), \tag{4.18}$$

over a wide temperature range ($Q_m = (E_m^* + E_m^c)w$). Figure 15 shows the temperature dependence of the GB mobility in this limit in classical Arrhenius coordinates. For a single mode (black dotted curve), the GB mobility increases and then decreases with increasing temperature (the mobility exhibits a maximum with respect to temperature). At low temperature, the mobility is Arrhenius, but decreases with increasing T at high temperature - this is the so-called anti-thermal behavior (Homer et al., 2014). The temperature at which this behavior switches is roughly given by $dM/dT = 0$ or $T^c = Q_1/k_B$ using Eq. (4.18). Similar conclusions apply when $E^{e_m} \gg E^{c_m}$.

We now examine why there is a local minimum in the $M(T)$ kMC data for some multi-disconnection mode simulations (Fig. 13d,e). Consider two disconnection modes, $m = 1$ and 2 in Eq. (4.18) as indicated by the solid red ($h_2/h_1 = 3$) and blue dashed ($h_2/h_1 = 2$) curves in Fig. 15. When $Q_2 \gg Q_1$, the critical temperature (corresponding to $m = 2$) occurs at a much higher temperature than for the $m = 1$ mode. This implies that there may be a local minimum in the M vs. T data, provided that the two peaks are of

sufficient height. That is, a local minimum exists for $Q_2 \gg Q_1$ if and only if $h_2/h_1 > e$ (see Eq. (4.18)). This is in qualitative agreement with the kMC results in Fig. 13, where a local minimum exists when $h_2/h_1 \geq 2$ and gets deeper as h_2/h_1 increases. The critical ratio h_2/h_1 for the kMC simulations is lower than e mainly because interaction between disconnections of different modes is ignored in the analytical theory. As a specific example, consider the $\Sigma 25$ [100] (034) STGB examined in the MD simulations of Homer et al. (2014), where $h_2/h_1 = 25/7 > e$ such that $M(T)$ should exhibit a local minimum (provided it occurs below the melting point); indeed, this is consistent with the MD data where a local minimum is observed for this GB in Ni, but not in Al. We suspect that the GB mobility in Al too would show a local minimum, if it did not melt first (note, the melting point of Ni is nearly twice that of Al).

4.3. Parameters for Specific Grain Boundaries and Comparison with MD

While the kMC simulations described in Section 4.1 employed parameters chosen to investigate the general features of the temperature dependence of GB mobility, the kMC can also be applied to simulate the motion of a specific GB in a real material – provided the appropriate GB parameters are available. Here, we develop a parameters set for the $\Sigma 17$ [100] (035) and $\Sigma 25$ [100] (034) STGBs in EAM Al (Mishin et al., 1999), perform kMC simulations for these two specific GBs, and compare the GB mobility thus obtained with molecular dynamics results. (We focus on Al here since we have an extensive set of GB energy barrier data for Al from another unpublished study.)

The parameters required for the kMC simulations are $K, \gamma, \zeta, \delta, \omega, \{b_m, h_m\}$ and $\{E_m^*\}$. For any coincidence-site-lattice GB of particular bicystallography, $\{b_m, h_m\}$ can be determined based on the GB geometry (Han et al., 2018). The parameters K, γ, ζ and δ can be determined from E_m^S vs. R with $\psi = 0$ (see the red curve in Fig. 14), which we determine via molecular static for each disconnection mode for each GB. For each mode, we constructed a series of configurations where a pair of disconnections were separated by different distance R . Then, we minimized the energy of each of the prepared configurations and obtained a set of metastable states. The results are plotted in Figs. 16a1 ($\Sigma 17$) and 16b1 ($\Sigma 25$); each data

Table 3: Parameters for two symmetric tilt GBs in EAM (Mishin et al., 1999) Al. $a_0 = 0.405$ nm is the lattice constant, a_{dsc} is the size of a DSC lattice cell, m is the index of disconnection mode, b_m , h_m and E_m^* are the corresponding Burgers vector, step height, and glide barrier, A_m and B_m are fitting parameters (see Eq. (4.19)), $K \equiv \mu/[4\pi(1-\nu)]$ (μ and ν are the shear modulus and Poisson's ratio), γ is the step energy, δ_0 is the effective core size (r_0 is the core size), δ is the spacing between lattice point in the quasi-1D lattice model, and ζ scales the contribution of the core energy (Eq. (4.7)). The range of $K = \mu/[4\pi(1-\nu)]$ corresponds to different crystal orientations and the anisotropic elastic constants are from Mishin et al. (1999). The $\Sigma 17$ [100] step energy is estimated from $\sqrt{2}\gamma_s - \gamma_0$ (Han et al., 2018), where $\gamma_s = 0.4861$ J/m² for the (014) and $\gamma_0 = 0.4657$ J/m² for the (035) STGB in EAM Al. The $\Sigma 25$ [100] step energy estimates employ $\gamma_s = 0.4707$ J/m² for the (017) and $\gamma_0 = 0.3872$ J/m² for the (034) STGB. γ_0 and γ_s are from Han et al. (2017).

m	b_m/a_{dsc}	h_m/a_{dsc}	A_m (eV/nm)	B_m (eV/nm)	E_m^* (eV/nm)	K (eV/nm ³)	γ (eV/nm ²)	$\pi\delta_0/L$	$\pi\delta/L$	ζ	r_0/δ
$\Sigma 17$ [100] (035) with $a_{\text{dsc}} = a_0/\sqrt{34}$											
1	0	8.5	1.07570	0	1.24444						
2	1	-2	0.47855	0.18376	0.19753	20.1013	1.0656	0.28513	0.31416	-1.903	0.134
3	1	6.5	1.39769	0.12727	1.11111						
4	2	-4	1.56834	0.79501	0.29876						
Estimates						20.34-24.53	1.3844				
$\Sigma 25$ [100] (034) with $a_{\text{dsc}} = a_0/\sqrt{25}$											
1	0	12.5	3.25669	0	0.99012						
2	1	-3.5	0.79239	0.24639	0.42222						
3	1	9	3.21678	0.2472	1.14568	19.2861	1.6282	0.06038	0.15708	-1.044	0.135
4	2	5.5	4.54659	0.95765	1.17778						
5	3	2	6.89744	2.30333	1.20741						
Estimates						20.34-24.53	1.7383				

point corresponds to a metastable state after energy minimization. Based on the molecular statics data of each mode, we extract the parameters, as described below.

(i) Fit E_m^S vs. R to

$$E_m^S(R) = A_m + B_m \ln \sin[\pi(R/L + c_m)], \quad (4.19)$$

where A_m , B_m and c_m are the fitting parameters. The fitted curves are plotted in Figs. 16a1,b1. Comparing Eqs. (4.19) and (4.7), we see $B_m = 2Kb_m^2$. K is obtained by fitting $\{B_m\}$ and $\{b_m^2\}$ (for all modes).

(ii) Comparing Eqs. (4.19) and (4.7), we see that

$$A_m = 2\gamma|h_m| - B_m \ln \left[e^{-\zeta} \sin(\pi r_0/L) \right]. \quad (4.20)$$

(We assume that r_0 is the same for all modes.) We denote $C_{m1} \equiv 2|h_m|$, $C_{m2} \equiv -B_m$, $X_1 \equiv \gamma$ and $X_2 \equiv \ln [e^{-\zeta} \sin(\pi r_0/L)]$. Then, Eq. (4.20) becomes

$$C_{m1}X_1 + C_{m2}X_2 = A_m \quad \text{or} \quad \mathbf{CX} = \mathbf{A}. \quad (4.21)$$

We obtain X_1 and X_2 by fitting Eq. (4.21) to the $\{C_{m1}, C_{m2}, A_m\} \equiv \{2|h_m|, -B_m, A_m\}$ data. Minimization of $\|\mathbf{CX} - \mathbf{A}\|$ gives $\mathbf{X} = (\mathbf{C}^T \mathbf{C})^{-1}(\mathbf{C}^T \mathbf{A})$. From this, we find the step energy $\gamma = X_1$.

- (iii) Defining $\sin(\pi\delta_0/L) \equiv e^{-\zeta} \sin(\pi r_0/L) = e^{X_2}$ (δ_0 is the effective disconnection core size), we obtain δ_0 from $\pi\delta_0/L = \arcsin e^{X_2}$. However, the kMC simulations require ζ and δ . As discussed above, these parameters are related by $\zeta + 2 = \ln(\zeta/\zeta_0)$; as long as this relationship is satisfied the lattice model and continuum theory will be consistent (see Appendix). In practice, we choose δ as the size of a CSL cell, such that $\zeta = \ln(\delta/\delta_0) - 2$.

We obtained the parameter E_m^* for each mode from atomistic data obtained using the nudged-elastic-band (NEB) method (Jonsson et al., 1998; Henkelman and Jónsson, 2000). To do this, we first chose two neighboring states corresponding to the minimum energy configurations near the top of the profile (see the blue curve in Fig. 14a); these correspond to the initial and final states in the NEB calculations. The NEB method finds the minimum energy path (reaction coordinates) associated with the transition from the initial (reaction coordinate 0) to the final (reaction coordinate 1) states. These data are shown in Figs. 16a2 ($\Sigma 17$) and 16b2 ($\Sigma 25$) for several of the lowest energy disconnection modes. Then, E^* is the energy difference between the maxima and zero for each curve in Fig. 16.

The parameters obtained by fitting the molecular statics and NEB results for the two GBs are summarized in Table 3. The elastic modulus K obtained from fitting is close to the expected value for a perfect crystal. The excess energy associated with the introduction of a step can be estimated as $\gamma = \sqrt{2}\gamma_s - \gamma_0$ (Han et al., 2018), where γ_0 is the energy of

the flat GB and γ_s is the energy of a GB with inclination of 45° . The value of γ obtained by fitting is consistent with this estimated value. Hence, the fitting based on Eq. (4.19) is reasonable. While $\zeta < 0$ in Table 3 seems counter-intuitive, we recall that ζ is the scaling factor for the core energy only if the chosen core size $\delta/2$ is the real disconnection core size. Since we fix δ as the size of a CSL cell (probably too large), this core energy has no physical meaning. Rather, we choose the core energy parameter and core size self-consistently, as in classical dislocation theory.

With these atomistically-determined parameters (summarized in Table 3), we performed kMC simulations for the $\Sigma 17$ [100] (035) and $\Sigma 25$ [100] (034) STGBs in EAM Al and determined the GB mobility vs. temperature (see the black solid circles in Fig. 17). To test our kMC approach, we also determine the GB mobility as a function of temperature from MD simulations of GB migration (synthetic driving force) using the Large-scale Atomic/Molecular Massively Parallel Simulator (LAMMPS) (Plimpton, 1995) and the same interatomic potentials (as used to determine the kMC parameters). Note that since the kMC model (and theory) are quasi-1D, we performed the bicrystal MD simulations using a simulation cell that is very small in the direction parallel to the tilt axis ($w \sim 1.2$ nm). The other two cell dimensions are ~ 20 nm (parallel to the tilt axis) and ~ 100 nm (orthogonal to the GB plane). All simulations (see Chen et al. (2019) for more details) were run for 3.5 ns and $\psi = 10$ MPa at fixed number of atoms and temperature. The GB position is defined as the x_3 position where the layer-averaged centro-symmetry parameter (Stukowski, 2010) is maximum (Kelchner et al., 1998). The GB migration velocity is the normal velocity of the mean GB plane. The MD results are shown as the hollow blue squares in Fig. 17.

Figure 17 shows that our MD and kMC simulation results are in relatively good agreement with each other (note, the attempt frequency ω in the kMC was not determined from our atomistic simulations – but chosen to yield the best fit to the data). The deviation of the MD data from the kMC and theory in Fig. 17a at 600K is not systematic; the actual deviation may be larger than the error bars which were calculated from two sets of data

points. Figure 17 also shows (red dashed curve) $M(T)$ based upon the disconnection theory (Eq. (4.16) with the same parameters as for the kMC). The statistical disconnection model reproduces both the kMC and MD results. We note that while the MD simulations involve the fewest assumptions in the prediction of the GB mobility and its temperature dependence, it is also the most computationally costly and impractical at low temperature when the GB mobility is not fast. On the other hand, accurate kMC and theoretical predictions of $M(T)$ require determination of the fundamental parameters (such as the energy landscape for the motion of disconnections) - these too can require substantial computational resources (albeit much less than the MD simulations for systematic investigations). (Although the example presented in Figure 17 does not show anti-thermal behavior because of the low melting point of Al, performing additional MD simulations and NEB calculations for Ni or other higher melting point materials should show anti-thermal behavior, based on our kMC results.) The greatest advantage of both the kMC and statistical disconnection theory lies in their utility for systematic investigation of GB migration physics.

4.4. Discussion and Conclusions

The aim of this paper is to provide a mechanistic understanding of the diverse forms of the temperature dependence of the grain-boundary (GB) mobility that were previously reported based upon MD simulations and experiments. Several forms of this temperature dependence have been particularly perplexing, in light of the established theories of how GBs migrate (particularly, “anti-thermal” behavior where the GB mobility decreases with increasing temperature).

This paper provides two approaches for understanding $M(T)$ based upon a disconnection-based mechanism for GB migration: a kinetic Monte Carlo implementation and a statistical disconnection theory. The main idea employed here is that GB migration occurs via the formation and glide of disconnections along the GB; while disconnection dynamics depends on both the disconnection dislocation vector and step character (b, h) , GB migration itself takes place through the motion of the step-component of the disconnection motion. We investigate how different disconnection modes give rise to different GB mobilities and how

the simultaneous migration of different disconnection modes explains some of the richness of the temperature dependence of the GB mobility.

One of the main results of the present work is that the temperature dependence of the GB mobility is related to the fundamentally different disconnection dynamics at low and high temperature. In general, GB migration controlled by a single disconnection mode will lead to an Arrhenius T -dependent mobility at low temperature and a mobility at high T that is inversely proportional to temperature. Depending on the disconnection migration energy landscape, the high temperature regime may not be observed (i.e., if the transition temperature is higher than the melting temperature). The transition between the low and high temperature regimes occurs at different temperatures in different GBs within one material and in different materials for the same GB bicrystallography. The transition or critical temperature can be estimated as Q_1/k_B , where Q_1 is the activation energy for the most easily activated disconnection mode. It is the high temperature behavior, where the GB mobility scales inversely with temperature that is responsible for the reported “anti-thermal” behavior. Both the kMC and theory capture this behavior.

GB migration may also be affected by the activation of multiple disconnection modes; this depends on the relative formation and migration energy of the lowest energy disconnection modes. Activation of two disconnections, can give rise to GB mobilities versus temperature that exhibit two maxima and a local minimum (as seen in the kMC, theory and experiments).

While our main focus has been to understand the mechanistic origin of the factors that affect the temperature of the GB mobility, we also predict $M(T)$ for two specific grain boundaries in aluminum. To do this, we performed a series of static relaxation calculations for these two GBs as well as nudged elastic band calculations to determine the energy landscape associated with disconnection motion in a material described using an EAM interatomic potential. These calculations provided the parameterization for both the kMC and statistical disconnection dynamics theory. We then compared the kMC and theory with

a series of molecular dynamics simulations of the migration of these GBs. The MD, kMC and theory are all in good agreement. This implies that both the kMC and theory can be used to qualitatively predict GB migration behavior. While such parameterization of the kMC and theory via atomistic calculations is time consuming, the computational burden is much lower than the full MD simulations when the goal is systematic prediction (e.g., T -dependence, bicystallography-dependence, ...).

Although we have discussed the existence of different temperature regimes for the GB mobility and different forms of $M(T)$ as more disconnection modes are activated, we note that there are additional physical phenomena that may have a profound effect on the GB mobility. Perhaps, the most important of these, not included here, are GB structural phase transitions (also known as complexion transitions (Cantwell et al., 2014)). While GB structural phase transitions relate to the underlying structure of (even) flat GBs without disconnections, the varied temperature dependence of the GB mobility discussed here is the result of GB dynamics related to disconnection motion. Disconnection dynamics can also give rise to finite temperature phase transitions as well, but such transitions do not (necessarily) change the structure of the underlying GB itself.

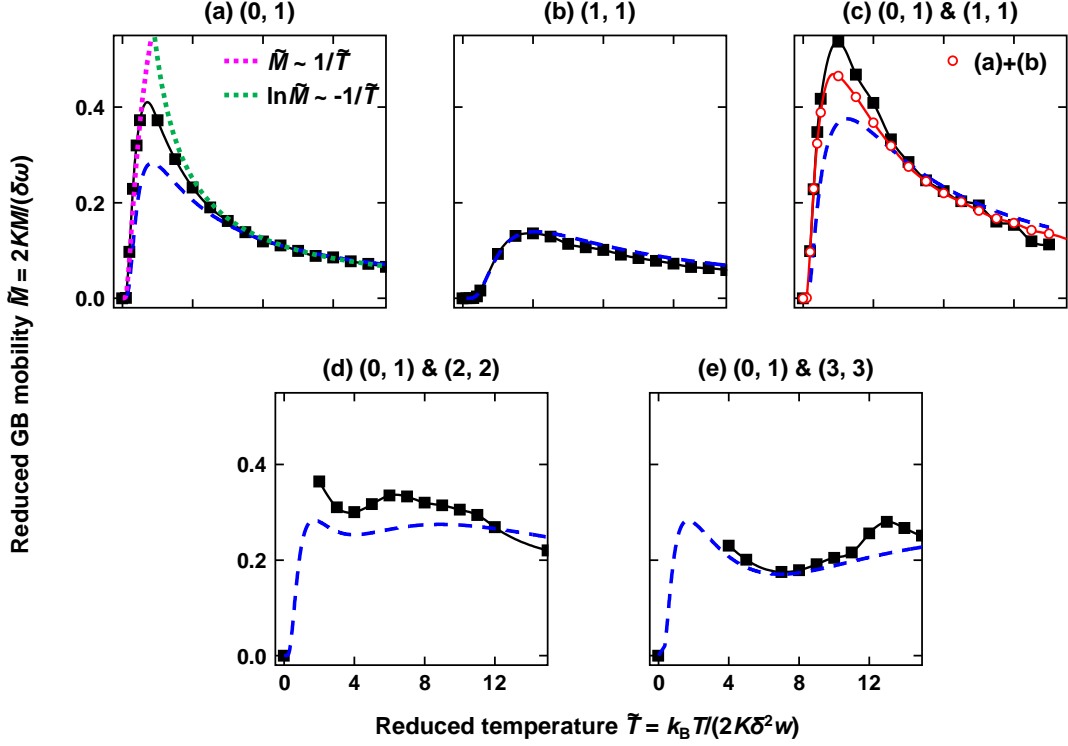


Figure 13: kMC simulation results for the (reduced) temperature dependence of the (reduced) GB mobility. The label above each figure indicates the operative disconnection modes: $(\tilde{b}_1, \tilde{h}_1)$ and, if there is another mode, $(\tilde{b}_2, \tilde{h}_2)$ (recall that $\tilde{h} = h/\delta$ and $\tilde{b} = b/\delta$). The kMC simulation correspond to: (a) a single pure-step disconnection mode – $(\tilde{b}_1, \tilde{h}_1) = (0, 1)$; (b) a single mode – $(\tilde{b}_1, \tilde{h}_1) = (1, 1)$; (c) two modes – $(\tilde{b}_1, \tilde{h}_1) = (0, 1)$ and $(\tilde{b}_2, \tilde{h}_2) = (1, 1)$; (d) two modes – $(\tilde{b}_1, \tilde{h}_1) = (0, 1)$ and $(\tilde{b}_2, \tilde{h}_2) = (2, 2)$; and (e) two modes – $(\tilde{b}_1, \tilde{h}_1) = (0, 1)$ and $(\tilde{b}_2, \tilde{h}_2) = (3, 3)$. In each figure, the kMC results are represented by solid black squares; the solid black lines connecting the kMC data points are drawn as guides to the eye. The blue dashed lines are obtained from the analytical model, i.e., Eq. (4.16). (c) also shows a comparison between the two-mode model (solid black squares) and the sum of the reduced mobilities for the two 1-mode simulations corresponding to the same two modes, individually, as shown in (a) and (b) (hollow red circles). This comparison demonstrates that the mobility in the 2-mode case can be approximated as the sum of those for the two 1-mode cases. The green dotted line in (a) indicates the relationships $\ln \tilde{M} = -1/\tilde{T}$ and the red dotted line indicates $\tilde{M} = 1/\tilde{T}$.

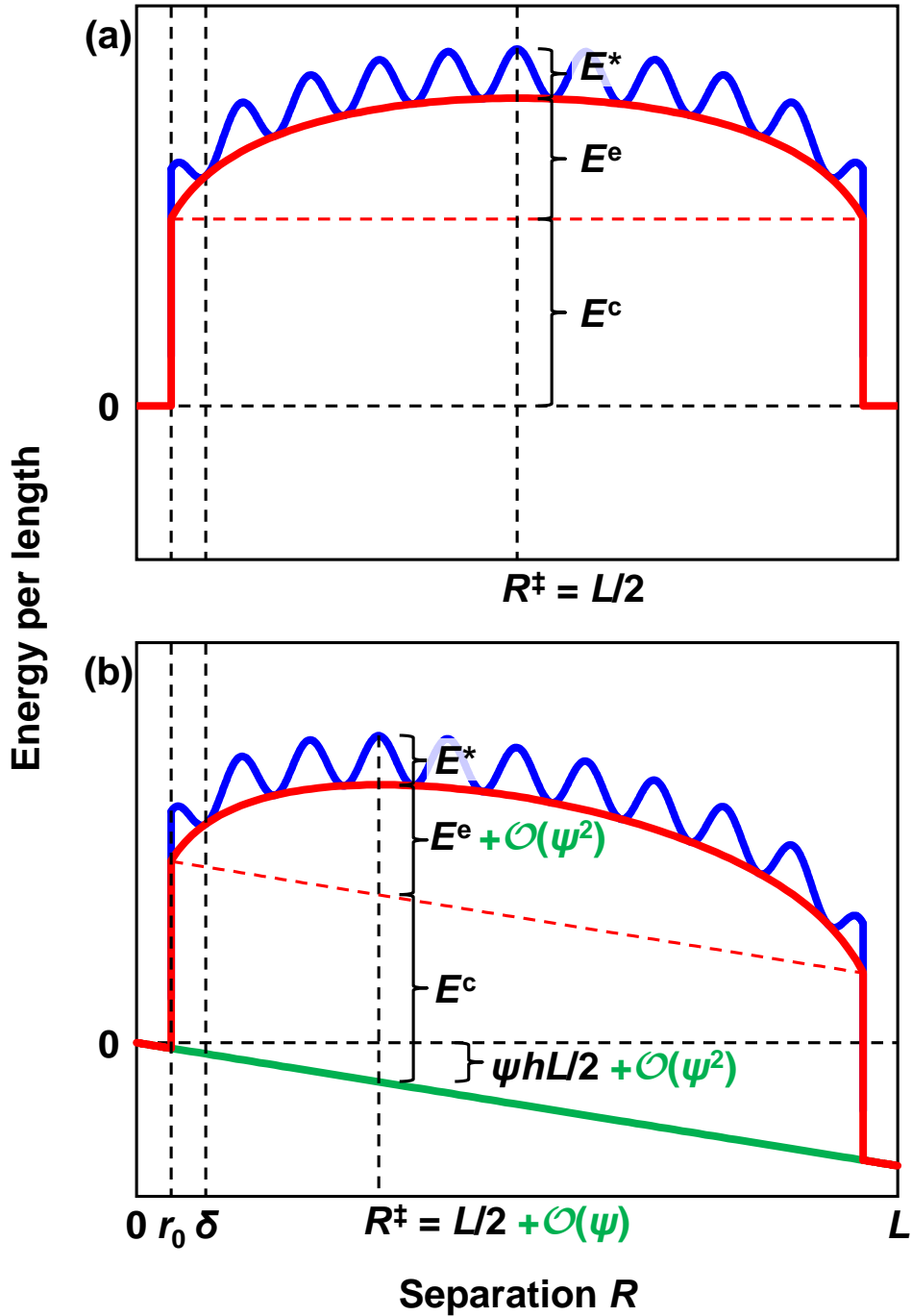


Figure 14: Schematics of the energy vs. separation of a disconnection pair for the cases of (a) $\psi = 0$ and (b) $\psi \neq 0$. The red curves represent $E^S(R) = E^c + W^I(R) + W^E(R)$, the blue curves represent $E(R) = E^S(R) + E^G(R)$, and the green solid line represents $W^E(R) = -\psi h R$. R^\ddagger is the “critical” separation corresponding to the total energy barrier. In (b), the order of the approximation to each part of the energy associated with the external driving force is of order $\mathcal{O}(\psi^2)$.

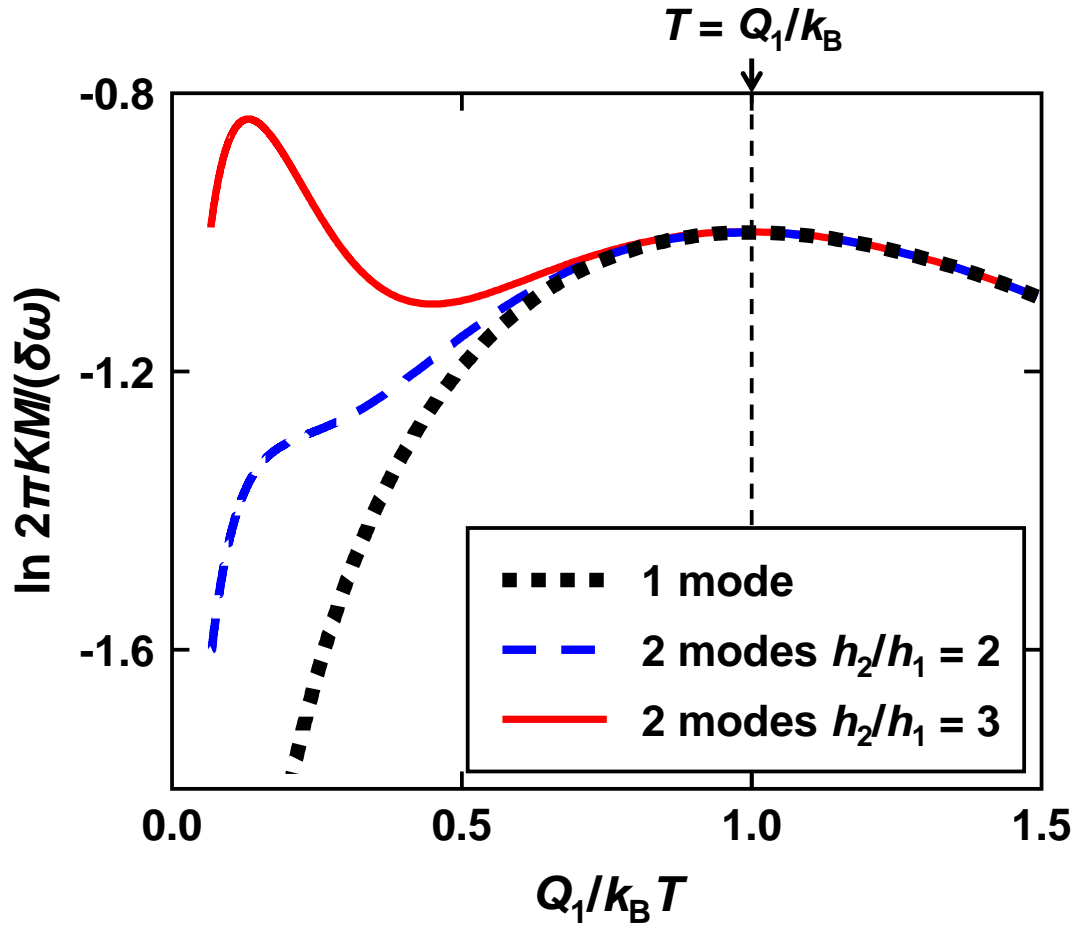


Figure 15: Temperature dependence of GB mobility described by Eq. (4.18) for a single mode (black dotted curve), two modes with $h_2/h_1 = 2 < e$ (blue dashed curve), and two modes with $h_2/h_1 = 3 > e$ (red solid curve) cases. In the two-mode simulations $Q_2 = 10Q_1$.

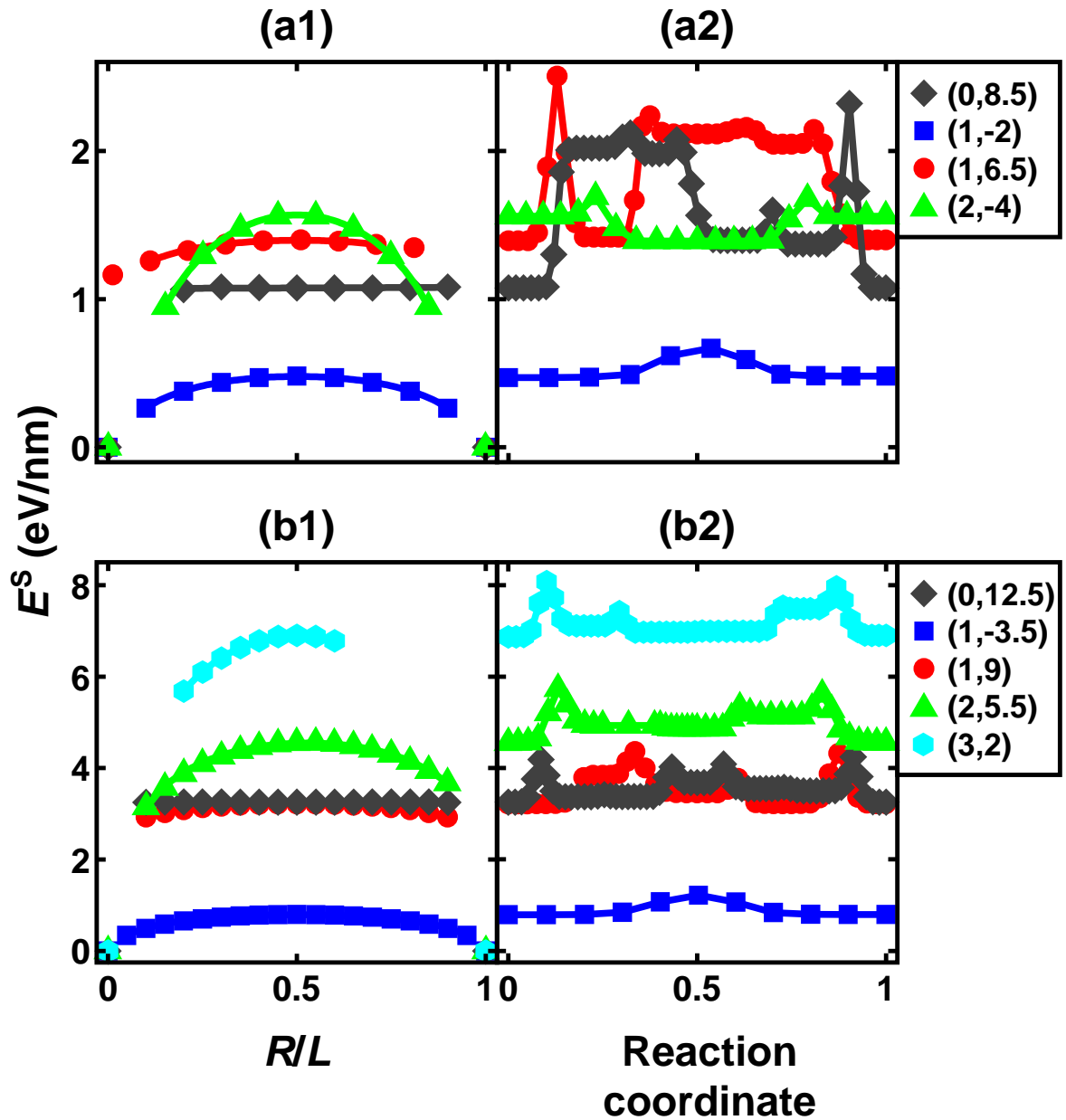


Figure 16: (a1) and (b1) are the energy E^S vs. separation R of a pair of disconnections, scaled by the supercell period L for the $\Sigma 17$ [100] (035) and $\Sigma 25$ [100] (034) STGBs in EAM Al, respectively. The data point colors indicate disconnection modes ($b_m/a_{\text{dsc}}, h_m/a_{\text{dsc}}$), as indicated in the legend. (a2) and (b2) are the energy landscape between two neighboring metastable configurations with the highest energy (at the maxima of each curve in (a1) and (b1)) obtained from the NEB calculations. E^* is the energy difference between the maximum and zero.

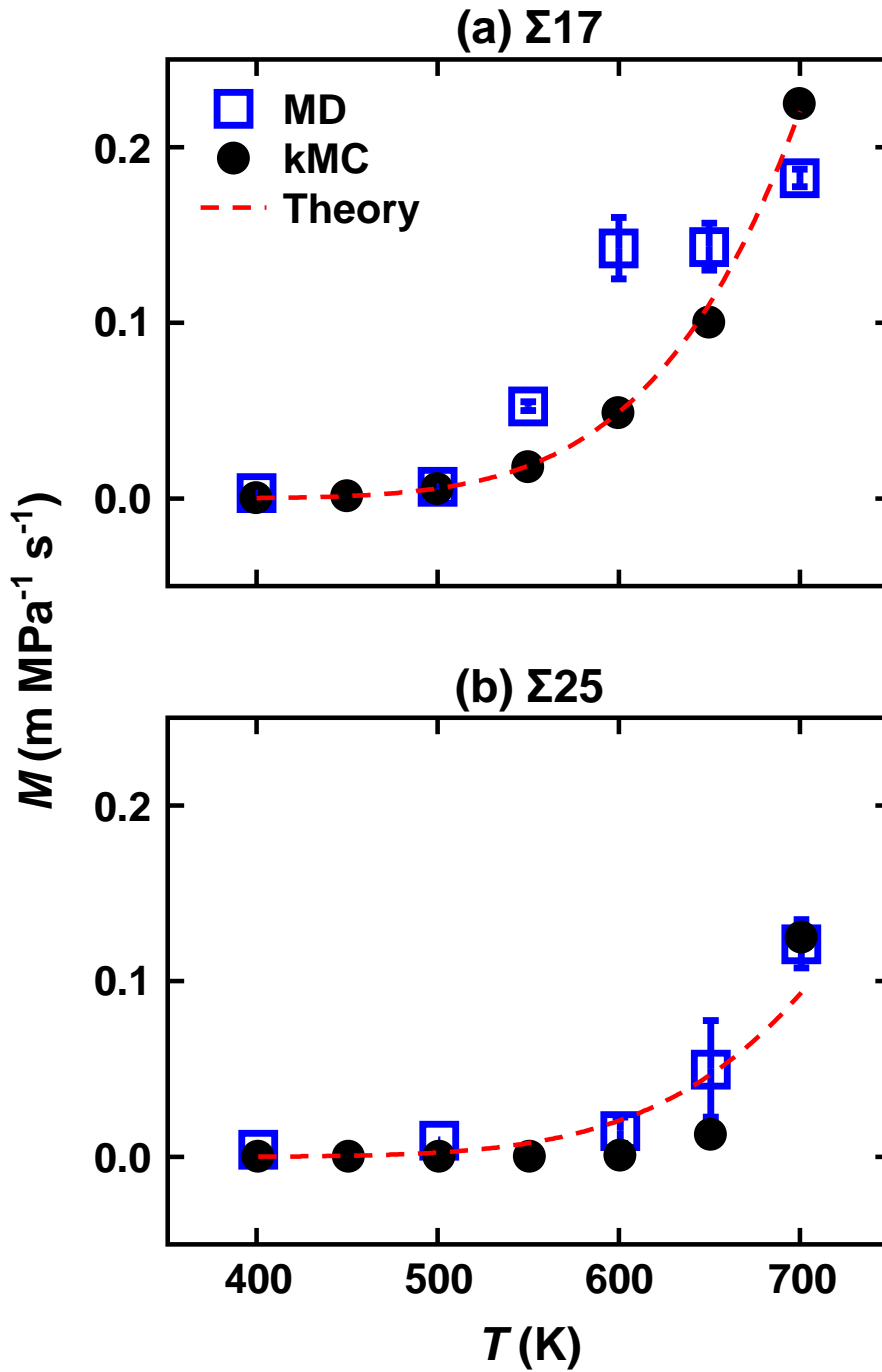


Figure 17: Temperature dependence of GB mobility obtained by MD simulations (blue hollow squares), kMC simulations (black solid circles) and disconnection theory (red dashed lines) for (a) $\Sigma 17$ [100] (035) and (b) $\Sigma 25$ [100] (034) STGBs in EAM Al. The error bars in the MD data represent the mobilities obtained in two MD simulations and the hollow, blue squares represent their mean.

CHAPTER 5 : Grain Boundary Topological Phase Transitions

This chapter was adapted from Chen et al. (2020c), where K. Chen, J. Han, and D.J. Srolovitz designed research, performed research, and wrote the paper; K. Chen performed simulations and analyzed data.

Chapter 4 discusses GB mobility as a continuous function of temperature, but GB mobility, like most material properties, may change abruptly at temperatures corresponding to phase transitions. Such GB phase transitions may explain the existence of critical temperatures at which abrupt changes occur in the nature of several physical phenomena, including grain growth stagnation (Holm and Foiles, 2010) and superplasticity (Edington et al., 1976).

There are several types of GB phase transitions discussed in the literature. These include thermodynamic phase transitions such as complexion/GB structural transitions or faceting/defaceting transitions (which are first-order) (Cantwell et al., 2014; Frolov et al., 2013; Meiners et al., 2020), roughening transitions (divergence in the height-height correlation function) which may be continuous (Rottman, 1986), and improper transitions where the GB transforms from solid-like to glass-like (Zhang et al., 2009). In this paper, we discuss a new class of fundamentally different GB phase transitions. We identify a GB topological phase transition of a type of the class originally discussed by Kosterlitz and Thouless (Kosterlitz and Thouless, 1973). Such topological transitions may be thought of as defect binding/unbinding transitions. The most important type of defects for GB dynamics are disconnections (Han et al., 2018). Disconnections are line defects, constrained to lie within the GB and characterized by both Burgers vector \mathbf{b} and step height h . The set of possible disconnection modes $\{\mathbf{b}, h\}$ is set by GB bicystallography. Disconnections (like dislocations) are topological defects, as seen through a Burgers circuit analysis (Han et al., 2018).

Below the topological or Kosterlitz-Thouless (KT) transition temperature T_{KT} , the interaction between disconnections is long-range, decaying as the inverse of their separation. The

formation and migration of disconnections are severely restricted and GB mobility tends to be small (with important exceptions). On the other hand, above T_{KT} , the long-range elastic field of disconnections is effectively screened. Hence, the KT transition may be viewed as a screening (or sliding) transition, where the screening parameter (dialelastic constant) diverges at T_{KT} . The KT transition leads to abrupt changes in the GB migration mobility, roughness, sliding coefficient, etc.

While the KT transition leads to GB roughening, this transition fundamentally differs from the roughening transition widely discussed in the literature (Rottman, 1986). While this classic roughening phase transition is topological, the steps that control it have no long-range elastic interactions and are not topological defects (nonlocal imperfections corresponding to singularities in an order parameter characterizing a broken symmetry (Irvine et al., 2013)). On the other hand, the dislocation nature of disconnections implies that disconnections are fundamentally topological defects. Hence, the KT transition discussed in this paper corresponds to the screening of long-range elastic interactions, while the classical roughening transition arises from topologically stable configurations of steps (without long-range interactions).

We analyze the KT transition first through mean-field theory, then apply renormalization group analysis to accurately predict the main features of this transition by formal extension to the thermodynamic limit (i.e., infinite length scales). The results are confirmed through a series of kinetic Monte Carlo (kMC) simulations. Our analysis shows that the Kosterlitz-Thouless (KT) transition temperature depends on the driving force for GB motion. For example, in curvature-driven grain growth, we find that at a fixed temperature, large grains are more likely to be below T_{KT} (low mobility) and small grains above it (high mobility). This is a possible explanation of why grain growth in pure materials often stagnates at large grain size and superplasticity is generally restricted to small grain sizes and high temperatures. We confirm these results by comparing our renormalization group prediction of the grain size at which grain growth stagnation occurs with simulation data from the

literature (Holm and Foiles, 2010).

5.1. Disconnection Topological Transitions

We describe the migration of GBs in terms of the motion of disconnections. Motion of disconnections leads to both GB migration (step motion) and shear across the GB (dislocation motion). We demonstrate that an abrupt change in GB behavior may result from an abrupt change in how disconnections interact; this is a topological phase transition.

We first consider the case of a dislocation in a two-dimensional (2d) elastic medium (x - y plane) interacting with dislocation dipoles, following the general approach originally described by Kosterlitz and Thouless (Kosterlitz and Thouless, 1973). Here, we assume that the Burgers vectors are parallel to the x -axis: $\mathbf{b} = b\hat{\mathbf{x}}$. The elastic interaction energy of a test dislocation and another dislocation varies as the logarithm of their separation and the interaction force is minus the gradient of this energy with respect to test dislocation displacement (i.e., decaying as the inverse of their separation). When multiple dislocations are present, the total force on the test dislocation is simply the sum of the forces from each of these. The divergence of the force on the test dislocation (of unit \mathbf{b}) at \mathbf{r} , $\mathbf{f}(\mathbf{r})$ is proportional to the Burgers vector distribution around the test dislocation $\rho(\mathbf{r})$: $\nabla \cdot \langle \mathbf{f} \rangle = 4\pi K \rho(\mathbf{r})$, where $\rho(\mathbf{r})$ is the Burgers vector density and the constant $K \equiv \mu/[4\pi(1-\nu)]$ (μ and ν are the elastic shear modulus and Poisson ratio). (Angular brackets $\langle \dots \rangle$ denote the time average of a fluctuating quantity.) Dislocation dipoles in the material polarize (dislocations in the dipole separate) under the action of a (Peach-Koehler) force (Sutton and Balluffi, 1995). The (polarized) dipole moment is $\int \langle \mathbf{p} \rangle d\mathbf{r} = \int \mathbf{r} \rho(\mathbf{r}) d\mathbf{r}$, where \mathbf{p} is the instantaneous dipole moment density. The distribution of polarized dipoles exert a force on the test dislocation: $\langle \mathbf{f}_p \rangle = -4\pi K \langle \mathbf{p} \rangle$. The total force on the test dislocation is the sum of the applied force \mathbf{f} and that associated with the induced dipoles: $\langle \mathbf{f}_t \rangle = \mathbf{f} + \langle \mathbf{f}_p \rangle = \mathbf{f} - 4\pi K \langle \mathbf{p} \rangle$. The dipole moment is induced by the total force, $\langle \mathbf{p} \rangle = \chi \langle \mathbf{f}_t \rangle$ (to leading order in the force), where, in analogy to electrostatics, we define the susceptibility (tensor) as $\chi \equiv (\partial \langle \mathbf{p} \rangle / \partial \langle \mathbf{f}_t \rangle)|_{\langle \mathbf{f}_t \rangle = \mathbf{0}}$.

The total force on the test dislocation can then be expressed as the external force *screened*

by the induced dipoles $\langle \mathbf{f}_t \rangle = \mathbf{f}/\epsilon$, where ϵ is the diaelastic constant (akin to the dielectric constant in electrostatics). The diaelastic constant describes the strength of the screening of the applied force by the induced dislocation dipoles: $\epsilon \mathbf{I} = \mathbf{I} + 4\pi K \chi$ (\mathbf{I} is the identity matrix).

5.1.1. Disconnections on Grain Boundaries

We now apply this approach to disconnections on a nominally flat GB which, in this 2d model, is the line $y = 0$. In this case, the Burgers vector density is $\rho(x, y) = \rho(x)/\delta$, where δ is the disconnection core size. The external applied force on the test dislocation (with unit \mathbf{b}) is equal to the applied (shear) stress τ parallel to \mathbf{b} , $f = \tau$. In this case, $\epsilon = 1 + 4\pi K \chi$, where χ is the the xx component of the susceptibility tensor. The distribution of the dislocation dipole moment associated with all dipoles with separation smaller than r is $\langle p(r, x) \rangle = \int_{\delta}^r \langle br' \rangle n(r', x) dr'$, where $\langle br' \rangle$ is the moment of a dipole of separation r' and $n(r')$ is the number of dipoles with separation in $[r', r' + dr']$ per unit length between x and $x + dx$. Since we assume that the GB is uniform, we can drop the explicit dependence on x and write the susceptibility as $\chi(r) = (\partial \langle p \rangle / \partial f)|_{f=0} = \int_{\delta}^r \alpha(r') n(r') dr'$ ($\alpha(r') \equiv (\partial \langle br' \rangle / \partial \tau)|_{\tau=0}$ is the dipole polarizability). The diaelastic constant, then, becomes

$$\epsilon(r) = 1 + 4\pi K \int_{\delta}^r \alpha(r') n(r') dr'. \quad (5.1)$$

We evaluate the dipole polarizability and dipole number density $n(r)$ by assuming that the dipoles are in thermal equilibrium (Maxwell-Boltzmann distribution) as in the Debye-Hückel approximation for charged fluids. The polarizability is

$$\alpha(r) = \frac{\partial}{\partial \tau} \frac{\sum_{b'=\pm b} b' r e^{-\beta(E_c - \tau b' r)}}{\sum_{b'=\pm b} e^{-\beta(E_c - \tau b' r)}} \Bigg|_{\tau=0} = \beta b^2 r^2, \quad (5.2)$$

where E_c is the disconnection core energy (per unit length), w is the width of the system in the direction parallel to the disconnection line and $\beta \equiv w/k_B T$. The number density of

dipoles of separation $[r, r + dr]$ is

$$n(r) = \delta^{-3} e^{-\beta[2E_c + V(r) - (\psi h + \tau b)r]}, \quad (5.3)$$

where ψ is the chemical potential jump across the GB (Janssens et al., 2006), and the elastic interaction energy (per unit length) of the two disconnections in a dipole (separation r) is

$$V(r) = 2Kb^2 \int_{\delta}^r \frac{dr'}{r' \epsilon(r')}. \quad (5.4)$$

This completes the derivation except for the determination of the dielectric constant $\epsilon(r)$, which can be determined through the self-consistent solution of Eqs. (5.1) - (5.4). It is useful to define the following dimensionless (reduced) quantities: the reduced length $l \equiv \ln(r/\delta)$, the reduced inverse diaelastic constant $g \equiv \beta K b^2 / \epsilon(r)$, and the reduced dipole density $f \equiv \sqrt{r^3 n(r)}$. These substitutions reduce four coupled equations to just two:

$$\left\{ \begin{array}{l} \frac{dg^{-1}}{dl} = 4\pi f^2 \\ \frac{d \ln f}{dl} = \frac{3}{2} - g + \frac{1}{2} \beta (\psi h + \tau b) r \end{array} \right. . \quad (5.5)$$

In the limit that $r \rightarrow \delta$ (i.e., $l = 0$), we find that $g(0) = \beta K b^2$ and $\ln f(0) = \beta[(\psi h + \tau b)\delta - 2E_c]/2$.

5.1.2. Topological Phase Transition

Here, we examine the topological phase transition that occurs for disconnections on a GB that is associated with the screening of the disconnection fields. We do this first via a simple mean-field analysis (designed to provide qualitative, physical understanding) and then via a more rigorous renormalization group approach.

As above, consider a bicrystal in 2d containing a flat 1d GB, as depicted in Fig. 18; the

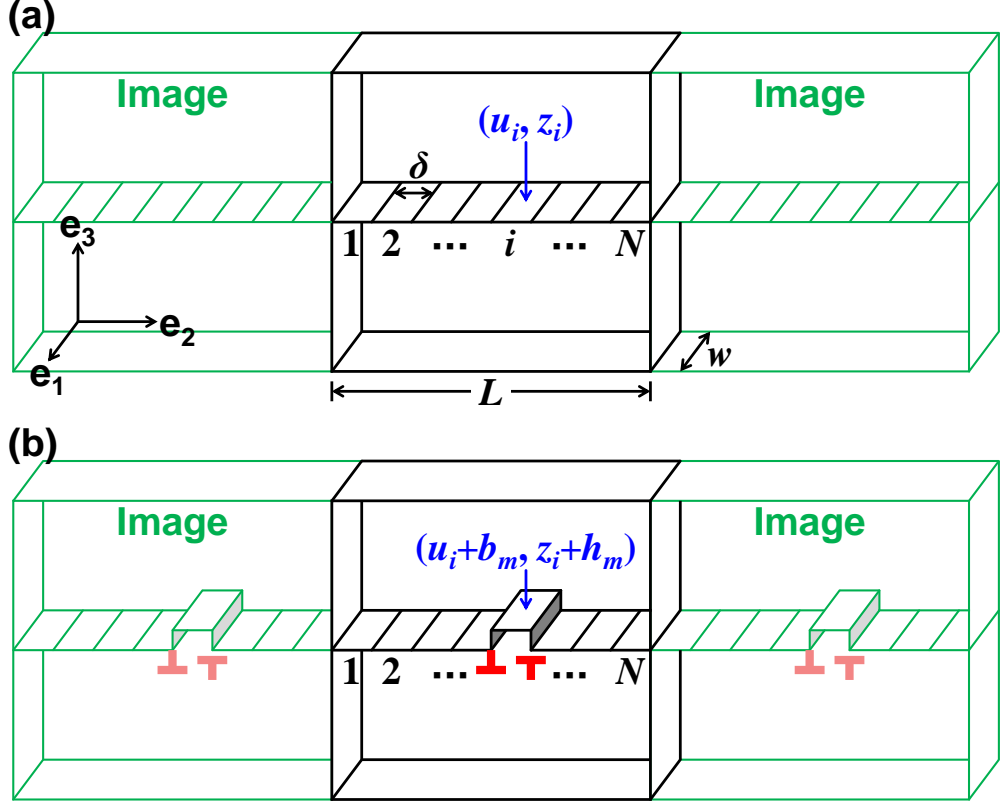


Figure 18: (a) Disconnection dipoles on a 1d GB in 2d. δ , r , L and S denote the disconnection core size, the separation of the disconnections in a disconnection dipole, the average distance between the disconnection dipoles and the system size in the x -direction, respectively. (b) The states of the system at i before and after disconnection dipole nucleation are (u_i, y_i) and $(u_i + b_m, y_i + h_m)$, respectively, for a pair of disconnections of mode m at location i .

tilt axis is in z and the nominal GB normal is in y . We focus on a thermally equilibrated GB; incorporating the formation and annihilation of disconnection dipoles (Fig. 18a). The separation between the two disconnections in a dipole is r , the average distance between disconnection dipoles is L , and the size (length) of the GB is S . Since this model does not describe the GB structure on the atomic-scale, it cannot describe premelting.

For simplicity, we assume that there is only one type of disconnection dipole on the GB, i.e., disconnection mode $(\pm b, \pm h)$. If $b = 0$ (pure-step mode), the free energy change associated with disconnection dipole formation on a flat GB is $F = 2E_c - k_B T \ln(S/\delta) < 0$ as $S \rightarrow \infty$, since the disconnection core energy E_c is independent of GB size S (Thomas et al., 2017;

Han et al., 2018; Chen et al., 2019) and the configurational entropy is proportional to $\ln(S/\delta)$. This suggests that an infinitely large, 1d GB is rough at all $T > 0$ K (i.e., the roughening transition temperature is 0 K). If the GB is of finite size or where the GB is 2d, the roughening temperature is finite (Swendsen, 1977). If $b \neq 0$, however, both entropy and disconnection elastic energy are proportional to $\ln(S/\delta)$; this suggests that there will be a critical temperature above which the entropy term dominates the free energy such that the roughening transition temperature is finite (in all dimensions).

The effect of non-zero b can be understood as follows. At low T , disconnections exist as closely bound dipoles; while at high T the ratio of the separation between disconnections in a dipole to the spacing between dipoles is no longer small, such that the disconnection dipoles mix or, alternatively, the dipoles are unbound. Based on this idea, we can distinguish the low- T from high- T regimes based on whether $\langle r^2/L^2 \rangle \ll 1$ or $\gg 1$, respectively.

The energy of a disconnection dipole has the form $U(r) = 2E_c + V(r)$, where the elastic potential energy is $V(r) = 2Kb^2 \ln(r/\delta)$. We first assume that the equilibrium disconnection dipole density $1/L$ is low; i.e., $E_c \gg k_B T$. The ensemble average (square of the) disconnection separation in dipoles is

$$\langle r^2 \rangle = \frac{\int_{\delta}^{\infty} r^2 e^{-\beta U(r)} dr}{\int_{\delta}^{\infty} e^{-\beta U(r)} dr} = \delta^2 \left(\frac{2\beta K b^2 - 1}{2\beta K b^2 - 3} \right). \quad (5.6)$$

The average number of dipoles in length L can be obtained by the grand-canonical ensemble average:

$$\langle \mathcal{N} \rangle = \frac{\sum_{\mathcal{N}=0}^{\infty} \mathcal{N} \mathcal{Z}^{\mathcal{N}} \mathcal{P}^{\mathcal{N}}}{\sum_{\mathcal{N}=0}^{\infty} \mathcal{Z}^{\mathcal{N}} \mathcal{P}^{\mathcal{N}}} = \mathcal{Z} \mathcal{P} + \mathcal{O}(\mathcal{Z}^2),$$

where $\mathcal{Z} \equiv e^{-2\beta E_c}$ and

$$\mathcal{P} \equiv \frac{1}{\delta^2} \int_0^L dx \int_{\delta}^{\infty} e^{-\beta V(r)} dr = \frac{L/\delta}{2\beta K b^2 - 1}.$$

The average disconnection dipole density $\langle 1/L \rangle$ is obtained by setting $\langle \mathcal{N} \rangle = 1$:

$$\left\langle \frac{1}{L} \right\rangle = \left(\frac{1}{\delta} \right) \frac{e^{-2\beta E_c}}{2\beta K b^2 - 1}. \quad (5.7)$$

From Eqs. (5.6) and (5.7), we find

$$\left\langle \frac{r^2}{L^2} \right\rangle = \frac{e^{-4\beta E_c}}{(2\beta K b^2 - 3)(2\beta K b^2 - 1)}. \quad (5.8)$$

This demonstrates that a critical temperature T_{KT} for which $\langle r^2/L^2 \rangle \rightarrow \infty$:

$$T_{\text{KT}} = 2Kb^2w/3k_B. \quad (5.9)$$

T_{KT} is the Kosterlitz-Thouless transition temperature. For $T < T_{\text{KT}}$, the disconnections are bound pairs; i.e., disconnections exist as dipoles bound together by elastic interactions. However, for $T > T_{\text{KT}}$ the disconnections are unbound; i.e., each disconnection is free to move independently - not bound to any other disconnection.

The GB roughness, as characterized by the standard deviation of the GB profile σ_y scales as $\langle r^2/L^2 \rangle^{\frac{1}{4}}$ and diverges at T_{KT} (in 1D GB T_{KT} is also the roughening transition temperature). This is discussed in more detail in Appendix, demonstrated in our kMC simulations (below), and observed in MD simulations (Olmsted et al., 2007).

The mean-field theory reveals that the long-range elastic interaction between disconnections may result in the disconnection binding-unbinding (or pairing-unpairing) transition. However, mean-field analysis rarely provides accurate predictions of the phenomenon near a phase transition (and thus fails to predict T_{KT} accurately). This problem can often be overcome by application of renormalization group methods. Following the spirit of renormalization group approaches for dislocations (Kosterlitz and Thouless, 1973; Khantha et al., 1994), we look for numerical solutions of Eq. (5.5) to obtain $f(l)$ and $g(l)$.

Any set of physical parameters/driving forces (K, b, h, E_c, T, ψ and τ) correspond to

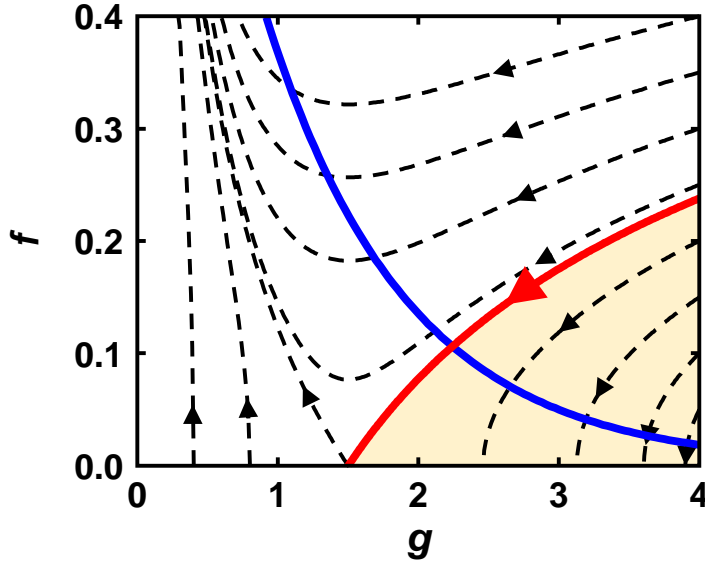


Figure 19: Renormalization flows obtained by numerical solution of Eq. (5.5) with $\psi = \tau = 0$ and different initial conditions $(g(0), f(0))$. The arrows denote directions of increasing length scale l (coarse-graining). The red curve is the critical manifold. The flows in the shaded region converge to $(g > 1.5, f = 0)$ as $l \rightarrow \infty$, while the flows in the unshaded region converge to $(g = 0, f \rightarrow \infty)$. The blue curve corresponds to $(g(0, T), f(0, T))$ where the temperature T increases from bottom right to top left; the material and GB parameters are those used for the one-mode kMC simulation. The Kosterlitz-Thouless transition temperature corresponds to the point where the red and blue curves cross.

different initial conditions $(g(0), f(0))$ in the solution of Eq. (5.5); starting from each particular initial condition there is a flow in $(g(l), f(l))$ as l varies from 0 to ∞ (since l is a length scale, this is coarse-graining that takes the system to the thermodynamic limit). This is depicted in Fig. 19 for different $(g(0), f(0))$. Figure 19 shows that there are two types of fixed points as $l \rightarrow \infty$: (i) a “superfluid phase” $(g = 0, f \rightarrow \infty)$, where screening diminishes dislocation interactions (i.e., $\epsilon \rightarrow \infty$) such that there are many unbound disconnection (i.e., $r^3 n \rightarrow \infty$) and the GB is rough, and (ii) an “insulating phase” $(g > 1.5, f = 0)$, where screening is limited ($\epsilon < 2Kb^2w/3k_B T$ as $r \rightarrow \infty$), few unbound disconnections exist ($r^3 n \rightarrow 0$) and the GB is flat. There is a critical manifold (red curve) in Fig. 19; flows above the critical manifold converge to type (i) fixed points (unbound disconnection/rough GB phase), while flows below this manifold converge to type (ii) fixed points (bound disconnection/flat GB phase).

The KT transition temperature can be determined numerically. For a particular GB, ($g(l = 0, T), f(l = 0, T)$) is a parametric curve; temperature T is the parameter (the blue curve in Fig. 19). The point where the red and blue curves cross (Fig. 19) corresponds to T_{KT} . Formally, this temperature can also be determined from the condition that f is scale-invariant:

$$T_{\text{KT}} = [2Kb^2\epsilon^{-1}(r_c) - (\psi h + \tau b)r_c] w/3k_B, \quad (5.10)$$

where r_c is the average disconnection separation in the dipoles at T_{KT} ($\epsilon(r_c)$ must be determined numerically). Eq. (5.10) is consistent with the mean-field result Eq. (5.9) ($\epsilon(r_c) = 1$) in the sparse disconnection ($E_c \gg Kb^2w$) and small driving force limits. When multiple disconnection modes are present, T_{KT} is dominated by the disconnection mode with the smallest T_{KT} .

Since the KT transition is associated with the screening of the long-range elastic interactions between disconnections and since disconnection motion is the underlying mechanism of GB migration, the KT transition should lead to a discontinuity in the temperature dependence of the GB mobility. When $T < T_{\text{KT}}$, the activation energy for GB migration Q includes both the disconnection glide barrier E^* and the large scale barrier associated with elastic interactions (Han et al., 2018; Chen et al., 2019, 2020a,b); when $T > T_{\text{KT}}$, the elastic barrier is effectively screened. Hence, increasing T through T_{KT} leads to an abrupt decrease in the activation energy for GB migration Q ; the slope of the GB mobility versus temperature curve should increase abruptly upon heating through T_{KT} . Such an abrupt increase in the GB mobility slope versus T is observed at T_{KT} in the kMC simulations shown below.

Similar results were observed in the molecular dynamics (MD) simulations. Homer et al. (Homer et al., 2014) observed that the slope of the mobility versus temperature of the Ni $\Sigma 39$ [111] (752) symmetrical tilt GB changed abruptly at a finite T . For this GB, $b = a_0/\sqrt{26}$ and $h = 3a_0/\sqrt{78}$ (a_0 is the lattice constant)(Han et al., 2018). With this input and the GB energy $\gamma \approx 0.5$ J/m², thickness $w = 7.5a_0$, $K = 9$ GPa (assuming $r_c \sim w/2$ is the largest disconnection distance in this periodic cell), we find that $\epsilon = 7.6$ from Fig. 19.

and (Eq. (5.10)) $T_{\text{KT}} \approx 800$ K. So, the theoretical prediction of the temperature where an abrupt change of the activation energy for GB mobility is about 800 K, which is close to the MD result under $\psi = 0.025$ eV. (Homer et al., 2014) The MD results of Homer et al. (Homer et al., 2014) also showed that the activation energy for GB migration Q is an approximately linear function of the “roughening temperature”, T_{KT} . We (Chen et al., 2020b) previously showed that the activation energy for GB migration Q varies linearly with Kb^2 and Eq. (5.10) shows that Kb^2 is proportional to T_{KT} ; hence, Q is a linear function of T_{KT} as observed in MD. Based on their MD simulations, Olmsted et al. (Olmsted et al., 2007) observed that at low temperatures and small driving forces, GBs migrate in a start-stop fashion, while at high temperatures/large driving forces, GBs migrate continuously. This may be understood by noting that below the KT transition ($T < T_{\text{KT}}$, which is driving force dependent), disconnection nucleation barriers are high thus disconnection nucleation time is much longer than migration time, while above the transition, nucleation (barriers) times are relatively short (disconnection screening effect) and are comparable with/smaller than migration times (Chen et al., 2020b).

5.2. Kinetic Monte Carlo Simulations

Here, we compare the theoretical analysis with the results of disconnection-based kinetic Monte Carlo (kMC) simulations. Figure 18b shows the basic model employed in our kinetic Monte Carlo (kMC) simulations (the GB tilt axis and nominal GB normal are in z and y and the system is periodic in x). The GB is discretized into N lattice sites along x . The state of GB site i ($1 \leq i \leq N$) is denoted by $(u_i(t), y_i(t))$, where u_i is the relative (tangential) displacement of the upper grain with respect to the lower one (in x) and y_i is the position (in y) of the GB at site i . Formation of a pair of disconnections of mode m ($\pm b_m, \pm h_m$) at i corresponds to $(u_i, y_i) \rightarrow (u_i + b_m, y_i + h_m)$, as illustrated in Fig. 18b. At each kMC time step, we randomly choose from all possible events, weighted by their relative rates (for more details, see Chapter 4 and Chen et al. (2020b)).

For simplicity, we employ reduced variables: $\tilde{\gamma} = \gamma/2\pi K\delta$, $\tilde{h} = h/\delta$, $\tilde{b} = b/\delta$, $\tilde{y} = y/\delta$, $\tilde{t} = t\omega$, $\tilde{M} = 2\pi KM/\omega\delta$, $\tilde{T} = k_{\text{B}}T/2\pi K\delta^2\omega$, $\tilde{\psi} = \psi/2\pi K$, and $\tilde{\tau} = \tau/2\pi K$. In this section,

we drop the “tilde” for simplicity of notation. We report kMC results for two simulation cases: (i) a pure step mode, $h = 1$ and (ii) a single disconnection mode, $b = 1$ and $h = 1$.

For the parameters used in the kMC simulations, the renormalization group analysis (Fig. 19) predicts $T_{\text{KT}} = 0.1$ for the single disconnection mode kMC and $T_{\text{KT}} = 0$ for the pure-step simulations. The roughening transition ($\sigma_y \rightarrow \infty$ and spatial correlation length $\rightarrow \infty$) and screening/sliding transition ($\epsilon \rightarrow \infty$) occur at the same temperature T_{KT} for the case of a GB in a 2d bicrystal.

Figures 20a,b show the standard deviations of the GB profile $\sigma_y = \sqrt{\langle y^2 \rangle - \langle y \rangle^2}$, obtained from the kMC simulations. We recall that the roughening transition occurs at $T = 0$ for pure steps in 2d; this is consistent with Fig. 20a for which the roughness varies smoothly with temperature across the entire simulation temperature range. On the other hand, introduction of a finite disconnection \mathbf{b} (see Fig. 20b) effectively suppresses roughening at low T ($\lesssim T_{\text{KT}}$). At low T the roughness is nearly size-independent; this suggests the presence of very short-range correlations in the GB profile at low T . (The spatial correlation length ξ is the length scale over which the two-point correlation between the heights of different points on the surface decays with their separation.) Above T_{KT} , σ_y increases rapidly with T and a strong size effect (larger roughening in larger systems) is observed. The presence of the near linear dependence of roughness on temperature and a strong size dependence above T_{KT} is reminiscent of the roughening behavior in the pure step case (Fig. 20a) at $T > 0$. These are signatures of a finite- T transition.

In finite- \mathbf{b} systems, the standard deviation of the shear $\sigma_u = \sqrt{\langle u^2 \rangle - \langle u \rangle^2}$ (see the insets in Figs. 20b) show similar behavior as the GB profile roughening. The abrupt change in “shear roughening” suggests that shear roughening is also a characteristic of the disconnection KT transition T_{KT} . (In 3d, the GB profile and shear roughening need not occur at the same T .)

Equilibrium fluctuations in the GB profile provide direct evidence of the GB roughening

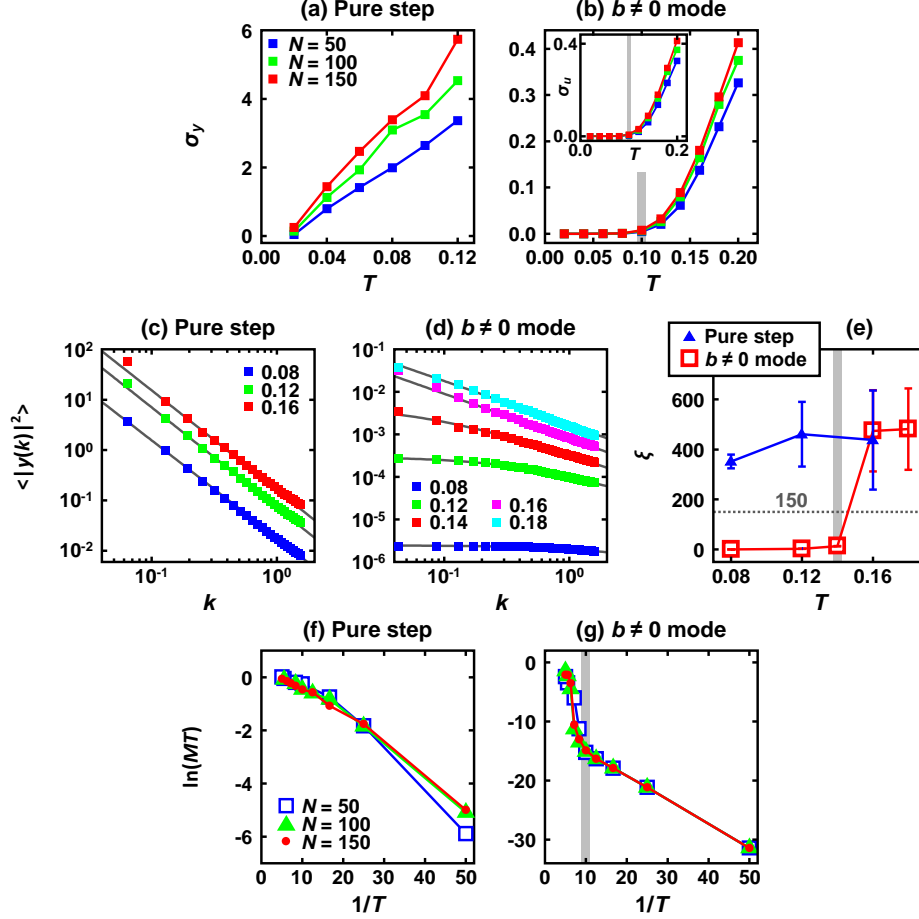


Figure 20: (a)-(b) show the GB roughness σ_y vs. T for the (a) pure step and (b) single mode with $b \neq 0$; the insets in (b) is the standard deviations of shear σ_u vs. temperature T . (c)-(d) show the average of the (square of the) magnitude of the Fourier transform (k is a wave vector) of the equilibrium GB profile $y(x)$, $\langle |y(k)|^2 \rangle$, for several temperatures (see the legend) for the (c) pure step and (d) single mode with $b \neq 0$. (e) shows the correlation length $\xi(T)$ (obtained from fitting $\xi = AT/(k^d + \xi^{-d})$ for each temperature to the kMC data in (c)-(d); the horizontal dashed line (at $\xi = 150$) is the kMC simulation cell period (in x). (f)-(g) show $\ln(MT)$ vs. $1/T$ (Chen et al., 2020a), where M is the GB mobility for the (f) pure step and (g) single mode cases. The vertical gray lines label $T = 0.1$ in (b), and (g), and $T = 0.14$ in (e).

transition. We expand the GB profile in a Fourier series, $y(x, t) = \sum_k y(k, t)e^{ikx}$ and measure the equilibrium static GB profile spectrum $\langle |y(k)|^2 \rangle$, where $\langle \cdot \rangle$ represents a time average. Liao et al. (Liao et al., 2018) demonstrated that for pure steps, this spectrum should be described by

$$\langle |y(k)|^2 \rangle = T/[N\Gamma(k^2 + \xi^{-2})], \quad (5.11)$$

where ξ is the correlation length and Γ is the dimensionless GB stiffness. For disconnection with non-zero \mathbf{b} (Karma et al., 2012),

$$\langle |y(k)|^2 \rangle = T/[N\mathcal{B}^2(k^1 + \xi^{-1})], \quad (5.12)$$

where $\mathcal{B} \equiv b/h$ is the shear coupling factor. As in Liao et al. (2018), a correlation length ξ is introduced as a wavelength cutoff. The KT transition theory suggests that $\xi \rightarrow \infty$ for $T > T_{\text{KT}}$ (Liao et al., 2018).

Figures 20c-d show the spectra obtained from the kMC simulations. These results indeed demonstrate that $\langle |y(k)|^2 \rangle \propto T$, consistent with Eqs. (5.11) and (5.12). The kMC data for each temperature were fitted to the function $AT/(k^d + \xi^{-d})$, where A , d and the correlation length ξ are the fitting parameters (d and ξ are functions of T). For $b = 0$ (Fig. 20c), $d \approx 2$, while when $b \neq 0$ (Figs. 20d), $d \approx 1$; consistent with Eqs. (5.11) and (5.12). The correlation length ξ obtained by the fitting at each temperature is shown in Fig. 20e. Since our kMC simulation were performed using a finite width GB ($N = 150$), we consider the GB roughened when $\xi > 150$. (Since ξ diverges above T_{KT} , it is not possible to obtain accurate measurements of ξ above T_{KT} .) Using this operational definition, we find that when $b = 0$ the GB is rough at all temperatures, but only rough at $T \geq 0.14 \approx T_{\text{KT}}$ for $b \neq 0$. The small difference between the theoretical prediction ($T_{\text{KT}} = 0.1$) and the simulation result ($T_{\text{KT}} = 0.14$) may be attributable to the finite GB width in the simulations and approximations in Eqs. (5.11) and (5.12).

The GB mobility may be related (Trautt et al., 2006) to fluctuations in the mean GB position

\bar{y} : $M = N\bar{y}^2(\Delta t)/2\Delta tT$, where Δt is the time interval used in the calculation of the time correlation \bar{y} . Figures 20f, g show the GB mobilities versus temperature from the kMC simulations. When the operative disconnection mode is a pure step mode (Fig. 20f), the GB mobility behaves in a quasi-Arrhenius fashion; $\ln(MT) \propto -Q/T$ (Chen et al., 2020a), where the activation energy Q (i.e., slope of $\ln(MT)$ vs. $1/T$) is roughly temperature-independent (Q is not exactly temperature-independent since this quasi-Arrhenius relation is inapplicable in cases where the disconnection nucleation time and migration time are comparable; see Chen et al. (2020b) for details). When $b \neq 0$ (Fig. 20g), the activation energy Q (slope) changes abruptly at $T \approx T_{\text{KT}}$. This is because at $T > T_{\text{KT}}$, the elastic fields of the disconnections are effectively screened such that the elastic contribution to the activation energy of disconnection formation is zero. The temperature at which the activation energy for mobility changes ($b \neq 0$) coincides with an abrupt change in both σ_y and/or σ_u (Fig. 20b), i.e., T_{KT} .

The kMC simulations demonstrate that, when the activated disconnection mode has non-zero \mathbf{b} , a finite temperature dynamic phase transition occurs in the GB (provided melting does not occur first). Examination of the standard deviations of the GB profile σ_y and the equilibrium GB fluctuation spectrum $\langle |y(k)|^2 \rangle$ suggests that such a phase transition corresponds to the GB roughening transition. The simultaneous transitions in the behavior of the standard deviations of the GB shear σ_x , the divergence of correlation length ξ above critical temperature and the temperature dependence of GB mobility suggest that the roughening transition is a Kosterlitz-Thouless, topological phase transition. The kMC simulation results suggest that the abrupt changes in the temperature dependencies of σ_y , σ_x , $\langle |y(k)|^2 \rangle$ and M provides clear evidence of a transition temperature for GB dynamics with $b \neq 0$ disconnections (see Fig. 20) at a temperature consistent with the KT transition temperature T_{KT} predicted by the renormalization group theory, $T = 0.1$ (Section 5.1). In other words, finite b disconnection-mediated KT transitions can result in both GB roughening and changes in GB migration behavior.

5.3. Grain Growth Stagnation

Grain growth stagnation is widely observed in both experiments (Barmak et al., 2006) and MD simulations (Holm and Foiles, 2010). Holm and Foiles suggested that this stagnation is associated with the GB roughening transition (Holm and Foiles, 2010). Here, we argue that this behavior is better described in terms of the GB KT transition.

The driving force for grain growth is the reduction of the energy of the GB network in a polycrystal. In classical analyses of normal grain growth, we assume the GB energy is isotropic and GB migration is overdamped. This means that the GB velocity is proportional to its mean curvature H (i.e., mean curvature flow). The chemical potential jump across the GB is $\psi = \gamma H$ and the mean curvature scales (on average) as the inverse of the grain size, D ; ψ decreases as D increases. Eq. (5.10) shows that decreasing ψ (increasing grain size D) implies an increasing KT transition temperature, $T_{\text{KT}}(D)$. Therefore, during isothermal grain growth, the increase in the mean grain size results in fewer and fewer mobile grains (i.e., those with $T_{\text{KT}}(D) < T$). This may lead to grain growth stagnation.

The inverse of the critical grain size is

$$D_{\text{KT}}^{-1} = \left(\frac{1}{\epsilon(r_c)} - \frac{3k_{\text{B}}T}{2Kb^2w} \right) \frac{Kb^2}{r_c\gamma h}. \quad (5.13)$$

Holm and Foiles observed grain growth stagnation at different temperatures in Monte Carlo simulations of polycrystals (Holm and Foiles, 2010); their data (points in Fig. 21) shows that inverse mean grain size at which stagnation occurs D_s^{-1} varies with temperature T in an approximately linear function of T ; as predicted here, Eq. (5.13). When the grain size exceeds D_{KT} , the grain will stop growing or shrinking. Eq. (5.13) suggests that, grain growth continues when $T \geq 2Kb^2w/3\epsilon k_{\text{B}} \equiv T_c$ ($D_{\text{KT}} \rightarrow \infty$).

For nickel (assuming b , h , w and r_c are of the order of one lattice constant, $\epsilon \approx 1$, and $\gamma \approx 1 \text{ J/m}^2$), we find that $T_c \sim 18000 \text{ K}$, which is much higher than the melting point. This implies that grain growth in polycrystalline nickel should always stagnate at a finite

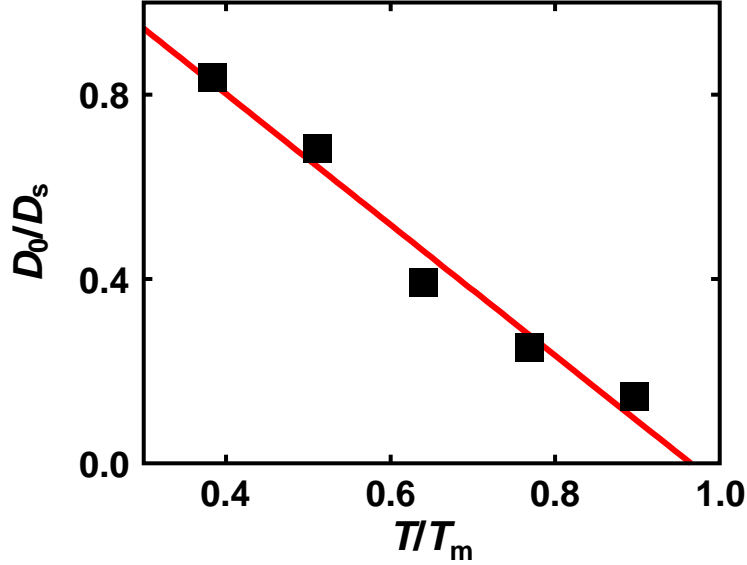


Figure 21: Temperature dependence of stagnated grain size D_s from mesoscale MC simulations (data points) from Holm and Foiles (2010) and a linear fit from Eq. (5.13). D_0 and T_m are the initial grain size and melting point, respectively.

grain size, as observed in MD simulations (Holm and Foiles, 2010). T_c may be decreased substantially by the application of a mechanical load.

Since D_{KT} varies grain-to-grain in a polycrystal, some GBs will show very small mobilities while others will remain mobile. As noted by Holm et al. (Holm et al., 2003), this suggests that abnormal grain growth may readily occur prior to overall grain growth stagnation.

The GB mobility is a tensor, linking both GB shear coupling and migration (Chen et al., 2020a). While the GB migration mobility shows a rapid increase at T_{KT} , the GB sliding coefficient will also increase rapidly at the KT transition temperature. This suggests the existence of a GB sliding transition; consistent with the widespread observations of the onset of superplasticity at small grain sizes or high temperature (Edington et al., 1976) and intergranular fracture at large grain size and low temperature in many materials (Dowling, 1999).

Table 4: Transition temperatures for thermodynamic GB roughening and sliding and where abrupt changes in GB mobilities are expected for pure step ($\mathbf{b} = \mathbf{0}$), pure dislocation ($h = 0$), a single disconnection mode (\mathbf{b}, h), and multiple disconnection modes (\mathbf{b}_m, h_m). A “-” and “0” indicate no transition and a transition temperature at 0 K. The subscripts and superscripts indicate dimensionality (2d/3d) and pure step (S), pure dislocation (D), single disconnection (1), and multiple disconnection (M) modes. M_{11} , M_{12} and M_{22} represent mobilities associated with pure GB migration, shear coupling, and sliding, respectively (Chen et al., 2020a). For multiple disconnection modes, entries only represent the lowest temperature of abrupt mobility changes.

	Pure Step		Pure Dislocation		1 Disconnection Mode		Multiple Disconnection Modes	
	2d	3d	2d	3d	2d	3d	2d	3d
Roughening	0	T_3^S	-	-	T_2^1	T_3^1	0	T_{3r}^M
Sliding	-	-	T_2^D	T_3^D	T_2^1	T_3^1	T_2^M	T_{3s}^M
M_{11}	-	T_3^S	-	-	T_2^1	T_3^1	T_2^M	$\min(T_{3r}^M, T_{3s}^M)$
M_{12}	-	-	-	-	T_2^1	T_3^1	T_2^M	T_{3s}^M
M_{22}	-	-	T_2^D	T_3^D	T_2^1	T_3^1	T_2^M	T_{3s}^M

5.4. Discussion

The theoretical analysis presented above demonstrates that GBs undergo a finite-temperature, Kosterlitz-Thouless, topological phase transition. The topological phase transition implies a transition from smooth to rough GBs, a transition from nearly immobile to highly mobile GBs, and a transition from non-sliding to readily sliding GBs. Because disconnections have dislocation, in addition to step, characters, this transition is topological in nature. While the step character is associated with the rapid change in GB mobility and GB roughening, the dislocation character is associated with the onset of GB sliding at T_{KT} .

The nature of the dynamic phase transition at GBs depends on disconnection character $\{\mathbf{b}, h\}$ and dimensionality (2d or 3d), as summarized in Table 4. For a pure step ($\mathbf{b} = \mathbf{0}$), the transition occurs at $T = 0$ in 2d and at finite T in 3d (Swendsen, 1977). Since this disconnection has $\mathbf{b} = \mathbf{0}$, such a transition leads to roughening and an increase in the GB migration mobility, but not to sliding. For a pure dislocation ($h = 0$), the transition occurs at finite temperature in both 2d and 3d. Since this disconnection has no associated step, such a transition leads to GB sliding, but not roughening. For GB dynamics with a single disconnection mode (finite \mathbf{b} and h), the phase transition leads to roughening, sliding, and a change in all types of mobilities at the same finite temperature $T = T_{KT} = T_d^1$.

While we do not explicitly consider multiple disconnection modes here, we expect that (i) the GB roughening will occur at $T = 0$ in 2d and at finite temperature (T_{3r}^M) in 3d (since pure step modes are always possible) and (ii) a sliding transition at finite temperature in both 2d (T_{2s}^M) and 3d (T_{3s}^M). In the multi-mode case, the mobilities will change abruptly at the topological transitions associated with both the thermodynamic roughening and sliding transitions. In 2d, the GB sliding transition temperature is associated with the smallest, nonzero Burgers vector. Above this temperature, all elastic interactions are screened ($\epsilon \rightarrow \infty$) and no additional KT transitions will occur. Thus there is only one sliding transition in 2d; even when multiple disconnection modes are active. In 3d, two sliding transitions are possible since not all \mathbf{b} are parallel (i.e., the GB is two-dimensional).

Several researchers have demonstrated that grain growth in pure materials often stagnates at a finite grain size (Holm and Foiles, 2010); stagnation is also seen as a pre-requisite to abnormal grain growth (a small set of grains grow to be much larger than the mean grain size) (Holm et al., 2003). Both stagnation and abnormal grain growth may further or hinder achievement of targeted material properties. The presented observations suggest that grain growth stagnation is associated with the difficulty of disconnection formation/migration below the GB transition temperature ($T < T_{KT}$; see Eq. 5.13 and Fig. 20). This is clear in our 2d simulations, where the GB mobility increases rapidly above T_{KT} (Fig. 20g) whereas the roughening temperature is 0 K (*cf.* Fig. 20a; the 2d multi-mode cases in Table 4.)

Ample evidences (experiments, simulations and theories) demonstrate that many aspects of GB dynamics are associated with the formation and motion of disconnections (Han et al., 2018). We presented mean-field and renormalization group theory results and kinetic Monte Carlo evidence for a finite-temperature, disconnection unbinding phase transition (of the Kosterlitz-Thouless type) in GBs. This disconnection unbinding phase transition is characterized by a finite-temperature transition in GB migration, roughening and sliding. Associated with these are abrupt changes in the activation energies for the mobilities associated with GB migration and GB sliding at T_{KT} . These results provided a unified view

of widely-observed feature of grain growth stagnation, abnormal grain, and superplasticity. Finally, we note that while other types of GB phase transitions (e.g., first-order structural phase transitions) may occur and affect GB properties, the disconnection-based KT transition theory gives a unified vision of a wide range of physical phenomena and testable predictions of how these depend on both temperature and grain size.

CHAPTER 6 : Final Remarks

Since GB migration and GB sliding are coupled, we extend the notion of the GB velocity-driving force relation applied throughout the field to account for both this coupling and the inter-relation between the different types of GB motion (migration and sliding). The natural extension is from a scalar velocity-mobility-driving force relation to one in which the velocity and forces may be thought of as vectors and the mobility as a second rank tensor. The kinetic equation suggests the definition of a GB mobility tensor, \mathbf{M} . We determine the full GB mobility tensor and its temperature dependence for symmetric tilt GBs in copper via molecular dynamics (MD) simulations. We are able to explain this temperature dependence, as well as several general properties of the mobility tensor, based upon analysis of a disconnection model. To explain all the complicated temperature dependence of mobility observed in MD and experiments, we develop both analytical statistical mechanics models and disconnection-based kMC simulations. These analytical models, kMC, and MD quantitatively agree with each other. Shear coupling factors, as ratios between components of the mobility tensor, naturally depend on the type, direction and magnitude of driving force and temperature. In particular, we show that the effective GB migration mobility will be smaller than that expected based upon bicrystal experiments as a result of stress generation during grain growth in polycrystalline systems.

We also presented mean-field and renormalization group theory results and kinetic Monte Carlo evidence for a finite-temperature, disconnection unbinding phase transition (of the Kosterlitz-Thouless type) in GBs. This disconnection unbinding phase transition is characterized by a finite-temperature transition in GB migration, roughening and sliding. Associated with these are abrupt changes in the activation energies for the mobilities associated with GB migration and GB sliding at T_{KT} . These results provide a unified view of widely observed features of grain growth stagnation, abnormal grain, and superplasticity.

With an eye to the future, extending our research to more complicated GB systems, e.g.,

polycrystals, asymmetric mixed GBs, or disconnection loops on GBs, is visible:

Disconnection Loops All presented disconnection models are for parallel disconnection lines on GBs, and extending our model for disconnection loops on GBs is of practical interest. The dislocation loop-based kMC simulations and KT transition theory are feasible.

General GBs Current work on shear coupling focuses on symmetric tilt GBs. Developing similar theory and MD simulations for general (asymmetric or mixed) GBs, where little research exists, is interesting.

Triple Junctions We mostly study the temperature dependence of GB mobility in bicrystals by MD and kMC simulations, but GBs in polycrystals may show different behavior due to triple junctions. Extending our analytical theory and kMC simulations to study triple junction mobility in polycrystals is feasible.

Dislocation-GB Interaction Understanding whether and how fast dislocations transmit across GBs is important. When a lattice dislocation is absorbed by a GB, this dislocation may interact with GB disconnections, affecting dislocation transmission barriers.

Visualization of Disconnections Developing an automatic method to identify disconnections on GBs from the outputs of MD simulations is useful. This may be achievable by describing atomistic environments by SOAP (Smooth Overlap of Atomic Positions) descriptors (Bartok et al., 2013) and then performing machine learning to classify atoms as bulk atoms, GB atoms, or disconnection atoms.

APPENDIX

A.1. The Parameters C^x and β_0^x

We can expand the shear coupling factor β for stress-driven GB migration (Eq. (2.2) in the main text)

$$\beta = \frac{\sum_i b_i e^{-\frac{Q_i}{k_B T}} \sinh \frac{(b_i \tau - h_i \psi) S}{k_B T}}{\sum_i h_i e^{-\frac{Q_i}{k_B T}} \sinh \frac{(b_i \tau - h_i \psi) S}{k_B T}} \quad (\text{A.1})$$

at high temperature to third order in $bS\tau/k_B T$. This yields $\beta = C^\tau \tau^2 + \beta_0^\tau$, where

$$C^\tau = \frac{\frac{S^2}{6k_B^2 T^2} (\sum_i e^{-\frac{Q_i}{k_B T}} b_i^4 - \sum_i e^{-\frac{Q_i}{k_B T}} b_i^2 \sum_i e^{-\frac{Q_i}{k_B T}} h_i b_i^3)}{\sum_i e^{-\frac{Q_i}{k_B T}} h_i b_i} \quad (\text{A.2})$$

$$\beta_0^\tau = \frac{\sum_i e^{-\frac{Q_i}{k_B T}} b_i^2}{\sum_i e^{-\frac{Q_i}{k_B T}} h_i b_i}. \quad (\text{A.3})$$

Similarly, expanding Eq. (A.1) at high temperature to third order in $hS\psi/k_B T$ yields $\beta = C^\psi \psi^2 + \beta_0^\psi$, where

$$C^\psi = \frac{\frac{S^2}{6k_B^2 T^2} (\sum_i e^{-\frac{Q_i}{k_B T}} h_i^3 b_i - \sum_i e^{-\frac{Q_i}{k_B T}} h_i b_i \sum_i e^{-\frac{Q_i}{k_B T}} h_i^4)}{\sum_i e^{-\frac{Q_i}{k_B T}} h_i^2} \quad (\text{A.4})$$

$$\beta_0^\psi = \frac{\sum_i e^{-\frac{Q_i}{k_B T}} h_i b_i}{\sum_i e^{-\frac{Q_i}{k_B T}} h_i^2}. \quad (\text{A.5})$$

At relatively low temperature ($b\tau S \ll k_B T \ll Q$, $h\psi S \ll k_B T$), $C^x \rightarrow 0$. This implies that at low temperature, the shear-coupling factor is determined by the lowest barrier mode and is insensitive to magnitude of driving force.

A.2. Limiting Behavior for Shear Coupling Factor

The driving force affects the shear-coupling factor β by tilting the energy landscape thereby lowering disconnection nucleation barriers. While large stresses favor disconnection modes of (relatively) large Burgers vector and small step height, large chemical potential jumps favor modes of (relatively) small Burgers vector and large step height (especially pure step modes where $\mathbf{b} = 0$). This implies different values of β for different driving forces. More specifically, under an applied stress, $|\beta|$ tends to be larger than under a chemical potential jump. Even in the small driving force limit, β depends on the type of driving force; except in special cases, e.g., at low temperature and finite β . When the stress-driving force is large ($\tau \rightarrow \infty$), GB sliding occurs ($\beta \rightarrow \infty$); this is because stress favors modes of large Burgers vector and negligible step height. On the other hand, when the chemical potential jump driving force is large ($\psi \rightarrow \infty$), the GB migrates without coupling ($\beta \rightarrow 0$); this is because chemical potential jumps favor modes of negligible Burgers vector and large step height.

Even at high temperatures, GBs migrate by the nucleation and motion of disconnections (Han et al., 2018), each with a specific Burgers vector (leading to grain translation) and step height (leading to GB migration). In the high temperature limit ($T \rightarrow \infty$), many disconnections modes are activated simultaneously. Hence, chemical potential jump-driven GB migration occurs with no net grain translation ($\beta \rightarrow 0$) because disconnections with the same sign of h but opposite signs of \mathbf{b} are nucleated such that the average $\mathbf{b} = 0$. Similarly, when driven by stress at high temperature, grain boundaries slide ($\beta \rightarrow \infty$) because disconnections with the same sign of $\mathbf{b} = 0$ but opposite signs of h are nucleated such that the average $h = 0$.

A.3. Enumeration of Modes

Following the approach outlined in (Han et al., 2018), we present a simplified method to enumerate all crystallographically possible disconnection modes (\mathbf{b}, h) for $[001](m, n, 0)$ GBs

($0 < n < m$, and $n + m$ is even). First, we define

$$\tilde{d}_y = 2m \quad (\text{A.6})$$

$$\tilde{d}_z = 2n \quad (\text{A.7})$$

$$\tilde{d}_{GB} = n^2 + m^2 \quad (\text{A.8})$$

$$\tilde{d} = 2 \quad (\text{A.9})$$

$$\tilde{d}_{1L} = \frac{k_2 \tilde{d}_{GB} - 2\tilde{d}_y}{\tilde{d}_z} \quad (\text{A.10})$$

$$a_y = \frac{a}{2\sqrt{n^2 + m^2}}, \quad (\text{A.11})$$

where a is the lattice parameter and k_2 is the smallest positive integer to make \tilde{d}_{1L} an even number. We further define

$$d^* = \frac{\tilde{d}}{[\tilde{d}_{GB}, \tilde{d}_{1L}]} \quad (\text{A.12})$$

$$d_{GB}^* = \frac{\tilde{d}_{GB}}{[\tilde{d}_{GB}, \tilde{d}_{1L}]} \quad (\text{A.13})$$

$$d_{1L}^* = \frac{\tilde{d}_{1L}}{[\tilde{d}_{GB}, \tilde{d}_{1L}]} \quad (\text{A.14})$$

$$\tilde{h}_0 = d^* d_{1L}^{*\Phi(d_{GB}^*)-1} \bmod d_{GB}^* \quad (\text{A.15})$$

where $[x, y]$ is the greatest common divisor of x and y and $\Phi(x)$ is the Euler's totient function. Then, all crystallographically possible (\mathbf{b}, h) whose Burger's vector is parallel to the y -axis are

$$\mathbf{b}_q = (0, a_y q \tilde{d}, 0) \quad (\text{A.16})$$

$$h_{qj} = a_y (q \tilde{h}_0 + j d_{GB}^*), \quad (\text{A.17})$$

where q and j are arbitrary integers.

A.4. Coupling Factor in the Framework of Mobility Tensor

The coupling factor β depends on the direction of the tangential displacement of one grain relative to the other, k , and the nature of the driving force

$$\beta_k = \frac{v_k}{v_1} = \frac{M_{k1}\psi + M_{k2}\tau_2 + M_{k3}\tau_3}{M_{11}\psi + M_{12}\tau_2 + M_{13}\tau_3}. \quad (\text{A.18})$$

The temperature (T) dependence of the coupling factor (β) for the $\Sigma 7$ [111] ($12\bar{3}$) GB in copper is shown in Fig. 22 based on the mobility data in Fig. 9 of the main text. Below 1000 K, β_2 is nearly constant and $\beta_3 \sim 0$, suggesting that single mode behavior dominates in this temperature range. Above 1000 K, β increases with temperature, suggesting that multiple disconnection modes are active.

A.5. Grain Growth in 3- and d -dimensions

The von Neumann-Mullins law was previously generalized from 2 to d -dimensions (MacPherson and Srolovitz, 2007). Following that approach, we may write the rate of growth of a grain in d -dimensions as

$$\dot{R} = mg\gamma/R \quad (\text{A.19})$$

and

$$g \equiv C \left[\frac{H_{d-2}(\mathbf{D}_{d-2})}{6H_{d-2}(\mathbf{D}_d)} - 1 \right], \quad (\text{A.20})$$

where \mathbf{D}_d refers to the grain of interest in d -dimensions, \mathbf{D}_{d-2} is the $(d-2)$ -dimensional feature of the domain \mathbf{D}_d (e.g. vertices in 2D and edges in 3D), H_{d-2} is the Hadwiger $(d-2)$ -measure from geometric probability and the constant C depends on the detailed grain shape (see MacPherson and Srolovitz (2007); Klain and Rota (1997)).

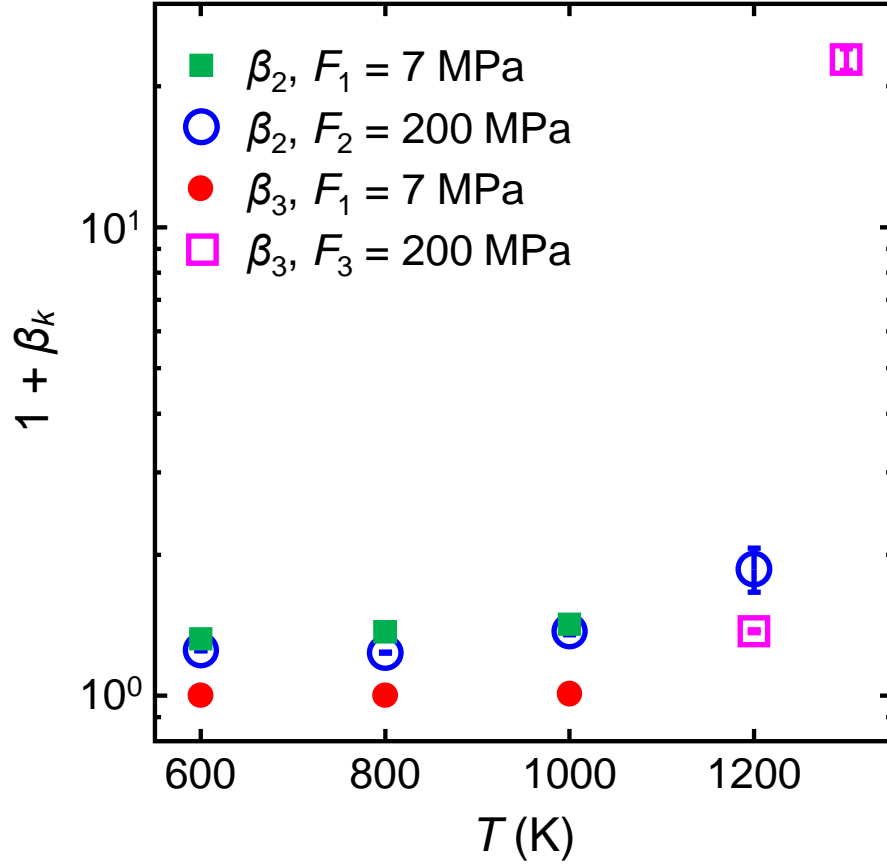


Figure 22: The temperature (T) dependence of the coupling factor (β) for the $\Sigma 7$ [111] $(12\bar{3})$ GB in copper obtained from the MD simulation data reported in Fig. 9 of the main text.

In d -dimensions, the general kinetic equation is

$$\begin{pmatrix} \dot{R} \\ -\dot{\tau}_2 R / \mu \\ \vdots \\ -\dot{\tau}_d R / \mu \end{pmatrix} = \begin{pmatrix} M_{11} & M_{12} & \cdots & M_{1d} \\ M_{21} & M_{22} & \cdots & M_{2d} \\ \vdots & \vdots & \ddots & \vdots \\ M_{d1} & M_{d2} & \cdots & M_{dd} \end{pmatrix} \begin{pmatrix} g\gamma/R \\ \tau_2 \\ \vdots \\ \tau_d \end{pmatrix}. \quad (\text{A.21})$$

In the $R \rightarrow \infty$ limit, the solution to this equation is

$$R^2 - R_0^2 = 2(d-1)\tilde{m}g\gamma t \quad (\text{A.22})$$

and

$$\tilde{m} = \frac{|\mathbf{M}|}{M_{11}^*} = [(\mathbf{M}^{-1})_{11}]^{-1}, \quad (\text{A.23})$$

where \mathbf{M}^* is the adjugate of \mathbf{M} . Eq. (A.23) indicates that for a long time grain growth always follows the parabolic law. But, instead of the commonly used mobility M_{11} , the effective GB mobility should be $[(\mathbf{M}^{-1})_{11}]^{-1}$.

The corresponding evolution of the shear stress τ_i is, in the long time limit,

$$\tau_i = \frac{(d-1)g\gamma M_{1i}^*}{M_{11}^* R} = \frac{(d-1)g\gamma(\mathbf{M}^{-1})_{1i}}{(\mathbf{M}^{-1})_{11} R}. \quad (\text{A.24})$$

This equation demonstrates that at long time the stress decays as $1/R$ or $t^{-1/2}$; however, this stress can be significant during typical grain growth experiments (especially in nanocrystalline materials).

In 3-dimensions, these equations reduce to

$$R^2 - R_0^2 = 4\tilde{m}g\gamma t \quad (\text{A.25})$$

with

$$g \equiv C \left(\frac{\mathcal{E}}{6\mathcal{L}} - 1 \right), \quad (\text{A.26})$$

where \mathcal{L} is the mean width of the grain and \mathcal{E} is the total length of all triple lines around the grain and where \tilde{m} is the same as in Eq. A.23. The corresponding evolution of the shear stress τ_i is, in the long time limit,

$$\tau_i = \frac{2g\gamma M_{1i}^*}{M_{11}^* R} = \frac{2g\gamma(\mathbf{M}^{-1})_{1i}}{(\mathbf{M}^{-1})_{11} R}. \quad (\text{A.27})$$

A.6. The Elastic Energy and Stress in the Kinetic Monte Carlo Simulations

In this section, we provide more details associated with the derivation of Eqs. (4.3) and (4.5) of the main text. Consider an array of disconnections with Burgers vector $\mathbf{b} = b\mathbf{e}_2$

and line direction \mathbf{e}_1 in the coordinate system of Fig. 11 of the main text. Because the system is periodic with periodicity L , there is an infinite set of disconnections at positions $x_2 = nL$ (n is an integer). Then, the shear stress anywhere in space associated with this array of disconnections is

$$\tau(x_2, x_3) = \tau_0 \sin(2\pi X_2) [\cosh(2\pi X_3) - \cos(2\pi X_2) - 2\pi X_3 \sinh(2\pi X_3)], \quad (\text{A.28})$$

where

$$\tau_0 \equiv -\frac{2\pi K b}{L} \frac{1}{[\cosh(2\pi X_3) - \cos(2\pi X_2)]^2}, \quad (\text{A.29})$$

and $X_2 \equiv x_2/L$ and $X_3 \equiv x_3/L$. The shear stress at the disconnection at x_2 (and $x_3 = 0$) associated with all the periodic image disconnections at $x'_2 + nL$ is

$$\tau(x_2, 0) = \frac{2\pi K b}{L} \cot \left[\frac{\pi}{L} (x'_2 - x_2) \right]. \quad (\text{A.30})$$

Associated with each site i in the lattice is a displacement of the grain above this site relative to the grain below it, u_i (see Fig. 11 of the main text). The displacement difference between sites i and $i + 1$ is simply the Burgers vector of the disconnection residing at the midpoint between these two sites. Then, according to Eq. (A.30), for a given distribution of displacements $\{u_i\}$, the shear stress at site j is

$$\tau_j = \frac{2\pi K}{L} \sum_{l=1}^N (u_l - u_{l-1}) \cot \left[\frac{\pi}{N} \left(l - \frac{1}{2} - j \right) \right], \quad (\text{A.31})$$

where we let $u_0 = u_N$ (i.e., the system is periodic) and the summation is over all sites in the simulation cell.

If the state of the i^{th} site undergoes the transition: $u_i \rightarrow u_i + b \equiv u_i^+$, how does the stress field evolve? Consider the stress at arbitrary site j before and after the transition at site i .

Before the transition, the stress at site j is (i.e., we rearrange Eq. (A.31)):

$$\begin{aligned} \tau_j^{(0)} = & \frac{2\pi K}{L} \left\{ \sum_{l \neq i, i+1}^N (u_l - u_{l-1}) \cot \left[\frac{\pi}{N} \left(l - \frac{1}{2} - j \right) \right] \right. \\ & \left. + (u_i - u_{i-1}) \cot \left[\frac{\pi}{N} \left(i - \frac{1}{2} - j \right) \right] + (u_{i+1} - u_i) \cot \left[\frac{\pi}{N} \left(i + \frac{1}{2} - j \right) \right] \right\}, \end{aligned} \quad (\text{A.32})$$

where the superscript “(0)” indicates the state of the system before the transition. After the transition, Eq. (A.32) becomes

$$\begin{aligned} \tau_j^{(1)} = & \frac{2\pi K}{L} \left\{ \sum_{l \neq i, i+1}^N (u_l - u_{l-1}) \cot \left[\frac{\pi}{N} \left(l - \frac{1}{2} - j \right) \right] \right. \\ & \left. + (u_i^+ - u_{i-1}) \cot \left[\frac{\pi}{N} \left(i - \frac{1}{2} - j \right) \right] + (u_{i+1} - u_i^+) \cot \left[\frac{\pi}{N} \left(i + \frac{1}{2} - j \right) \right] \right\} \\ = & \tau_j^{(0)} + \frac{2\pi K b}{L} \left\{ \cot \left[\frac{\pi}{N} \left(i - \frac{1}{2} - j \right) \right] - \cot \left[\frac{\pi}{N} \left(i + \frac{1}{2} - j \right) \right] \right\}. \end{aligned} \quad (\text{A.33})$$

This is exactly Eq. (4.5) in the main text which suggests how the stress on each site will be updated after the occurrence of a transition event.

The stress at site i in the unit cell associated with this transition arises from all of the periodic images of site i ; i.e.,

$$\tau_i^{(1)} = \tau_i^{(0)} - \frac{4\pi K b}{L} \cot \left(\frac{\pi}{2N} \right), \quad (\text{A.34})$$

where we have simply substituted $j = i$ in Eq. (A.33). The energy change of the system when there is a state transition at site i is the product of the stress field at site i and the change in displacement there (i.e., virtual work). There are no other contributions from other sites, since site i is the only site for which the displacement changed (by b). The work done in the transition at site i (u_i^+) is equivalent to displacing the disconnection across the

width of site i (δ); i.e.,

$$W^I = - \int_{x_i - \delta/2}^{x_i + \delta/2} \tau_i(x) b \, dx \approx - \frac{(\tau_i^{(1)} + \tau_i^{(0)})\delta}{2} b = -\tau_i^{(0)} b \delta + \frac{2\pi K b^2 \delta}{L} \cot\left(\frac{\pi}{2N}\right). \quad (\text{A.35})$$

Here, the displacement of the disconnection is in $x = x_2$ and the middle expression is based upon a discrete approximation to the integral (i.e., trapezoidal rule). This is exactly Eq. (4.3) in the main text.

A.7. Configurational Entropy and Equilibrium Disconnection Concentration

In this section, we evaluate the configurational entropy and free energy associated with the distribution of disconnections and the equilibrium disconnection density, as quoted in the main text. Assume that only disconnections of one mode are activated along a grain boundary (GB). For simplicity, we assume that these disconnections are associated with evenly spaced disconnection dipoles with a dipole separation, L . If the system is discretized into N sites and the number of disconnection dipoles is n , the configurational entropy (per unit thickness) is

$$S = k_B w^{-1} [N \ln N - n \ln n - (N - n) \ln(N - n)] \quad (\text{A.36})$$

$$= k_B w^{-1} N \left[\ln\left(\frac{N}{N - n}\right) - \frac{n}{N} \ln\left(\frac{n}{N - n}\right) \right] \quad (\text{A.37})$$

$$= k_B w^{-1} N \left[\ln\left(\frac{1}{1 - \delta/L}\right) - \frac{\delta}{L} \ln\left(\frac{\delta/L}{1 - \delta/L}\right) \right], \quad (\text{A.38})$$

where we have employed Stirling's approximation and set $n/N = \delta/L$. The corresponding free energy (per unit thickness) is

$$F = E - TS = nE^c - k_B T w^{-1} [N \ln N - n \ln n - (N - n) \ln(N - n)], \quad (\text{A.39})$$

where $E^c = 2\gamma|h| + 2\zeta K b^2$ is the energy for form a disconnection dipole on one site (i.e., the energy associated with disconnection cores). The equilibrium number of disconnections

is found from:

$$0 = \left(\frac{dF}{dn} \right)_N = E^c + k_B T w^{-1} \ln \left(\frac{n}{N-n} \right) \Rightarrow \frac{n}{N-n} = \exp \left(-\frac{E^c}{k_B T/w} \right). \quad (\text{A.40})$$

Hence, the equilibrium separation between disconnection dipoles is

$$\frac{L}{\delta} = 1 + \exp \left(\frac{E^c}{k_B T/w} \right) \quad (\text{A.41})$$

or, equivalently, the equilibrium disconnection dipole concentration is

$$\frac{\delta}{L} = \left[1 + \exp \left(\frac{E^c}{k_B T/w} \right) \right]^{-1}. \quad (\text{A.42})$$

In the low-temperature limit (i.e., $\exp[E^c/(k_B T/w)] \gg 1$), we find

$$\frac{\delta}{L} = \exp \left(-\frac{E^c}{k_B T/w} \right). \quad (\text{A.43})$$

This is Eq. (8) in the main text.

We estimate the error by replacing the actual disconnection density with its low temperature limit by focussing on the highest accessible temperature, i.e., the melting point. We also ignore the disconnection core energy relative to the entropic contribution in the free energy and choose reasonable parameter values, $|h| \sim 1 \text{ \AA}$ and $w = 10 \text{ \AA}$. Consider three typical metals: (i) Ni, $\gamma = 0.4 \text{ J/m}^2$ and $T_m = 1565 \text{ K}$; (ii) Al, $\gamma = 0.2 \text{ J/m}^2$ and $T_m = 939 \text{ K}$; and (iii) Cu, $\gamma = 0.3 \text{ J/m}^2$ and $T_m = 1350 \text{ K}$. The melting points were determined for the EAM potentials: Foiles-Hoyt Ni (Foiles and Hoyt, 2006), Ercolessi-Adams Al (Ercolessi and Adams, 1994), and Mishin Cu (Mishin et al., 2001). The GB energies are conservative estimates of the energies of high-angle GBs obtained by Holm et al. (Holm et al., 2010) using same set of EAM potentials. For these three metals, the error associated with our low temperature approximation (i.e., omitting the “1” in Eq. (A.42)) is only 2-4%.

At equilibrium, the configurational entropy per unit thickness and in a period (the period

is L) is

$$S = k_{\text{B}}w^{-1} \frac{L}{\delta} \left[\ln \left(\frac{1}{1 - \delta/L} \right) - \frac{\delta}{L} \ln \left(\frac{\delta/L}{1 - \delta/L} \right) \right] \quad (\text{A.44})$$

$$\begin{aligned} &= k_{\text{B}}w^{-1} \left[\frac{L}{\delta} \ln \left(\frac{1}{1 - \delta/L} \right) - \ln \left(\frac{\delta/L}{1 - \delta/L} \right) \right] \\ &\approx k_{\text{B}}w^{-1} \left[1 - \ln \left(\frac{\delta}{L} \right) + O \left(\frac{\delta}{L} \right) \right] \approx k_{\text{B}}w^{-1} \ln \left(\frac{eL}{\delta} \right) \approx k_{\text{B}}w^{-1} + \frac{E^{\text{c}}}{T}. \end{aligned} \quad (\text{A.45})$$

The approximations in the second line in this equation were to let $\delta/L \rightarrow 0$ and to employ Eq. (A.43) in place of Eq. (A.42). Multiplying both sides of Eq. A.44 by T yields Eq. (9) in the text.

A.8. Consistency between Lattice Model and Continuum Theory

Consider the formation of a disconnection dipole on an infinitely large, otherwise flat GB. In classical continuum dislocation theory (Hirth and Lothe, 1982), the energy of a pair of dislocations $\pm b$ separated by R is

$$\Delta E^{\text{S}}(R) = 2\zeta K b^2 + 2K b^2 \ln \left(\frac{R}{r_0} \right), \quad (\text{A.46})$$

where the first term is the dislocation core energy where the dimensionless parameter ζ and the dislocation core size is r_0 should be chosen self-consistently. We can rewrite this equation as

$$\Delta E^{\text{S}}(R) = 2K b^2 \ln \left(\frac{R}{\delta_0} \right), \quad (\text{A.47})$$

where $\delta_0 \equiv r_0 e^{-\zeta}$ is the effective core size. Hence, there is only one parameter δ_0 , rather than two (ζ and r_0) in the continuum theory. However, in the lattice model employed in the kMC simulations here, ζ is required, along with the spacing between lattice sites δ ; i.e., the lattice model has two parameters, ζ and δ . However, we can define the relationship between ζ and δ to be consistent with the continuum theory, as described below.

Consider the formation of a disconnection pair in an initially disconnection-free GB of infinite extent. The change in energy of the system on the formation of a disconnection

pair (within the lattice model) may be described by reference to Fig. (23). Further, we assume that the GB is initially stress free: $\tau_i^{(0)} = 0$ and set the zero of energy to be that of the disconnection-free GB (Fig. (23)a). In the discrete model, the transition $(u_i, z_i) \rightarrow (u_i + b, z_i - h)$ corresponds to the formation of a pair of disconnections separated by δ (Fig. (23)b). The stress at site i produced by the formation of this disconnection dipole is

$$\tau_i^{(1)} = -\frac{2Kb}{\delta/2} - \frac{2K(-b)}{-\delta/2} = -8Kb/\delta. \quad (\text{A.48})$$

This corresponds to the motion of a disconnection across site i (i.e., a distance δ - as described in Section A.7). The associated work is found from Eq. (A.35):

$$W^I = -\tau_i b \delta = 4Kb^2. \quad (\text{A.49})$$

Following Eq. (4.1) in the main text, the change of the total energy associated with the change of state due to the transition depicted in Fig. 23 is

$$\Delta E_{\text{lattice}}^S = \Delta E^c + W^I + W^E = (2\gamma|h| + 2\zeta Kb^2) + 4Kb^2 + 0 = 2\gamma|h| + 2Kb^2(\zeta + 2). \quad (\text{A.50})$$

Now, consider the change of energy associated with the formation of a disconnection dipole based on the continuum theory, is as given in Eq. (A.47). For a disconnection pair separation of δ , this change in energy is

$$\Delta E_{\text{continuum}}^S = 2\gamma|h| + 2Kb^2 \ln(\delta/\delta_0). \quad (\text{A.51})$$

The lattice and continuum models yield the same disconnection dipole formation energy provided that $\Delta E_{\text{lattice}}^S = \Delta E_{\text{continuum}}^S$. Inserting Eqs. (A.50) and (A.51) into this equality implies

$$\zeta + 2 = \ln(\delta/\delta_0). \quad (\text{A.52})$$

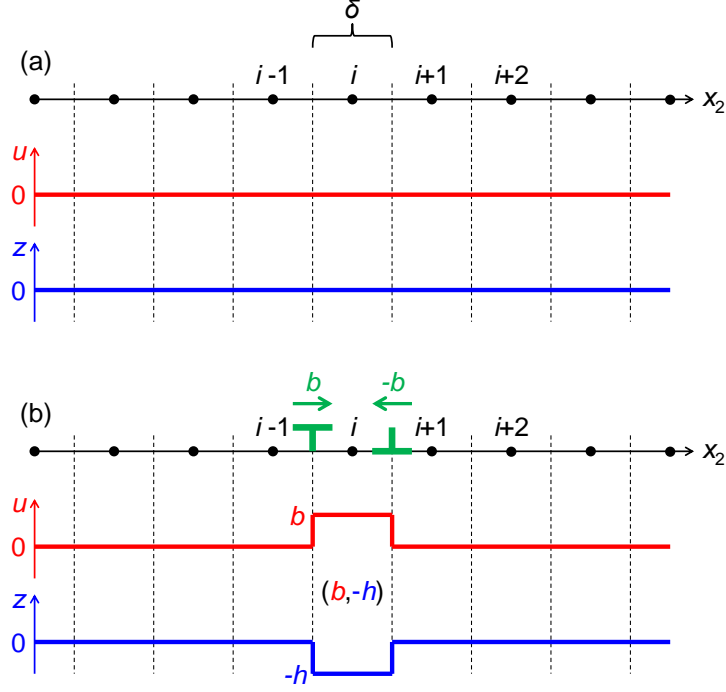


Figure 23: Lattice-model description of the formation of a disconnection pair (dipole), $(b, -h)$ and $(-b, h)$, on site i .

Hence, the lattice and continuum models are consistent provided that ζ and δ satisfy Eq. (A.52).

A.9. Grain Boundary Roughness

Consider a (1d) tilt grain boundary (GB) separating a pair of (2d) grains. In this situation, disconnections nucleate and migrate along the x -axis. For simplicity, we assume that there is only one disconnection mode (b, h) activated on the GB. When a disconnection pair nucleates, a hypothetical “string” is defined between them. The length of the string is the separation of the two disconnections r . The sign of the string is the same as the sign of h . We assume that at position x , the number of positive strings is $v_+(x)$, and the number of negative strings is $v_-(x)$; thus, the GB height at x is $y(x) = h[v_+(x) - v_-(x)]$ and the total string number is $v(x) = v_+(x) + v_-(x)$.

Assume that when the GB is at equilibrium at a particular temperature, n is constant at any point along the GB and at any time. At an arbitrary point, there are n strings; the

probability for them being positive is 1/2, i.e.,

$$\langle v_+ \rangle = \frac{v}{2}. \quad (\text{A.53})$$

The average squared number of positive strings is

$$\langle v_+^2 \rangle = \sum_{i=0}^v i^2 P(v_+ = i) = \sum_{i=0}^v \frac{i^2}{2^v} \binom{v}{i} = \sum_{i=0}^v \frac{i^2}{2^v} \frac{v!}{i!(v-i)!} = \frac{v^2 + v}{4}. \quad (\text{A.54})$$

According to the definition of GB roughness, the squared roughness is

$$\begin{aligned} \sigma_y^2 &= \langle y^2 \rangle = h^2 \langle (v_+ - v_-)^2 \rangle \\ &= h^2 \langle (2v_+ - v)^2 \rangle = h^2 \langle 4v_+^2 + v^2 - 4v_+v \rangle \\ &= h^2 (4\langle v_+^2 \rangle + v^2 - 4v\langle v_+ \rangle) = h^2 v. \end{aligned} \quad (\text{A.55})$$

So, the GB roughness is proportional to the total number of strings per point (i.e., the string density).

Assume that there are many disconnection dipoles on the GB, with separation r and the distance between dipoles L . Then, the density of disconnection dipoles is $\langle L \rangle^{-1}$. Each pair contributes a string of length $\langle r \rangle$. Thus, the average total string number at one point is

$$\langle v \rangle = \frac{S}{\langle L \rangle} \frac{\langle r \rangle}{S} = \frac{\langle r \rangle}{\langle L \rangle} \approx \left\langle \frac{r^2}{L^2} \right\rangle^{1/2} = \frac{e^{-2\beta E_c}}{(2\beta K b^2 - 3)(2\beta K^2 - 1)}, \quad (\text{A.56})$$

where S is the total length of the 1d GB. So, v and thus σ_y^2 diverge at the critical temperature

$$T_{\text{KT}} = 2Kb^2/3k_B. \quad (\text{A.57})$$

Hence, for a 1d GB, roughening transition occurs at T_{KT} , i.e., the KT transition temperature.

When $T < T_{\text{KT}}$, both r and L are finite and as long as $S \gg r$ and l , the roughness should be

nearly size-independent. When $T_{\text{KT}} < T < 3T_{\text{KT}}$, however, $r \rightarrow \infty$ and the finite size effect is strong. In this case, the average string length contributed from each pair is S instead of $\langle r \rangle$ in a finite size simulation. Replacing $\langle r \rangle$ with S in Eq.(A.55) and (A.56), we have

$$\sigma_y^2 = \frac{Sh^2 e^{-2\beta E_c}}{\delta(2\beta K b^2 - 1)} \propto S. \quad (\text{A.58})$$

When $T > 3T_{\text{KT}}$, $\langle L \rangle < \delta$. This introduces another size effect such that $\langle L \rangle$ should be replaced with δ in Eq.(A.55) and (A.56),

$$\sigma_y^2 = \frac{Sh^2}{\delta} \propto S. \quad (\text{A.59})$$

BIBLIOGRAPHY

- Aust, K. and U. Rutter
1959a. Grain boundary migration in high-purity lead and dilute lead-tin alloys. *Transactions of the American Institute of Mining and Metallurgical Engineers*, 215(1):119–127.
- Aust, K. and U. Rutter
1959b. Temperature dependence of grain migration in high-purity lead containing small additions of tin. *Transactions of the American Institute of Mining and Metallurgical Engineers*, 215(1):820–831.
- Bainbridge, D. W., H. L. Choh, and E. H. Edwards
1954. Recent observations on the motion of small angle dislocation boundaries. *Acta Metallurgica*, 2(2):322–333.
- Balluffi, R. W., A. Brokman, and A. H. King
1982. CSL/DSC Lattice model for general crystal-crystal boundaries and their line defects. *Acta Metallurgica*, 30(8):1453–1470.
- Barmak, K., J. Kim, C. S. Kim, W. E. Archibald, G. S. Rohrer, A. D. Rollett, D. Kinderlehrer, S. Ta'Asan, H. Zhang, and D. J. Srolovitz
2006. Grain boundary energy and grain growth in Al films: Comparison of experiments and simulations. *Scripta Materialia*, 54(6):1059–1063.
- Bartok, A. P., R. Kondor, and G. Csanyi
2013. On representing chemical environments. *Physical Review B - Condensed Matter and Materials Physics*, 87(18):184115.
- Biscondi, M. and C. Goux
1968. Intercrystalline creep of oriented aluminium bicrystals. *Mem Sci Rev Met*, 65(2):167–179.
- Blundell, S. J. and K. M. Blundell
2010. *Concepts in Thermal Physics*, volume 9780199562.
- Cahn, J. W., Y. Mishin, and A. Suzuki
2006. Coupling grain boundary motion to shear deformation. *Acta Materialia*, 54(19):4953–4975.
- Cantwell, P. R., M. Tang, S. J. Dillon, J. Luo, G. S. Rohrer, and M. P. Harmer
2014. Grain boundary complexions. *Acta Materialia*, 62(1):1–48.
- Chandra, N. and P. Dang
1999. Atomistic simulation of grain boundary sliding and migration. *Journal of Materials Science*, 34(4):655–666.
- Chen, K., J. Han, X. Pan, and D. J. Srolovitz

- 2020a. The grain boundary mobility tensor. *Proceedings of the National Academy of Sciences of the United States of America*, 117(9):4533–4538.
- Chen, K., J. Han, and D. J. Srolovitz
 2020b. On the Temperature Dependence of Grain Boundary Mobility. *Acta Materialia*, 194:412–421.
- Chen, K., J. Han, S. L. Thomas, and D. J. Srolovitz
 2019. Grain boundary shear coupling is not a grain boundary property. *Acta Materialia*, 167:241–247.
- Chen, K., D. J. Srolovitz, and J. Han
 2020c. Grain-Boundary Topological Phase Transitions. *arXiv*, 2011.01475v1.
- Chen, L.-Q. and G. Kalonji
 1992. Finite temperature structure and properties of $\Sigma = 5$ (310) tilt grain boundaries in nacl a molecular dynamics study. *Philosophical Magazine A*, 66(1):11–26.
- Combe, N., F. Mompiau, and M. Legros
 2016. Disconnections kinks and competing modes in shear-coupled grain boundary migration. *Physical Review B*, 93(2):024109.
- Dowling, N. E.
 1999. *Mechanical behavior of materials : engineering methods for deformation, fracture, and fatigue*. Pearson.
- Edington, J. W., K. N. Melton, and C. P. Cutler
 1976. Superplasticity. *Progress in Materials Science*, 21(1-2):61–170.
- Ercolessi, F. and J. B. Adams
 1994. Interatomic potentials from first-principles calculations: The force-matching method. *EPL*, 26(8):583–588.
- Foiles, S. M. and J. J. Hoyt
 2006. Computation of grain boundary stiffness and mobility from boundary fluctuations. *Acta Materialia*, 54(12):3351–3357.
- Frolov, T., D. L. Olmsted, M. Asta, and Y. Mishin
 2013. Structural phase transformations in metallic grain boundaries. *Nature Communications*, 4(1):1–7.
- Fukutomi, H., T. Iseki, T. Endo, and T. Kamijo
 1991. Sliding behavior of coincidence grain boundaries deviating from ideal symmetric tilt relationship. *Acta Metallurgica et Materialia*, 39(7):1445–1448.
- Furtkamp, M., G. Gottstein, D. A. Molodov, V. N. Semenov, and L. S. Shvindlerman
 1998. Grain boundary migration in Fe-3.5boundaries. *Acta Materialia*, 46(12):4103–4110.

- Gianola, D. S., S. Van Petegem, M. Legros, S. Brandstetter, H. Van Swygenhoven, and K. J. Hemker
2006. Stress-assisted discontinuous grain growth and its effect on the deformation behavior of nanocrystalline aluminum thin films. *Acta Materialia*, 54(8):2253–2263.
- Gorkaya, T., T. Burlet, D. A. Molodov, and G. Gottstein
2010. Experimental method for true in situ measurements of shear-coupled grain boundary migration. *Scripta Materialia*, 63(6):633–636.
- Gottstein, G. and L. S. Shvindlerman
2009. *Grain Boundary Migration in Metals*. Taylor Francis.
- Grünwald, W. and F. Haessner
1970. Thermisch aktivierte Korngrenzenwanderung in gewalzten Goldeinkristallen unter dem Einfluss gelöster Fremdatome. *Acta Metallurgica*, 18(2):217–224.
- Günster, C., D. A. Molodov, and G. Gottstein
2013. Migration of grain boundaries in Zn. *Acta Materialia*, 61(7):2363–2375.
- Hadian, R., B. Grabowski, M. W. Finnis, and J. Neugebauer
2018. Migration mechanisms of a faceted grain boundary. *Physical Review Materials*, 2(4):043601.
- Hamilton, J. C. and S. M. Foiles
2002. First-principles calculations of grain boundary theoretical shear strength using transition state finding to determine generalized gamma surface cross sections. *Physical Review B*, 65(6):064104.
- Han, J., S. L. Thomas, and D. J. Srolovitz
2018. Grain-boundary kinetics: A unified approach. *Progress in Materials Science*, 98:386–476.
- Han, J., V. Vitek, and D. J. Srolovitz
2017. The grain-boundary structural unit model redux. *Acta Materialia*, 133:186–199.
- Haslam, A. J., D. Moldovan, V. Yamakov, D. Wolf, S. R. Phillpot, and H. Gleiter
2003. Stress-enhanced grain growth in a nanocrystalline material by molecular-dynamics simulation. *Acta Materialia*, 51(7):2097–2112.
- Henkelman, G. and H. Jónsson
2000. Improved tangent estimate in the nudged elastic band method for finding minimum energy paths and saddle points. *The Journal of Chemical Physics*, 113(22):9978.
- Hirth, J. P. and R. W. Balluffi
1973. On grain boundary dislocations and ledges. *Acta Metallurgica*, 21(7):929–942.
- Hirth, J. P. and J. Lothe
1982. *Theory of dislocations*. Krieger Pub. Co.

- Hirth, J. P., R. C. Pond, and J. Lothe
2006. Disconnections in tilt walls. *Acta Materialia*, 54(16):4237–4245.
- Hirth, J. P., R. C. Pond, and J. Lothe
2007. Spacing defects and disconnections in grain boundaries. *Acta Materialia*, 55(16):5428–5437.
- Holm, E. A. and S. M. Foiles
2010. How Grain Growth Stops: A Mechanism for Grain-Growth Stagnation in Pure Materials. *Science*, 328:1138–1141.
- Holm, E. A., M. A. Miodownik, and A. D. Rollett
2003. On abnormal subgrain growth and the origin of recrystallization nuclei. *Acta Materialia*, 51(9):2701–2716.
- Holm, E. A., D. L. Olmsted, and S. M. Foiles
2010. Comparing grain boundary energies in face-centered cubic metals: Al, Au, Cu and Ni. *Scripta Materialia*, 63(9):905–908.
- Homer, E. R., S. M. Foiles, E. A. Holm, and D. L. Olmsted
2013. Phenomenology of shear-coupled grain boundary motion in symmetric tilt and general grain boundaries. *Acta Materialia*, 61(4):1048–1060.
- Homer, E. R., E. A. Holm, S. M. Foiles, and D. L. Olmsted
2014. Trends in grain boundary mobility: Survey of motion mechanisms. *JOM*, 66(1):114–120.
- Hu, H. and B. B. Rath
1972. Influence of Solute on the Mobility of Tilt Boundaries. In *The Nature and Behavior of Grain Boundaries*, H. Hu, ed., Pp. 405–435. New York, NY: Springer US.
- Irvine, W. T., A. D. Hollingsworth, D. G. Grier, and P. M. Chaikin
2013. Dislocation reactions, grain boundaries, and irreversibility in two-dimensional lattices using topological tweezers. *Proceedings of the National Academy of Sciences of the United States of America*, 110(39):15544–15548.
- Janssens, K. G. F., D. Olmsted, E. A. Holm, S. M. Foiles, S. J. Plimpton, and P. M. Derlet
2006. Computing the mobility of grain boundaries. *Nature Materials*, 5(2):124–127.
- Jonsson, H., G. Mills, and K. W. Jacobsen
1998. Nudged elastic band method for finding minimum energy paths of transitions. In *Classical and Quantum Dynamics in Condensed Phase Simulations*, B. J. Berne, G. Ciccotti, and D. F. Coker, eds., Pp. 385–404. World Scientific Pub Co Pte Lt.
- Karma, A., Z. T. Trautt, and Y. Mishin
2012. Relationship between Equilibrium Fluctuations and Shear-Coupled Motion of Grain Boundaries. *Physical Review Letters*, 109(9):095501.

- Kelchner, C. L., S. J. Plimpton, and J. C. Hamilton
1998. Dislocation nucleation and defect structure during surface indentation. *Physical Review B*, 58(17):11085–11088.
- Khantha, M., D. P. Pope, and V. Vitek
1994. Dislocation Screening and the Brittle-to-Ductile Transition: A Kosterlitz-Thouless Type Instability. *Physical Review Letters*.
- Khater, H. A., A. Serra, R. C. Pond, and J. P. Hirth
2012. The disconnection mechanism of coupled migration and shear at grain boundaries. *Acta Materialia*, 60(5):2007–2020.
- King, A. H. and D. A. Smith
1980. The effects on grain-boundary processes of the steps in the boundary plane associated with the cores of grain-boundary dislocations. *Acta Crystallographica Section A*, 36(3):335–343.
- Klain, D. A. and G.-C. Rota
1997. *Introduction to geometric probability*. Cambridge University Press.
- Kosterlitz, J. M. and D. J. Thouless
1973. Ordering, metastability and phase transitions in two-dimensional systems. *J. Phys. C : Solid State Phys*, 6.
- Legros, M., D. S. Gianola, and K. J. Hemker
2008. In situ TEM observations of fast grain-boundary motion in stressed nanocrystalline aluminum films. *Acta Materialia*, 56(14):3380–3393.
- Lejček, P., V. Paidar, J. Adámek, and S. Kadečková
1994. Grain boundary migration in $\Sigma=5$ bicrystals of an Fe-3alloy. *Interface Science*, 1(3):187–199.
- Li, C. H., E. H. Edwards, J. Washburn, and E. R. Parker
1953. Stress-induced movement of crystal boundaries. *Acta Metallurgica*, 1(2):223–229.
- Liao, M., X. Xiao, S. T. Chui, and Y. Han
2018. Grain-Boundary Roughening in Colloidal Crystals. *Physical Review X*, 8(2).
- MacPherson, R. D. and D. J. Srolovitz
2007. The von Neumann relation generalized to coarsening of three-dimensional microstructures. *Nature*, 446(7139):1053–1055.
- Meiners, T., T. Frolov, R. E. Rudd, G. Dehm, and C. H. Liebscher
2020. Observations of grain-boundary phase transformations in an elemental metal. *Nature*, 579(7799):375–378.
- Mishin, Y., D. Farkas, M. J. Mehl, and D. A. Papaconstantopoulos
1999. Interatomic potentials for monoatomic metals from experimental data and ab initio

- calculations. *Physical Review B - Condensed Matter and Materials Physics*, 59(5):3393–3407.
- Mishin, Y., M. J. Mehl, D. A. Papaconstantopoulos, A. F. Voter, and J. D. Kress
2001. Structural stability and lattice defects in copper: Ab initio, tight-binding, and embedded-atom calculations. *Physical Review B*, 63(22):224106.
- Molodov, D. A., U. Czubayko, G. Gottstein, and L. S. Shvindlerman
1995. Mobility of 111 tilt grain boundaries in the vicinity of the special misorientation $\Sigma=7$ in bicrystals of pure aluminium. *Scripta Metallurgica et Materialia*, 32(4):529–534.
- Molodov, D. A., G. Gottstein, F. Heringhaus, and L. S. Shvindlerman
1998. True absolute grain boundary mobility: Motion of specific planar boundaries in Bi-bicrystals under magnetic driving forces. *Acta Materialia*, 46(16):5627–5632.
- Molteni, C., G. P. Francis, M. C. Payne, and V. Heine
1996. First Principles Simulation of Grain Boundary Sliding. *Physical Review Letters*, 76(8):1284–1287.
- Molteni, C., N. Marzari, M. C. Payne, and V. Heine
1997. Sliding Mechanisms in Aluminum Grain Boundaries. *Physical Review Letters*, 79(5):869–872.
- Mompiou, F., D. Caillard, and M. Legros
2009. Grain boundary shear-migration coupling-I. In situ TEM straining experiments in Al polycrystals. *Acta Materialia*, 57(7):2198–2209.
- Mullins, W. W.
1956. Two-dimensional motion of idealized grain boundaries. *Journal of Applied Physics*, 27(8):900–904.
- Olmsted, D. L., S. M. Foiles, and E. A. Holm
2007. Grain boundary interface roughening transition and its effect on grain boundary mobility for non-faceting boundaries. *Scripta Materialia*, 57(12):1161–1164.
- Olmsted, D. L., E. A. Holm, and S. M. Foiles
2009. Survey of computed grain boundary properties in face-centered cubic metals—II: Grain boundary mobility. *Acta Materialia*, 57(13):3704–3713.
- Onsager, L.
1931. Reciprocal relations in irreversible processes. I. *Physical Review*, 37(4):405–426.
- Plimpton, S. J.
1995. Fast Parallel Algorithms for Short-Range Molecular Dynamics. *Journal of Computational Physics*, 117(1):1–19.
- Pond, R. C. and W. Bollmann
1979. The Symmetry and Interfacial Structure of Bicrystals. *Philosophical Transactions*

- of the Royal Society A: Mathematical, Physical and Engineering Sciences*, 292(1395):449–472.
- Powers, J. D. and A. M. Glaeser
1998. Grain boundary migration in ceramics. *Interface Science*, 6(1-2):23–39.
- Priedeman, J. L., D. L. Olmsted, and E. R. Homer
2017. The role of crystallography and the mechanisms associated with migration of incoherent twin grain boundaries. *Acta Materialia*, 131:553–563.
- Rahman, M., H. Zurob, and J. Hoyt
2014. A comprehensive molecular dynamics study of low-angle grain boundary mobility in a pure aluminum system. *Acta Materialia*, 74:39–48.
- Rajabzadeh, A., M. Legros, N. Combe, F. Momprou, and D. A. Molodov
2013a. Evidence of grain boundary dislocation step motion associated to shear-coupled grain boundary migration. *Philosophical Magazine*, 93(10-12):1299–1316.
- Rajabzadeh, A., F. Momprou, M. Legros, and N. Combe
2013b. Elementary mechanisms of shear-coupled grain boundary migration. *Physical Review Letters*, 110(26):265507.
- Rheinheimer, W. and M. J. Hoffmann
2015. Non-Arrhenius behavior of grain growth in strontium titanate: New evidence for a structural transition of grain boundaries. *Scripta Materialia*, 101:68–71.
- Rottman, C.
1986. Roughening of low-angle grain boundaries. *Physical Review Letters*, 57(6):735–738.
- Rupert, T. J., D. S. Gianola, Y. Gan, and K. J. Hemker
2009. Experimental observations of stress-driven grain boundary migration. *Science (New York, N.Y.)*, 326(5960):1686–90.
- Rutter, J. and K. Aust
1965. Migration of 100 tilt grain boundaries in high purity lead. *Acta Metallurgica*, 13(3):181–186.
- Sansoz, F. and J. F. Molinari
2005. Mechanical behavior of Σ tilt grain boundaries in nanoscale Cu and Al: A quasi-continuum study. *Acta Materialia*, 53(7):1931–1944.
- Schönfelder, B., G. Gottstein, and L. S. Shvindlerman
2005. Comparative study of grain-boundary migration and grain-boundary self-diffusion of [0 0 1] twist-grain boundaries in copper by atomistic simulations. *Acta Materialia*, 53(6):1597–1609.
- Sheikh-Ali, A. D., J. A. Szpunar, and H. Garmestani

2003. Stimulation and Suppression of Grain Boundary Sliding by Intragranular Slip in Zinc Bicrystals. *Interface Science*, 11(4):439–450.
- Shiga, M. and W. Shinoda
2004. Stress-assisted grain boundary sliding and migration at finite temperature: A molecular dynamics study. *Physical Review B*, 70(5):054102.
- Song, H. and J. Hoyt
2012. A molecular dynamics simulation study of the velocities, mobility and activation energy of an austenite–ferrite interface in pure Fe. *Acta Materialia*, 60(10):4328–4335.
- Stukowski, A.
2010. Visualization and analysis of atomistic simulation data with OVITO—the Open Visualization Tool. *Modelling and Simulation in Materials Science and Engineering*, 18(1):015012.
- Sutton, A. P. and R. W. Balluffi
1995. *Interfaces in Crystalline Materials*.
- Swendsen, R. H.
1977. Roughening transition in the solid-on-solid model. *Physical Review B*, 15(2):689–692.
- Thomas, S. L., K. Chen, J. Han, P. K. Purohit, and D. J. Srolovitz
2017. Reconciling grain growth and shear-coupled grain boundary migration. *Nature Communications*, 8(1):1–12.
- Trautt, Z. T., M. Upmanyu, and A. Karma
2006. Interface mobility from interface random walk. *Science*, 314(5799):632–635.
- Turnbull, D.
1951. Theory of Grain Boundary Migration Rates. *JOM*, 3(8):661–665.
- Upmanyu, M., D. Srolovitz, L. Shvindlerman, and G. Gottstein
1999. Misorientation dependence of intrinsic grain boundary mobility: simulation and experiment. *Acta Materialia*, 47(14):3901–3914.
- Viswanathan, R. and C. L. Bauer
1973. Kinetics of grain boundary migration in copper bicrystals with [001] rotation axes. *Acta Metallurgica*, 21(8):1099–1109.
- Von Neumann, J.
1952. Discussion: shape of metal grains. In *Metal Interfaces*, C. Herring, ed., Pp. 108–110.
- Washburn, J. and E. R. Parker
1952. Kinking in Zinc Single-Crystal Tension Specimens. *JOM*, 4(10):1076–1078.

- Winning, M., G. Gottstein, and L. Shvindlerman
2001. Stress induced grain boundary motion. *Acta Materialia*, 49(2):211–219.
- Winning, M., G. Gottstein, and L. Shvindlerman
2002. On the mechanisms of grain boundary migration. *Acta Materialia*, 50(2):353–363.
- Winning, M. and A. D. Rollett
2005. Transition between low and high angle grain boundaries. *Acta Materialia*, 53(10):2901–2907.
- Yoshida, H., K. Yokoyama, N. Shibata, Y. Ikuhara, and T. Sakuma
2004. High-temperature grain boundary sliding behavior and grain boundary energy in cubic zirconia bicrystals. *Acta Materialia*, 52(8):2349–2357.
- Zhang, H., M. Mendelev, and D. Srolovitz
2004. Computer simulation of the elastically driven migration of a flat grain boundary. *Acta Materialia*, 52(9):2569–2576.
- Zhang, H., M. I. Mendelev, and D. J. Srolovitz
2005. Mobility of 5 tilt grain boundaries: Inclination dependence. *Scripta Materialia*, 52(12):1193–1198.
- Zhang, H., D. J. Srolovitz, J. F. Douglas, and J. A. Warren
2009. Grain boundaries exhibit the dynamics of glass-forming liquids. *Proceedings of the National Academy of Sciences of the United States of America*, 106(19):7735–7740.
- Zhou, J. and V. Mohles
2011. Towards realistic molecular dynamics simulations of grain boundary mobility. *Acta Materialia*, 59(15):5997–6006.